Politecnico di Milano
Dipartimento di Chimica, Materiali e Ingegneria Chimica "G. Natta"
Doctoral Programme In Industrial Chemistry and Chemical Engineering

---

Implementation of detailed chemistry in large-scale combustion computations

Doctoral Dissertation of:

Alessandro STAGNI 802364

Supervisor:

Prof. Tiziano FARAVELLI

Tutor:

Prof. Giuseppe RESNATI

The Chair of the Doctoral Program:

Prof. Alessio FRASSOLDATI

XXVIII Cycle – 2013/2015

To my family

"Considerate la vostra semenza:
fatti non foste a viver come bruti,
ma per seguir virtute e canoscenza."

Dante Alighieri (1265-1321)
La Divina Commedia, Inferno XXVI, 118-120

Acknowledgements

At the end of this Ph.D. experience, recognizing the roles of all those who have someway contributed to this final accomplishment is more than appropriate. First of all, I would like to thank Professor Tiziano Faravelli for the continuous support and the helpful discussions throughout these years. I am also grateful to Professors Eliseo Ranzi, Alessio Frassoldati and Alberto Cuoci for their key role in my educational growth, and for introducing me to combustion science in its countless facets. I appreciated the availability of Professors Pascale Desgroux and Tamás Turányi, too, for being the external examiners of my defense committee.

I would like to thank Professor Matthias Ihme for allowing me to carry out 10 months of my Ph.D. at Stanford University, where I had the privilege to complete my educational path, and to make a significant step forward in my personal growth. The active cooperation with his group is fully recognized, with a particular mention to Lucas Esclapez, Hao Wu, Jeff O'Brien and Pavan Govindaraju.

The whole CRECK modeling group at Politecnico di Milano deserves a specific acknowledgement. Thanks to Giancarlo Gentile and Matteo Pelucchi for sharing memorable moments, inside and outside the university walls; to Chiara Saggese and Mattia Bissoli, with whom I have shared almost 10 years of Chemical Engineering studies; to Tiziano Maffei, for his guiding role as "experienced" Ph.D. in our group; and to Isabella Branca, for her unconditioned help in solving our everyday problems. Thanks also to Steffen Salenbauch and Michael Evans, whose friendship extended well beyond their visiting period at Politecnico.

Gratefulness to my Ph.D. colleagues, whom I had the pleasure to meet in these years within Politecnico. This common path has been full of exciting experiences, which have made the everyday life at Politecnico pretty enjoyable. A special mention also goes to my longtime friends: Carlo Maria Campelli, Matteo D'Isanto, Stefano Langè, Giorgio Belfiore, who have kept playing a major role in my life in spite of the geographical distance.

Finally, thanks to my family for the unconditioned support during these years, without whom this experience could have never started four years ago, continued in the United States and ended up today.

Milan, July 12$^{\text{th}}$, 2016

Publications

Cuoci, A., Frassoldati, A., **Stagni, A.**, Faravelli, T., Ranzi, E., & Buzzi-Ferraris, G. (2013). Numerical modeling of NO_x formation in turbulent flames using a kinetic post-processing technique. Energy & Fuels, 27(2), 1104-1122.

Stagni, A., Cuoci, A., Frassoldati, A., Faravelli, T., & Ranzi, E. (2014). A fully coupled, parallel approach for the post-processing of CFD data through reactor network analysis. Computers & Chemical Engineering, 60, 197-212.

Stagni, A., Cuoci, A., Frassoldati, A., Faravelli, T., & Ranzi, E. (2014). Lumping and reduction of detailed kinetic schemes: an effective coupling. Industrial & Engineering Chemistry Research, 53(22), 9004-9016.

Ranzi, E., Frassoldati, A., **Stagni, A.**, Pelucchi, M., Cuoci, A., & Faravelli, T. (2014). Reduced Kinetic Schemes of Complex Reaction Systems: Fossil and Biomass-Derived Transportation Fuels. International Journal of Chemical Kinetics, 46(9), 512-542.

Pelucchi, M., Bissoli, M., Cavallotti, C., Cuoci, A., Faravelli, T., Frassoldati, A., Ranzi, E. & **Stagni, A.** (2014). Improved Kinetic Model of the Low-Temperature Oxidation of n-Heptane. Energy & Fuels, 28(11), 7178-7193.

Frassoldati, A., D'Errico, G., Lucchini, T., **Stagni**, A., Cuoci, A., Faravelli, T., Onorati, A. & Ranzi, E. (2015). Reduced kinetic mechanisms of diesel fuel surro-

gate for engine CFD simulations. Combustion and Flame, 162(10), 3991–4007.

Stagni, A., Frassoldati, A., Cuoci, A., Faravelli, T., & Ranzi, E. (2016). Skeletal mechanism reduction through species-targeted sensitivity analysis. Combustion and Flame, 163, 382-393.

Bernardi, M.S., Pelucchi, M., **Stagni, A.**, Sangalli, L.M., Cuoci, A., Frassoldati, A., Secchi, P., & Faravelli, T. (2016). Curve Matching, a generalized framework for models/experiments comparison: an application to n-heptane combustion kinetic mechanisms. Combustion and Flame, 168, 186-203.

Evans, M.J., Medwell, P.R., Tian, Z., Frassoldati, A., Cuoci, A., & **Stagni, A.** (2016). Ignition Characteristics in Spatially Zero-, One- and Two- Dimensional Laminar Ethylene Flames. AIAA Journal, *in press.*

Frassoldati, A., Cuoci, A., **Stagni, A.**, Faravelli, T., & Ranzi, E. (2016). Skeletal kinetic mechanism for Diesel combustion. Combustion Theory and Modeling, *under review.*

Stagni, A., Esclapez, L., Govindaraju, P., Cuoci, A., Faravelli, T., & Ihme, M. (2016). The role of preferential evaporation on the ignition of multicomponent fuels in a homogeneous spray/air mixture. Proceedings of the Combustion Institute 36, *in press.*

Evans, M.J., Medwell, P.R., Wu, H., **Stagni, A.**, & Ihme, M. (2016). Classification and Lift-Off height prediction of non-premixed MILD and autoignitive flames. Proceedings of the Combustion Institute 36, *in press.*

Franzelli, B., Cuoci, A., **Stagni, A.**, Ihme, M., Faravelli, T., & Candel, S. (2016). Numerical investigation of soot-flame-vortex interactions. Proceedings of the Combustion Institute 36, *accepted for oral presentation.*

Maringer, G., Frassoldati, A., Gehmlich, R., **Stagni, A.**, Ranzi, E., Seshadri, K. (2016). Autoignition of Condensed Hydrocarbon Fuels in Nonpremixed Flows at Elevated Pressures. Combustion Theory and Modeling, *under review.*

Conferences

Stagni, A., Cuoci, A., Frassoldati, A., Faravelli, T., & Ranzi, E. A Fully Coupled Approach for Predicting Pollutants Formation Through Reactor Network Analysis, 14th International Conference on Numerical Combustion, April 8-10, 2013, San Antonio (TX), United States.

D'Errico, G., Lucchini, T., **Stagni, A.**, Frassoldati, A., Faravelli, T., & Ranzi, E.. Reduced kinetic mechanisms for diesel spray combustion simulations. 11th International Conference on Engines & Vehicles, September 15-19, 2013, Capri (NA), Italy.

Stagni, A., Saggese, C., Bissoli, M., Cuoci, A., Frassoldati, A., Faravelli, T., & Ranzi, E. Reduced Kinetic Model of Biodiesel Fuel Combustion, International Conference on BioMass, May 4-7, 2014, Florence, Italy.

Franzelli, B., Cuoci, A., **Stagni, A.**, Saggese, C., Frassoldati, A., Faravelli, T. & Ihme, M., Accounting for strain-rate effect in soot modeling of turbulent flames, 15th International Conference on Numerical Combustion, April 19-22, 2015, Avignon, France.

Frassoldati, A., Cuoci, A., **Stagni, A.**, Faravelli, T., Ranzi, E., Skeletal kinetic mechanism for Diesel combustion, 9th Mediterranean Combustion Symposium, June 7-11, 2015, Rhodes, Greece.

Evans, M. J., Medwell, P. R., Tian, Z. F., Frassoldati, A., Cuoci, A., & **Stagni, A.** Ignition Characteristics in Spatially Zero-, One- and Two- Dimensional Laminar Ethylene Flames. 22nd AIAA Computational Fluid Dynamics Conference, June 22-26, 2015, Dallas (TX), United States.

Pelucchi, M., **Stagni, A.,** Bissoli, M., Cuoci, A., Frassoldati, A., Ranzi, E., Faravelli, T., Detailed kinetic mechanisms for practical applications: new reaction classes and model reduction. CleanAir 2015, July 5-9, 2015, Lisbon, Portugal.

Govindaraju, P., **Stagni, A.**, & Ihme, M., Evaporation and combustion characteristics of multicomponent fuels. 68th Annual Meeting of the APS Division of Fluid Dynamics, November 22-24, 2015, Boston (MA), United States.

Evans, M. J., Medwell, P. R., Wu, H., **Stagni, A.**, Ihme, M., Classification of non-premixed MILD and autoignitive flames, Australian Combustion Symposium, December 7-9, 2015, Melbourne, Australia.

Stagni, A., Frassoldati, A., Cuoci, A., Faravelli, T., & Ranzi, E. Kinetic modeling of soot formation from n-heptane combustion, Kaust Future Fuels Workshop, March 7-9, 2016, Thuwal, Saudi Arabia.

Stagni, A., Bernardi, M.S., Pelucchi, M., Sangalli, L.M., Cuoci, A., Frassoldati, A., Secchi, P., Faravelli, T., Curve Matching: a generalized framework for model comparison with large sets of experiments, Workshop of the WG4 SMART-CATs COST Action, April 5-6, 2016, Naples, Italy.

Contents

Abstract

The use of combustion for the production of energy must comply with increasingly stringent regulations, pushing towards higher efficiencies and lower emissions of pollutant compounds. In this scenario, the research towards newer fuels and burning technologies assumes a key importance. In the latest years significant progresses have already been attained, and the margins for further improvement are still wide. To this end, the role of numerical simulations in support of experimental research has recently become more and more central. Specifically, the higher available computing power has allowed to use detailed kinetic models for the simplest fuels (methane, hydrogen, etc.), which are required to give a predictive value to numerical simulations. Yet, for real fuels like those used for transportation purposes, a direct utilization of detailed chemistry is not currently possible, because of their excessive size.

The purpose of this Thesis is originated from this limitation affecting detailed mechanisms. Although the field of kinetic mechanism reduction has been very active for at least three decades, at present a generalized procedure to obtain a systematic reduction with the desired degree of accuracy on defined targets is not available yet. The existing, state-of-the-art methods, based on the coupling between flux analysis and sensitivity analysis, are often insufficient to obtain a satisfactory size, such that the obtained schemes can be used in combustion simulations. Moreover, they are targeted at preserving accuracy on fuel reactivity, in terms of ignition delay time, thus excluding phenomena not directly related to it, like pollutants formation. For this reason, a multi-step approach was developed, where multiple reduction techniques were combined. It is shown that a substantial degree of reduction could be ensured by an upstream chemical lumping, i.e. by

grouping the isomers of the intermediate species and radicals, without affecting model accuracy. Its combination with the established flux and sensitivity analysis techniques provides a significant advantage in the size of the reduced mechanisms, which becomes even wider with the increasing fuel complexity. Sensitivity analysis is also extended to include different targets throughout the reduction procedure. In order to quantify the capability of a kinetic mechanism in reproducing the dynamics of species formation, a multi-faceted methodology for curve comparison was developed. Initially conceived for comparing kinetic models and experiments, it was implemented in the reduction framework to rank skeletal models according to a defined target property, and a Species-Targeted Sensitivity Analysis was successfully included in the reduction framework. The overall approach was implemented into a freely-available numerical tool through a parallel programming protocol, thus allowing to carry out mechanism reduction within hours.

The availability of this reduction framework allows to carry out fundamental studies of combustion dynamics with a significant decrease of the required times. Also, a greater level of detail can be placed on the aspects not directly related to chemical kinetics. Two case studies better illustrate this concept. The two-phase ignition of multicomponent droplets in a homogeneous environment was investigated, and the role of preferential evaporation in gas-turbine relevant conditions was quantified. The implementation of a multicomponent diffusion model, as well as a cubic equation of state to account for equilibrium, allowed to find operating conditions, in terms of starting diameter and equivalence ratio, where preferential evaporation is strongly affecting the two-phase ignition. Moreover, the influence of low-temperature chemistry in such conditions is highlighted, and its crucial role in the region governed by preferential evaporation is demonstrated.

The species-targeted reduction methodology was then applied to the case of soot formation from real fuels. Starting from a discrete sectional model to couple gas and solid phase, the reduction framework required proper adaptation of the target properties, due to the continuous distribution of particle size and composition characterizing soot. By setting mass fraction and particle size distribution as reduction targets, a skeletal mechanism was obtained, and its benchmark against original mechanism and experimental data provided a positive outcome. The obtained mechanism was used to investigate the evolution of soot in isolated droplets in microgravity conditions. This allowed to observe the formation of an inner soot layer, surrounded by the flame front, both progressively moving away from the droplet surface (coherently with experimental observations). Specifically, (i) the thermophoretic effect was found to be the critical factor causing maximum volume

fractions orders of magnitude higher than what observed in gas-phase diffusion flames, and (ii) radiation was found to have a strong impact on the extinction of sooting droplets, for which a simple gray-gas model, currently used in most Computational Fluid Dynamic (CFD) simulations, is not accurate enough to predict flame radiance.

Sommario

La produzione di energia tramite processi di combustione è al giorno d'oggi sottoposta a limiti di legge sempre più restrittivi, che spingono verso maggiori efficienze e minori emissioni di sostanze inquinanti. In questo scenario, la ricerca verso nuovi combustibili e nuove tecnologie di combustione assume un ruolo di primo piano. Negli ultimi anni progressi significativi sono stati già ottenuti, ma i margini per un ulteriore miglioramento sono ancora ampi. A tal fine, il ruolo delle simulazioni numeriche a supporto della ricerca sperimentale è recentemente diventato sempre più centrale. In particolare, la maggiore potenza computazionale a disposizione di università e industrie ha permesso di utilizzare, per i combustibili più semplici (metano, idrogeno, ecc.) modelli cinetici dettagliati, che sono essenziali per dare un valore predittivo alle simulazioni numeriche. Tuttavia, per combustibili più complessi come quelli utilizzati per il trasporto pubblico e privato, l'utilizzo diretto di cinetiche dettagliate non è attualmente possibile a causa delle dimensioni eccessive.

Lo scopo di questa Tesi nasce da questa limitazione che caratterizza la maggior parte degli schemi cinetici dettagliati. Sebbene la riduzione di meccanismi cinetici è un campo di ricerca molto attivo da almeno tre decenni, attualmente una procedura generalizzata per ottenere una riduzione sistematica con il grado di accuratezza richiesto su determinate proprietà non è stato ancora sviluppato. Infatti, le più recenti metodologie di riduzione, basate sull'accoppiamento tra analisi dei flussi e analisi di sensitività, sono spesso insufficienti per ottenere delle dimensioni accettabili per un successivo utilizzo in simulazioni di combustione. Inoltre, finora queste tecniche sono sempre state mirate a mantenere una corretta reattività del combustibile, in termini di tempi di autoignizione. In questo modo,

l'accuratezza su proprietà non direttamente legate a questo, come la formazione di composti inquinanti, non può essere garantita. Per questo motivo, in questa Tesi un processo composto di più stadi è stato sviluppato, in cui più tecniche di riduzione sono state combinate in serie. Infatti, viene mostrato come una riduzione significativa può essere ottenuta mediate un "lumping chimico" delle specie in gioco, ovvero raggruppando gli isomeri di specie e radicali intermedie in pseudo-specie, senza ripercussioni significative sull'accuratezza del modello cinetico. La combinazione di questo approccio con le tecniche consolidate di analisi dei flussi e analisi di sensitività fornisce un vantaggio significativo nella dimensione dei meccanismi ridotti, che diventa tanto piu evidente all'aumentare della complessità del combustibile considerato. Inoltre, l'analisi di sensitività è estesa per includere differenti proprietà come obiettivo di riduzione. Al fine di quantificare la capacità di un meccanismo cinetico nel riprodurre la dinamica di formazione delle specie obiettivo, una metodologia per il confronto tra curve è stata sviluppata. In un primo momento, questa è stata ideata per confrontare modelli cinetici ed esperimenti; in seguito, questa è stata implementata nella metodologia di riduzione per classificare meccanismi scheletali in funzione di una determinata proprietà obiettivo, ed una *Species-Targeted Sensitivity Analysis* è stata inclusa con successo nell'approccio generale. Questo è stato implementato in un codice numerico, liberamente accessibile alla comunità scientifica, tramite un protocollo di programmazione parallela, permettendo quindi di eseguire una riduzione dei meccanismi cinetici in tempi dell'ordine delle ore.

La disponibilità di questo approccio generale alla riduzione ha permesso di eseguire studi fondamentali delle dinamiche di combustione con una diminuzione significativa dei tempi richiesti. Inoltre, in questo modo un maggiore livello di dettaglio può essere garantito su aspetti non direttamente legati alla cinetica chimica. Due esempi illustrano meglio questo concetto. L'ignizione di gocce multicomponente in un ambiente gassoso omogeneo è stata analizzata, ed è stato possibile quantificare il ruolo dell'evaporazione preferenziale nelle condizioni caratteristiche delle turbine a gas. L'implementazione di un modello di diffusione multicomponente e l'utilizzo di una equazione di stato cubica per tenere in conto l'equilibrio liquido-vapore, ha permesso di individuare condizioni operative, in termini di diametro e rapporto di equivalenza globale, in cui l'evaporazione preferenziale influenza notevolmente l'ignizione bifase. Inoltre, nelle condizioni considerate è stata individuata una notevole influenza delle cinetiche di bassa temperatura, il cui ruolo cruciale nella regione governata dall'evaporazione preferenziale è stato dimostrato.

La metodologia di riduzione è stata quindi applicata al caso della formazione di soot da combustibili liquidi. Partendo da un modello a sezioni discrete per accoppiare fase liquida e fase gassosa, l'approccio sviluppato ha richiesto una modifica opportuna per tenere in conto le proprietà caratteristiche del soot, ovvero una distribuzione continua delle dimensioni delle particelle e delle relative composizioni. Impostando frazione massiva e distribuzione delle dimensioni delle particelle come proprietà obiettivo è stato possibile ottenere un meccanismo scheletale, validato positivamente in casi mono- e bidimensionali, tramite confronto con dati sperimentali e meccanismo originale. Lo schema ottenuto è stato utilizzato per analizzarre l'evoluzione del soot in gocce isolate in condizioni di microgravità. Ciò ha permesso di osservare la formazione di un guscio interno di soot, circondato da un fronte di fiamma. Coerentemente con le osservazioni sperimentali, è stato possibile verificare che entrambi si allontatano progressivamente dalla superficie della goccia. Inoltre, è stato possibile verificare che (i) l'effetto termoforetico è il fattore critico che causa frazioni volumetriche di soot ordini di grandezza più elevati di quanto osservato in fiamme diffusive in fase gas, e che (ii) la radiazione della fiamma ha un impatto decisivo sull'estinzione delle gocce stesse, per le quali un classico modello di "gas grigio", attualmente usato nella maggior parte delle applicazioni di Fluidodinamica Computazionale (CFD), non è abbastanza accurato per predire le emissioni radiative.

List of Figures

List of Tables

Nomenclature

Roman Symbols

C	Heat capacity
k	Thermal conductivity
v	Velocity
P	Pressure
T	Temperature
x	Mole Fraction
Y	Mass Fraction

Acronyms

CFD	Computational Fluid Dynamic
CSP	Computational Singular Perturbation
CSP	Computational Singular Perturbation
DAE	Differential-Algebraic Equations
DIC	Direct Interaction Coefficient
DNS	Direct Numerical Simulation
DRG	Directed Relation Graph
DRGEP	DRG with Error Propagation

FDA	Functional Data Analysis
FSR	Flame Standoff Ratio
ICE	Internal Combustion Engine
IDT	Ignition Delay Time
JSR	Jet Stirred Reactor
LLNL	Lawrence Livermore National Laboratory
LTC	Low Temperature Chemistry
MEEM	Model-Experiment Error Matrix
MEV	Model Error Vector
MW	Molecular Weight
NO_x	Nitrogen Oxides
NTC	Negative Temperature Coefficient
ODE	Ordinary Differential Equation
OIC	Overall Interaction Coefficient
PAH	Polycyclic Aromatic Hydrocarbons
PCA	Principal Component Analysis
PFA	Path Flux Analysis
PFR	Plug Flow Reactor
PRF	Primary Reference Fuel
PSDF	Particle Size Distribution Function
QSSA	Quasi Steady-State Approximation
RFA	Reacting Flux Analysis
SSR	Soot Standoff Ratio
STSA	Species Targeted Sensitivity Analysis
TRF	Toluene Reference Fuel

Greek Symbols

α	Accomodation factor
μ	Dynamic viscosity
ν	Stoichiometric coefficient
Φ	Equivalence Ratio
ρ	Density
τ	Residence time

Subscripts

i	Species subscript
j	Reaction subscript
k	Reactor subscript

Mathematical Symbols

$\dot{\omega}$	Net reaction rate
$Đ_{ij}$	Stefan-Maxwell binary diffusion coefficient
$Đ^0_{ij}$	Infinite dilution diffusion coefficient of the i-th species into j
D_{ij}	Fick's binary diffusion coefficient

CHAPTER 1

Introduction

TODAY it is widely acknowledged [1] that, in spite of the continuous efforts towards renewable sources of energy, the dominant role of combustion in the world scenario will last for most of the 21st century: in a world where the energy demand grows in parallel with the gross domestic product, the larger exploitation of renewable sources is not able to balance the increase in energy production [2] (Figure 1.1). While the demand from western countries is expected to remain

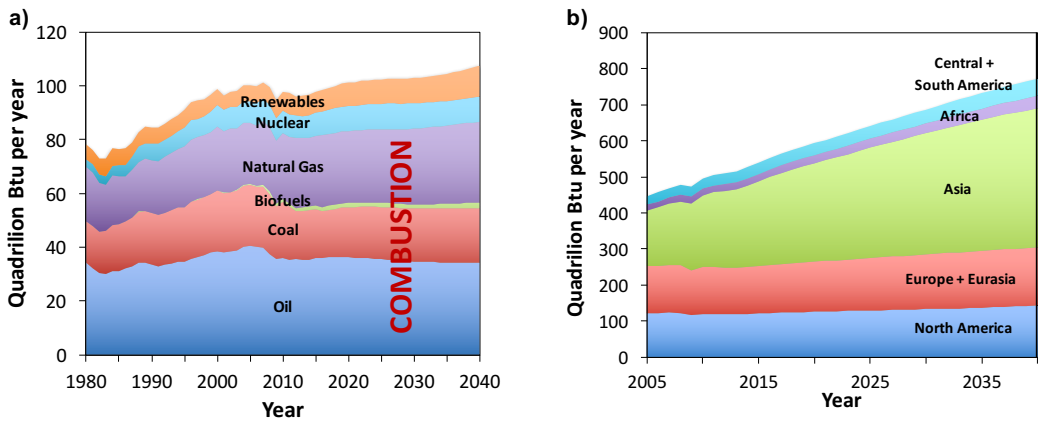

Figure 1.1: a) US annual energy production (by source): history and predictions. b) World annual energy production (by region): history and predictions. From [2].

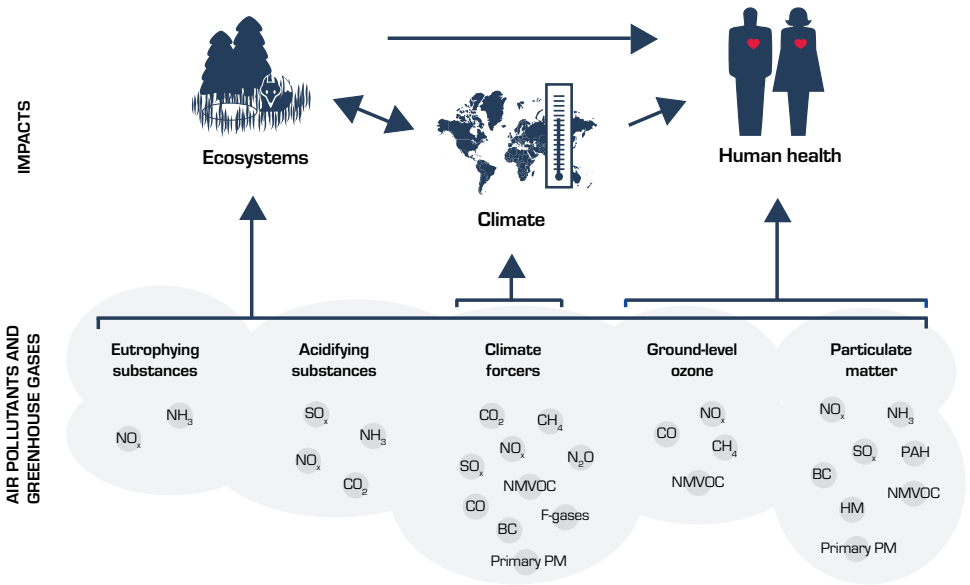

Figure 1.2: Potential impacts of air pollutants and greenhouse gases. From [4].

approximately constant, the demographic and economic growth of Asian emerging powers are currently boosting the global energy trends.

Although fossil fuel reserves do not currently appear to be a limitation for the forthcoming decades [3], the sustainability of a never-ending growth is a major political and scientific issue. As a matter of fact, combustion processes are among the main producers of greenhouse gases and air pollutants [4], whose major impacts on ecosystem, climate change and human health are summarized in Figure 1.2. Moreover, the massive use of crude oil and natural gas for energy production is unavoidable to maintain the current status of modern societies, and the development of a new infrastructure based on their total replacement with new sources of power is a process requiring decades. Today the major advantages deriving from the use of fossil fuels are their cheap availability and established production and distribution network, which puts them in a privileged position, if compared to renewable sources.

Therefore, the slow transition to new energy sources is accompanied by a continued effort in combustion research; this revolves around the sustainability concept, in order to minimize the negative effects of fossil (and non-fossil) fuels exploitation. Two parallel targets are then pursued:

- Combustion efficiency: considering the huge amounts of energy at stake, even the smallest improvements in fuel consumption would result in huge savings of fuel itself, and parallel reductions in CO_2 emissions (whose formation is,

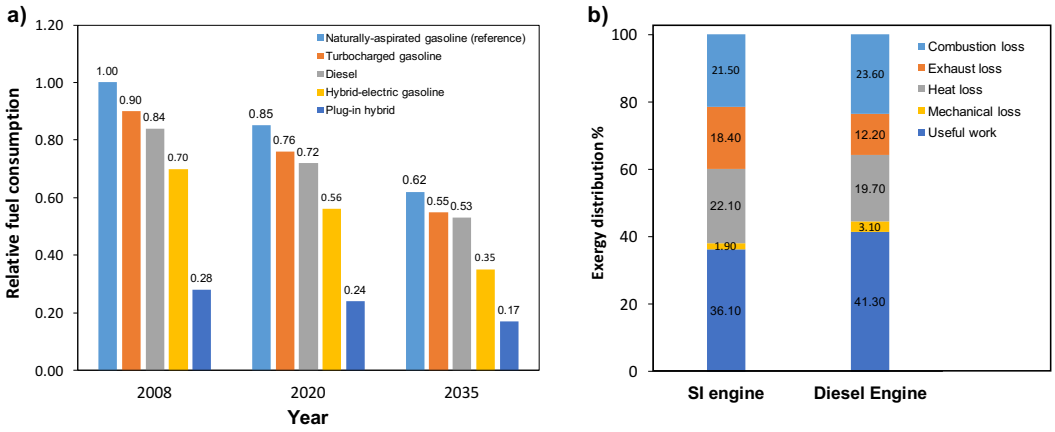

Figure 1.3: a) Expected relative fuel consumption of passenger cars [6] b) Energy losses in ICEs [7].

anyway, unavoidable as a direct product of combustion).

- Reduction of pollutants, whose formation is an indirect result of the overall combustion process, and can in principle be avoided or at least minimized.

In both cases, more and more stringent regulations [5] are being set into place by governments and agencies. Yet, the potential improvements attainable in this field are still significant: as an illustrative example, Figure 1.3b shows that, at present, the net efficiency of Internal Combustion Engines (ICE) is around 40%. About one third of the overall losses is related to combustion itself. They are due, for example, to the imperfect mixing between reactants, resulting then in incomplete combustion and in the formation of byproducts, like carbon monoxide and unburned hydrocarbons, with an unexploited residual calorific power. The expectations for the reductions in fuel utilization in the first two decades are quite optimistic: Figure 1.3a shows that a 38% efficiency improvement in the 140-years-old spark-ignited engine is expected by 20 years, and that the combination of multiple technologies, like plug-in hybrid engines, could drastically drop fuel consumption up to almost one order of magnitude.

As one can imagine, obtaining such improvements is subject to a comprehensive, first-principles knowledge of the (i) fluid dynamic and (ii) kinetic fundamentals behind the combustion process. For this reason, in the latest decades the use of empiricism has been slowly replaced by a more structured approach to the matter. The synergistic coupling between fundamental experiments and numerical modeling has characterized the latest decades of research in combustion. The exploit in computational capability has paved the way to more and more sophisticated models, whose prediction power has then increased, such that today they

are of common use in combustion engineering.

Indeed, the introduction of numerical simulations is able to provide what experiments alone are not always able to guarantee: flexibility. The more and more complete understanding of combustion chemistry offers new perspectives in terms of efficient and low-emission burning regimes. A significant example in this direction is represented by the Homogeneous Charge Compression Ignition (HCCI) engine: it combines the features of gasoline and diesel engines, and is able to reach higher efficiencies than traditional ICEs; moreover, its low-temperature operating conditions and lean inlet composition can guarantee ultra-low emissions of Nitrogen Oxides (NO_x) as well as soot and particulate matter. On the other hand, the key role of the low- and intermediate-temperature chemistry and the consequent double-stage ignition, as well as of heat release, make such technology very difficult to setup and control. Considering the wide range of operating conditions in which ICEs are required to work, and the different nature of fuel blends potentially feeding them, it is easy to imagine that a purely experimental approach to its development would be very time consuming, as well as overmuch expensive.

1.1 Detailed chemistry in combustion simulations

Since the 1970s, increasingly accessible computing power and memory has boosted the development of detailed mechanisms for combustion chemistry. Compatibly with resources available at that time, hydrogen and methane mechanisms were the first fuels investigated. As remarked by Westbrook et al. in their review [8], the importance of having a detailed mechanism for methane has allowed to gain insight in the elementary steps behind its combustion, like the role of the methyl radical recombination (giving ethane) in the overall reaction pathways. Also, it has made possible to rationalize the dramatically different autoignition tendency of pure methane, which is the most stable hydrocarbon, and methane doped with small amounts of higher hydrocarbons. From mid-90s, the computational resources, and the kinetic know-how, were mature enough for a detailed modeling of heavier fuels. The use of the hierarchicality concept [9] has greatly simplified this job: the extension of a kinetic mechanism to a more complex fuel has only required to add the subset of elementary reactions bringing from the new fuels to the smaller molecules, whose behavior has already been modeled. In this way, the development of gas-phase mechanisms for heavier fuels has been made possible, and the latest 20 years have witnessed an outbreak in the number of available models. Figure 1.4a shows that, especially for the smallest species, the number

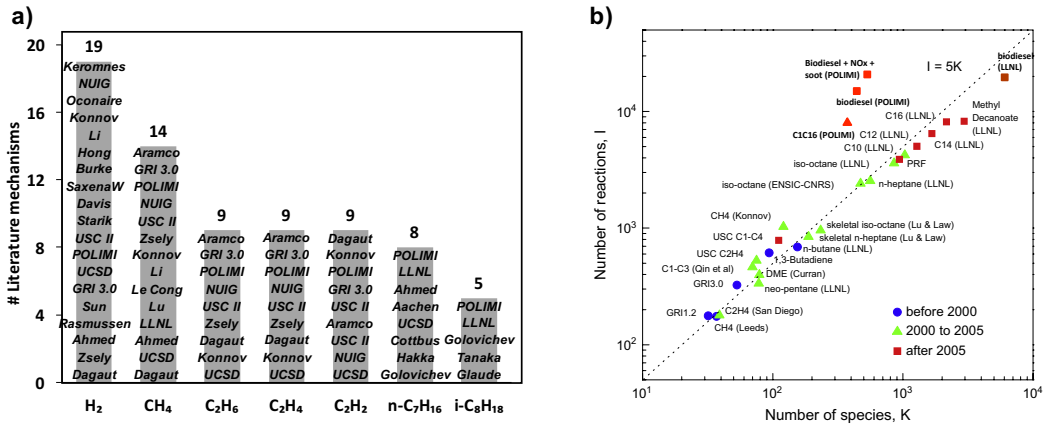

Figure 1.4: a) Number of kinetic mechanisms available in literature for the different fuels. b) Size and age of the different mechanisms. Adapted from Lu and Law [10].

of developed mechanisms is O(10). The most recent extensions (Figure 1.4b) allowed to consider the heaviest liquid fuels and surrogates, thus covering the whole range of gasoline, jet and diesel applications. In addition, the introduction of bio-derived fuels in the transportation market, like alcohols and methyl esters for gasoline and engine applications has recently required proper kinetic extension to consider the related dynamics of combustion. Indeed, it must be highlighted that their peculiar chemical features due to their oxygenation have important implications on the formation of such compounds, like aldehydes, whose effects on human health are still under debate.

As a result, detailed mechanisms are now extensively adopted to perform predictive simulations in order to improve the current devices and develop new combustion concepts. With the final targets of higher efficiencies and lower emissions, little-explored areas like low-temperature [11] or flameless (MILD) [12] combustion regimes can be deeply investigated. Here, the mentioned flexibility of numerical instruments proves essential, since quick (and cost-effective) parametric analyses to the kinetic and fluid dynamic settings can better characterize such regimes, as well as design new, targeted experimental campaigns in the regions where they are really needed.

Yet, in spite of the promising potential, such scenario shows one major drawback: even with the current computational capability, in several cases the use of detailed combustion mechanisms in Computational Fluid Dynamic (CFD) applications is limited by their size, in terms of number of species and reactions. Kinetic mechanisms introduce a computational weight proportional to the number of species according to a power law, whose exponent is between 2 and 3. Indeed, one transport equation must be added per each species, and the construc-

tion and factorization of Jacobian matrices, required in the resolution of dynamic and steady-state problems, respectively scale with second and third power [13]. Therefore, when associated to a particularly demanding application, obtaining results in acceptable times may be impossible. An extreme example is set by their application in reacting-flow Direct Numerical Simulations (DNS), which have been able to obtain fundamental insight on the flame/turbulence interaction, providing useful information for the improvement of turbulent combustion models. As reviewed by Poinsot and Veynante [14], starting from early 2000s the introduction of massively parallel architectures made the use of complex chemistry viable in such calculations. Yet, to date no more than ~120 species have been used, in simulations requiring $O(10^6)$ CPU hours [15]. Although to a lower extent, the same issues can be met also in smaller problems. As a matter of fact, even the evaluation of a laminar flame speed, i.e. a 1-dimensional problem, may require weeks with a serial solver if more than ~400 species are used [16]. In the light of this, the practical impossibility to use most of the detailed kinetic mechanisms indicated in Figure 1.4b in the simulations of interest becomes apparent, and their simplification turns out as a necessary step for their actual exploitation.

1.2 Aim and structure of the Thesis

The described background highlights the strong need for a trade-off between the size of a mechanism and its level of detail. Mechanism reduction is an established field of research, and the first works on this regard were written in the early 90s [17,18]. Yet, in spite of the remarkable acceleration occurred in this area in the last decade, obtaining kinetic mechanisms of the proper size is still a challenging task. More important, it has been shown [19] that a single reduction methodology is often not enough to achieve the desired size, also retaining sufficient accuracy.

The purpose of the Thesis stems from this last consideration. Starting from the available state of the art, a systematic, generalized and multistep methodology for mechanism reduction has been implemented and successfully applied. Revolving around this core, the structure of the Thesis is organized as follows, and is depicted in Figure 1.5. Chapter 2 provides an overview of (i) the automatic approaches to mechanism generation and management of a large number of species and reactions, (ii) chemical lumping and (iii) skeletal reduction techniques. Also, it shows how the combination of (ii) and (iii) can be effectively combined in a single methodology. Afterwards, Chapter 3 describes the second theoretical cornerstone of this work: the development of the Curve Matching framework for the comparison between models and/or experiments is described in detail, starting

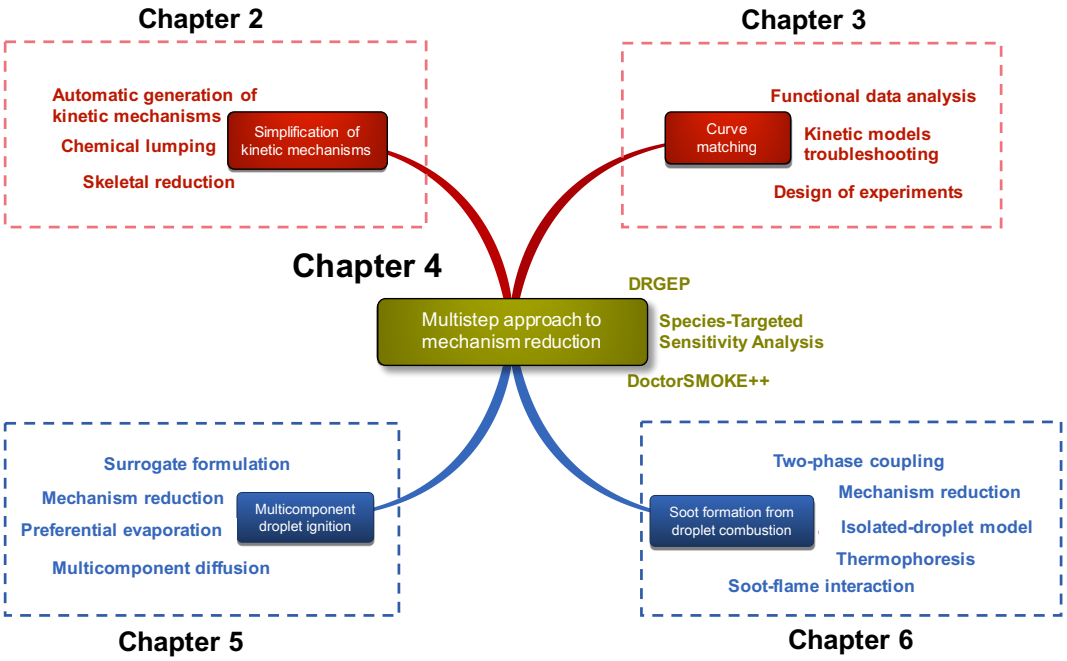

Figure 1.5: Structure of the Thesis.

from its theoretical foundations relying on functional data analysis, then progressively guiding the reader to the procedure to quantify such error and to leverage the obtained information for troubleshooting kinetic models and designing experiments in critical regions. The effectiveness of the whole methodology is shown through a comparison of several *n*-heptane mechanisms currently available in literature. The methods and procedures described in Chapters 2 and 3 are then incorporated in the overall reduction framework, illustrated in Chapter 4. Here, the Curve Matching approach is applied to the multistep procedure to implement a Species-Targeted Sensitivity Analysis, through which reduced mechanisms retaining accuracy on the dynamics of formation of specific species, like pollutants, can be obtained. Moreover, the implementation of the reduction framework in one single software, named `DoctorSMOKE++`, is outlined. Applications to fuels, fuel surrogates and NO_x mechanisms show the effectiveness of the proposed methodologies. `DoctorSMOKE++` is then adopted as the necessary starting point for two specific, computationally demanding applications deserving dedicated attention in the successive two Chapters. Chapter 5 describes a theoretical, parametric study aimed at quantifying the role of preferential evaporation on the ignition of surrogate fuel droplets in a homogeneous environment. Here, the simplification of the kinetic mechanism has allowed to use a higher detail in the other submodels, which are often overmuch simplified in the CFD simulations, like two-phase equilibrium

and liquid internal diffusion. Last, Chapter 6 shows how the obtained framework is extended to obtain a reduced mechanism describing soot formation. This is then applied to another two-phase problem, i.e. the analysis of soot dynamics in the combustion of isolated droplets. In particular, the soot-flame interaction and the role of thermophoretic effect are investigated. Finally, conclusions on the activity carried out are drawn in Chapter 7, where future developments and applications are proposed.

CHAPTER 2

Simplification of kinetic mechanisms

It has been already explained that the strong nonlinearity of combustion phenomena prevents the use of simplified one- (or few-) step kinetic models in a predictive way, even for the simplest reacting systems like those involving hydrogen and air [20]. As a consequence, the field of chemical kinetics has been a very active research streamline in the latest decades, and several mechanisms were developed by different schools for the combustion of the most varied hydrocarbon fuels. Also, it has been pointed out that the introduction of detailed kinetic mechanisms in combustion chemistry has brought about several complications in combustion simulations.

The first issue is expectably related to their dimension, which increases exponentially with the size of the involved fuels. Altgelt and Boduszynski [21] showed that, if all the branched alkane isomers are considered, the number of involved molecules may be higher than hundreds of thousands for hydrocarbons up to C_{20}. Table 2.1 shows a sample calculation by considering only the paraffin isomers. If one also considers that liquid fuels include other classes of compounds (olefins, aromatics, cyclo-alkanes, etc.) the impossibility of a kinetic modeling of the fuel mixture at this level of detail becomes apparent.

The second complication arises from the number of reactions. Lu and Law [10]

C atoms	Paraffin isomers	Petroleum fraction
8	18	Gasoline and naphthas
10	75	Kerosene
12	355	Jet fuels
15	4347	Diesel fuels
20	$3.66 \cdot 10^5$	Light gasoil
25	$3.67 \cdot 10^7$	Gasoil
30	$4.11 \cdot 10^9$	Heavy gasoil
35	$4.93 \cdot 10^{11}$	Atmospheric residue

Table 2.1: Number of structural paraffin isomers as a function of chain length [21].

showed that in most kinetic mechanisms, there are about 5 reactions per each species. Nevertheless, this approximately constant trend is the result of upstream simplifications on the reaction paths, since the larger size of a molecule results in a higher number of reactions which can involve the molecule itself; therefore, if all reaction paths were considered, reactions would increase more than linearly with the number of species. Beyond the resulting higher computational load and memory consumption, the main outcome is the practical impossibility of a manual compilation of the chemical mechanism, with the need of an automatic procedure for generating reaction parameters.

Last, but not less important, the large number of involved species interact each other in a wide range of time scales. As a result, the numerical problems to be faced are computationally stiff, requiring *ad hoc* numerical approaches and/or proper methods for the stiffness reduction.

These topics have been, and still are, a very active field of research. In this Chapter, an overview of the main strategies to tackle the mentioned issues are provided. Specifically, Section 2.1 illustrates the state-of-the-art techniques to automatically generate kinetic mechanisms. The remaining part of the Chapter is devoted to describing the developed techniques targeted at reducing the problem size and complexity: chemical lumping procedures are the focus of Section 2.2, while the approaches for the generation of skeletal mechanisms are described in Section 2.3.

2.1 Automatic generation of chemical mechanisms

The automatic generation of chemical mechanisms was first proposed by Chevalier et al. [22]. They created a LISP-based [23] computational framework able to identify the species produced, the reactions between species and the related

elementary reaction rates. The core of such a methodology was the identification of the reaction types (or classes), which are common to all the involved species. Once this step is completed, the rate constants for the different reaction classes can be evaluated by using a set of independent kinetic parameters describing the elementary acts. They can be derived either from the available literature [24–27], or through similarity and analogy rules. This approach was further investigated in successive works [28–34]; a detailed review of the underlying working principles has been recently carried out by Battin-Leclerc and coworkers [35].

Within a reaction-classes approach, the starting point is defining the classes involving the fuel molecules:

- Initiation reactions, by which the fuel molecule undergoes a C–C bond breakage and two radicals are produced:

$$\text{Fuel} \rightarrow \text{R}\cdot + \text{R}'\cdot$$

- H-abstraction (or metathesis) reactions, which occur when a radical abstracts a hydrogen atom from a stable molecule, thus propagating the chain radical reactions. In this case, a C–H bond is broken, while a second one is formed:

$$\text{R}\cdot + \text{R}'\text{H} \rightarrow \text{RH} + \text{R}'\cdot$$

The resulting alkyl-radicals undergo a wide range of possible reactions, which may be grouped in a number of classes. Their choice is arbitrary: Curran et al. [36,37] structured *n*-heptane and iso-octane reaction mechanisms into 25 major classes. Other approaches were proposed in different contexts [38–40]. A more simplified framework was set up by Ranzi and coworkers [41], who initially based their mechanism on 10 reaction classes. This number has also been recently increased [42] following the new experimental discoveries in the low-temperature oxidation pathways and reaction intermediates. The primary propagation reaction classes are listed in Table 2.2. Regardless of the class definition, the main advantage of such an approach lies in the possibility to apply the same rate rules to all the similar fuels in a systematic and structured way. As a result, mechanism generation can be easily implemented into a numerical algorithm [43] providing an automatic output according to the defined rules.

Table 2.3 shows the resulting number of propagating radicals for the different starting fuels: concerning *n*-heptane , i.e. the smallest species used for representing real fuels behavior, 38 intermediate radicals and 26 primary products (retaining *n*-heptane structure) would be needed to fully describe its oxidation

Reaction class	Description	Generic form
R1	Alkyl-radical decomposition	$R\cdot \rightarrow R'\cdot + C_nH_{2n}$
R2	Alkyl-radical isomerization	$R\cdot \leftrightarrow R'\cdot$
R3	O_2 H-abstraction	$R\cdot + O_2 \rightarrow C_nH_{2n} + HO_2\cdot$
R4	O_2 Addition	$R\cdot + O_2 \rightarrow ROO\cdot$
R5	ROO· internal isom. to QOOH·	$ROO\cdot \leftrightarrow QOOH\cdot$
R6	QOOH· decomp. to C_nH_{2n} and RCOH	$QOOH\cdot \rightarrow C_nH_{2n} + RCOH$
R7	QOOH· decomp. to conjugate C_nH_{2n}	$QOOH\cdot \rightarrow C_nH_{2n} + HO_2\cdot$
R8	QOOH· decomp. to cyclic ethers	$QOOH\cdot \rightarrow$ cyclic ether $+ OH\cdot$
R9	O_2 addition to QOOH·	$QOOH\cdot + O_2 \rightarrow \cdot OOQOOH$
R10	·OOQOOH decomp. to OQOOH	$\cdot OOQOOH \rightarrow OQOOH + OH\cdot$

Table 2.2: Primary propagation reactions for *n*-alkanes oxidation. From [41].

	Primary propagating radical				Primary product				
Fuel	R·	ROO·	·QOOH	·OOQOOH	Alkene	Cyclic ether	ROOH	OQOOH	Total
C_7H_{16}	4	4	15	15	3	8	4	15	68
$C_{10}H_{22}$	5	5	24	24	5	13	5	24	105
$C_{12}H_{26}$	6	6	30	30	6	16	6	30	130
$C_{14}H_{30}$	7	7	36	36	7	19	7	36	155
$C_{16}H_{34}$	8	8	42	42	8	22	8	42	180

Table 2.3: Primary radicals and products involved in n-alkanes oxidation.

path. Combined with the parallel pyrolysis and oxidation paths of the smallest molecules, the overall number of compounds becomes significant. The *n*-heptane mechanism developed by Curran and coworkers [36] at Lawrence Livermore National Laboratory (LLNL) is made up of 537 species and 4383 reactions. Table 2.4 lists the dimensions of the mechanisms for heavier n-alkanes, growing more than linearly with fuel size. Moreover, *n*-alkane fuels own the advantage of being simmetrical, which halves the number of intermediate species; when simmetry lacks, the overall size further increases. The biodiesel mechanism of Westbrook et al. [44], describing the pyrolysis and oxidation of methyl stearate, methyl oleate, methyl linoleate, methyl linolenate, and methyl palmitate, is made up of about 4,800 species and 20,000 reactions.

The introduction of automatic approaches to the formulation of kinetic mechanisms has allowed an easier and more structured management of the huge number of species and reactions rates. On the other hand, their integration into large-

Fuel	$C_{10}H_{22}$	$C_{12}H_{26}$	$C_{14}H_{30}$	$C_{16}H_{34}$
species	940	1282	1668	2116
reactions	3878	5030	6449	8130

Table 2.4: Size of LLNL n-alkanes submechanisms [45].

scale simulations is almost impossible because of the excessive computational cost. Therefore, in this form detailed mechanisms are of scarce applicability even in 1-dimensional simulations.

2.2 Chemical lumping procedures

Simplifying techniques are compulsory when the information contained in such mechanisms is to be exploited in multidimensional simulations. One of the most used approaches in chemical kinetics is based on species lumping, i.e. grouping them in a smaller number of pseudo-compounds, thus reducing the number of system variables. As discussed by Huang and coworkers [46], species lumping is a well-established technique in model reduction, with applications in several fields (catalytic cracking [47] and atmospheric chemistry [48], in addition to combustion itself [17, 49–51]). Although in different ways, they have to face three main issues: (i) determining which species are to be lumped; (ii) classifying how the original species contribute to the lumped ones, i.e. defining the lumping transformation; (iii) estimating kinetic parameters for the lumped species. As a result, two classes of approaches can be identified: chemical lumping methods [29,47], through which species are grouped according to their chemical structure or reactivity; and mathematically based approaches [46, 52], where formal rules for the transformation between original and lumped variables are defined.

Specifically, a chemical lumping methodology was conceived by Ranzi and coworkers [29]. Such an approach was targeted at reducing the number of intermediate species throughout the pyrolysis and oxidation paths, without sacrificing the descriptive capability. In such a way, detailed models can be extended to heavier compounds via a hierarchical approach, with a modest (linear) increase in the overall size of the mechanism. The procedure lies on the physically sound assumption that at high temperatures, the interactions between alkyl radicals heavier than C_4 and the reacting mixture are very weak: therefore, they can be directly replaced with their decomposition and isomerization products. By assuming a steady state for intermediate radicals, the product distributions (i.e. selectivities) can be calculated by solving the related linear system of continuity

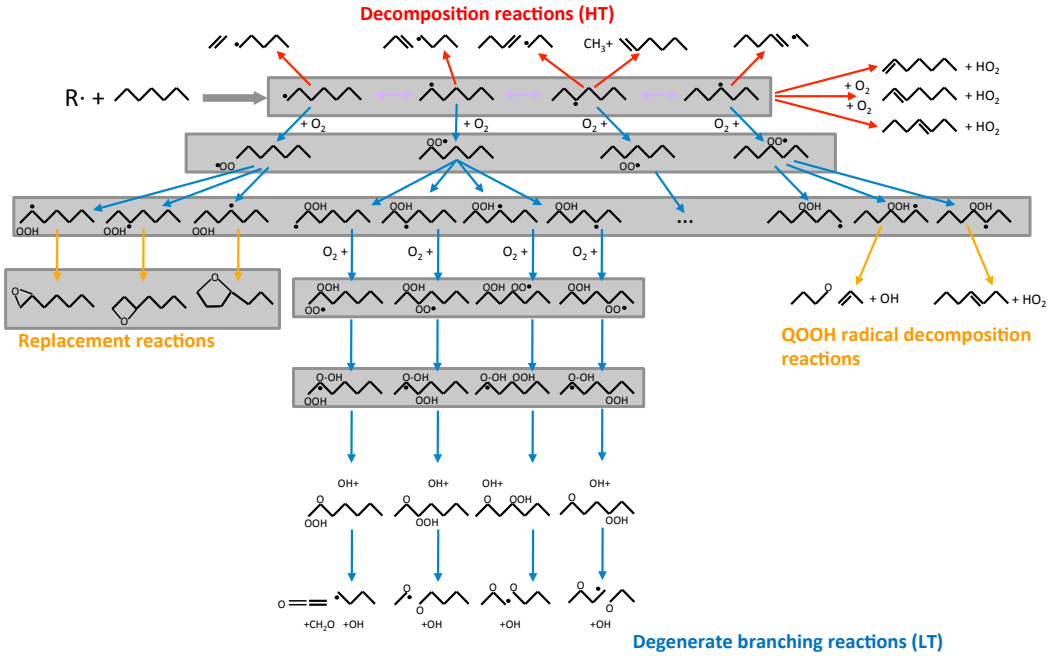

Figure 2.1: Species lumping in the pyrolisis and oxidation paths of n-heptane. Adapted from [29].

equations. For the heptyl radicals, one would have a 4x4 linear system:

$$r_j\left(0\right)+\sum_{i\neq j}k_{ij}R_i^{C_7}-\left(\sum_{i\neq j}k_{ij}+k_{dj}\right)R_j^{C_7}=0\quad j=1\ldots4 \tag{2.1}$$

where $r_j(0)$ is the direct formation rate of heptyl radical $R_j^{C_7}$, k_{dj} is the total rate constant for the decomposition reaction of $R_j^{C_7}$, and k_{ij} is the rate constant for the $R_i^{C_7} \leftrightarrow R_j^{C_7}$ reaction of isomerization. Once the values of $R_i^{C_7}$ are evaluated, a single lumped reaction can be set for the (lumped) heptyl radical:

$$\begin{aligned}\mathrm{C_7H_{15}} \rightarrow\ & 0.17\mathrm{C_2H_4}+0.17\mathrm{C_5H_{11}}+0.43\mathrm{C_3H_6}+0.43\mathrm{C_4H_9}+0.20\mathrm{C_4H_8}+\\ & +0.20\mathrm{C_3H_7}+0.16\mathrm{C_5H_{10}}+0.16\mathrm{C_2H_5}+0.04\mathrm{C_6H_{12}}+0.04\mathrm{CH_3}\end{aligned} \tag{2.2}$$

Such a stoichiometry is not theoretically independent of temperature. Nevertheless, it can be shown that it is a weak function of it [29]. Therefore, a reference value at an average temperature can be chosen, and it can be then kept fixed. Figure 2.1 schematically shows the lumping procedure, as applied in the case of *n*-heptane to all the intermediate radicals.

The lumped kinetic constants are derived through an optimization process, aimed at minimizing the deviation in the selectivities of the final products between

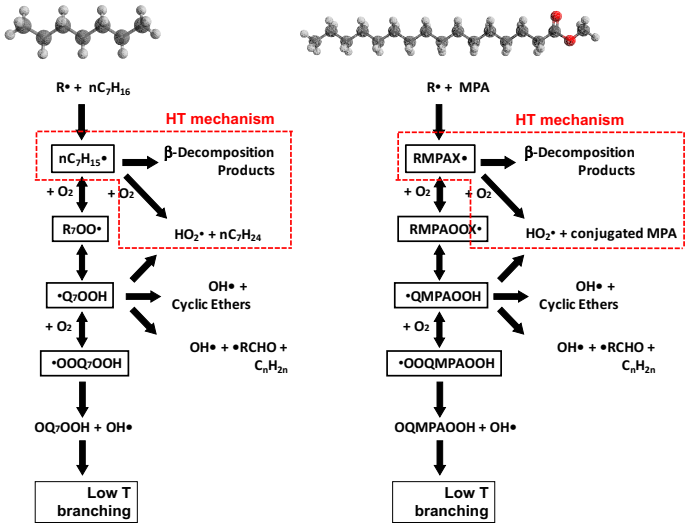

Figure 2.2: Analogy between lumped pyrolysis and oxidation mechanisms of (left) n-heptane and (right) methyl-palmitate.

the original and the lumped mechanism. The corresponding error function (2.3) is minimized:

$$\varepsilon\left(\mathbf{k}\right) = \int_{P_0}^{P} \int_{T_0}^{T} \sum_{j=1}^{n} \left[\sigma_{det,j} - \sigma_{lumped,j}\left(\mathbf{k}\right)\right]^2 dT dP \tag{2.3}$$

where n is the number of products, $\mathbf{k}$ is the vector of lumped kinetic constants, and σ_j the product selectivities. Regardless of the size of the considered fuel, the number of intermediate radicals and compounds is therefore reduced to 1 per class. Above all, the number of species constituting the kinetic mechanism increases linearly with the number of added fuels, and no longer exponentially with the fuel size. Figure 2.2 shows the analogy between the lumped oxidation paths of n-heptane (C_7H_{16}) and methyl palmitate ($C_{17}H_{34}O_2$), in spite of the large difference in size.

Downstream of this procedure, further reduction can be achieved by avoiding to include all the fuels of a given class (n-alkanes, iso-alkanes, alkenes, etc.) in the lumped mechanism. As a matter of fact, a similar chemical behavior can be observed in the same family of fuels: therefore, even if only some reference species of a family are included, the excluded ones can still be represented by splitting them between the closest two through the lever rule. Figure 2.3 shows this procedure, known as "vertical lumping", for three sample fuels. The combination of the two mentioned techniques results in significant savings in the overall size of the mechanism: as a representative example, the POLIMI lumped mechanism for Primary Reference Fuels (PRF) [53] is made up of 300 species and 11790

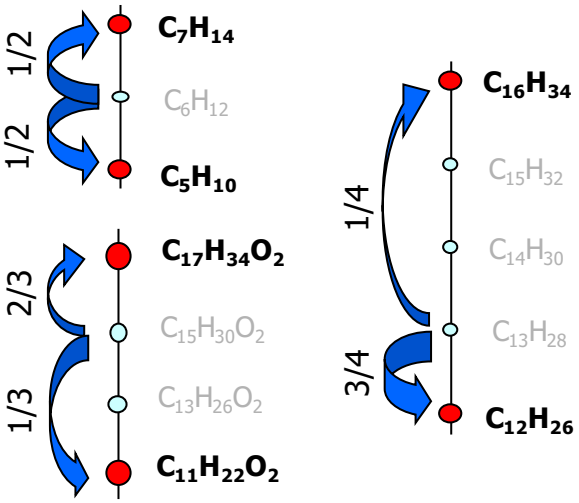

Figure 2.3: Modeling of intermediate fuels through vertical lumping. Top left: n-hexane. Bottom left: methyl myristate. Right: tridecane.

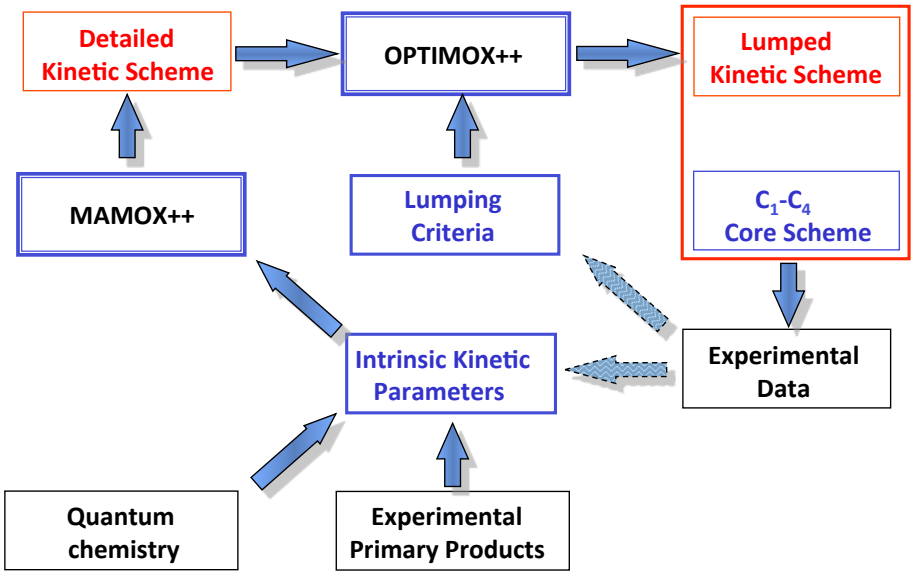

Figure 2.4: Block diagram of the lumped mechanism development. After Ranzi et al. [29].

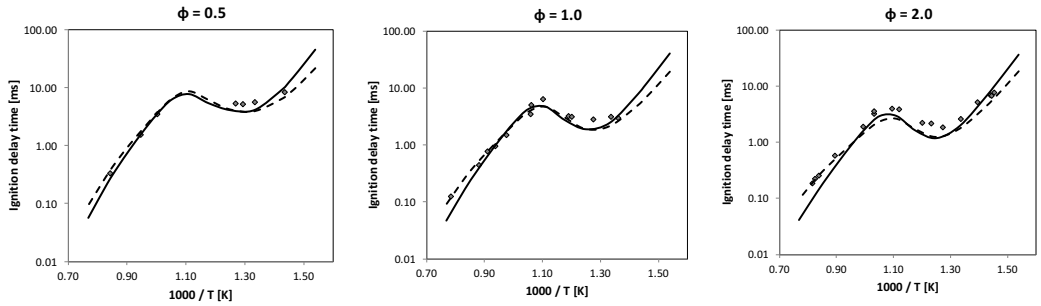

Figure 2.5: Ignition delay times of n-heptane/air mixture at 13.5 atm. Continuous lines: POLIMI lumped mechanism. Dashed lines: LLNL detailed mechanism. Symbols: experimental data [56].

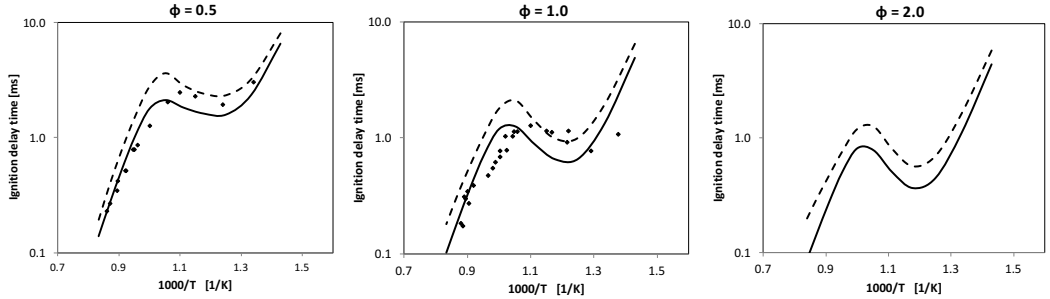

Figure 2.6: Ignition delay times of n-dodecane/air mixture at 20 atm. Continuous lines: POLIMI lumped mechanism. Dashed lines: LLNL detailed mechanism. Symbols: experimental data [57] (not available for $\Phi = 2$).

reactions. Conversely, the same LLNL detailed mechanism [54] includes 1389 species and 10481 reactions.

Such a different size does not imply a lower degree of accuracy. As an illustrative example [55], the output provided by POLIMI lumped kinetic models of *n*-heptane and *n*-dodecane [9] was compared with experimental data and with the corresponding predictions provided by the LLNL detailed mechanism of Westbrook et al. [45]. Figures 2.5 and 2.6 compare the ignition delay times of *n*-heptane and *n*-dodecane, respectively. Apparently, both the kinetic mechanisms properly account for low and high temperature reactivity. Differences are present between them, but they (i) are of the same order of the experimental uncertainties and (ii) can be attributed to a different core $C_0 - C_4$ sub-mechanism, which they lie on. Speciation is properly described, too, as shown by further comparisons. Figure 2.7 shows the dynamic species profile in a shock-tube reactor, thus reproducing the experimental setup of Davidson et al. [58], while Figures 2.8 and 2.9 show conversion and CO/CO_2 formation in an isothermal Jet Stirred reactor, as a function of temperature. Last, Figure 2.10 compares the laminar flame speed measurements of the same *n*-alkanes with the values predicted by POLIMI mech-

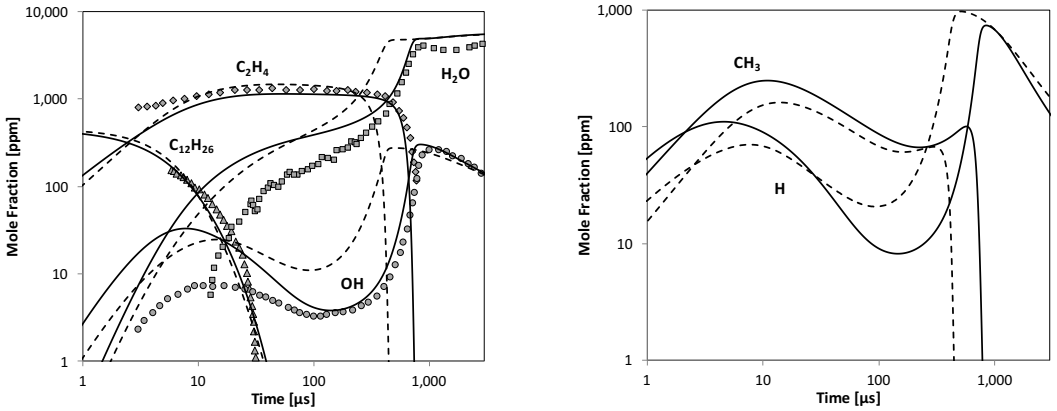

Figure 2.7: Species time history for *n*-dodecane oxidation in a shock-tube reactor. Nominal initial conditions: T = 1410 K, P = 2.3 atm, $x_{C_{12}}$= 457 ppm in a O_2/Ar system at stoichiometric ratio. Continuous lines: POLIMI lumped mechanism. Dashed lines: LLNL detailed mechanism. Symbols: experimental data [58].

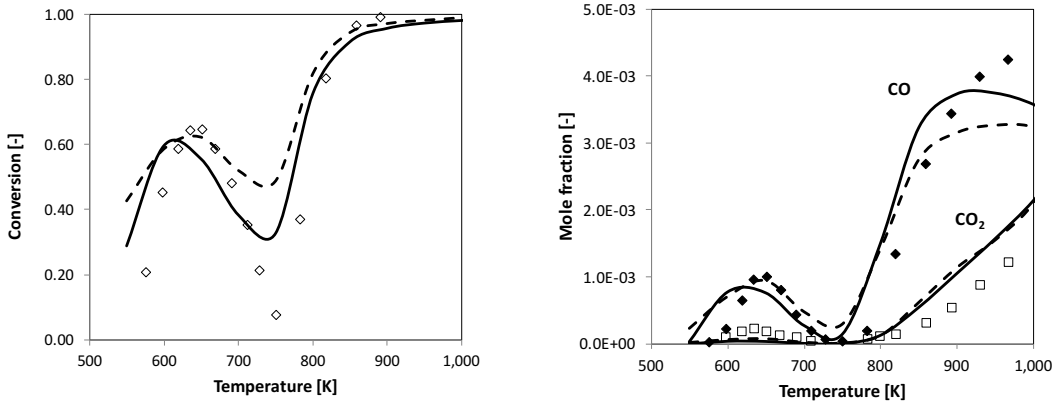

Figure 2.8: *n*-heptane oxidation in a jet stirred reactor at P = 10 bar and $\tau = 1\,s$. Continuous lines: POLIMI lumped mechanism. Dashed lines: LLNL detailed mechanism. Symbols: experimental data [59].

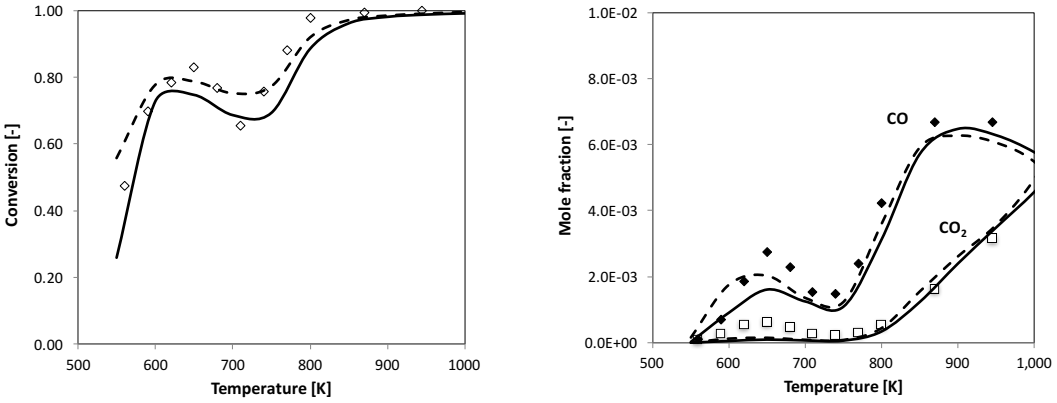

Figure 2.9: *n*-dodecane oxidation in a jet stirred reactor at P = 10 bar and $\tau = 1\,s$. Continuous lines: POLIMI lumped mechanism. Dashed lines: LLNL detailed mechanism. Symbols: experimental data [60].

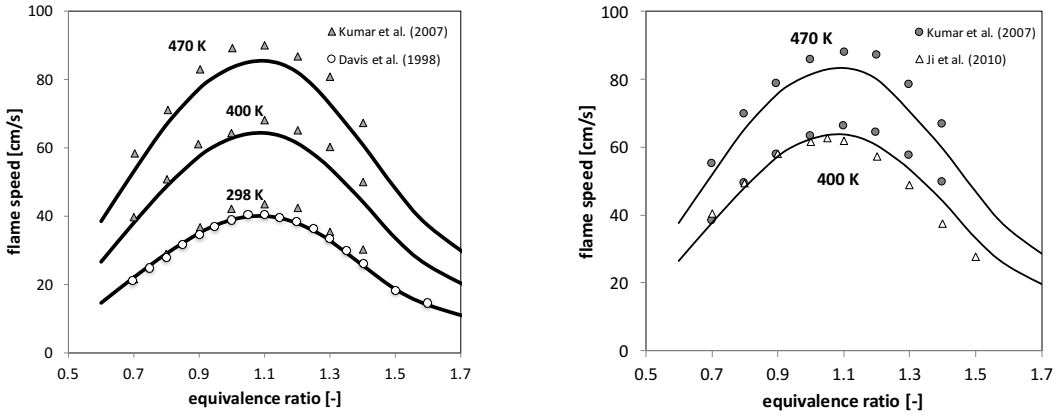

Figure 2.10: Laminar flame speeds of (left) *n*-heptane/air and (right) *n*-dodecane/air mixtures at atmospheric pressure. Experimental data from [62–64]. Simulations carried out with POLIMI mechanism.

anism. Besides the satisfactory agreement between experiments and predictions, what is worth highlighting is the impossibility of carrying out the same simulations with the LLNL mechanism, due to the excessive size of the mechanism. Such an issue has been met several times in literature [17, 61] with detailed mechanisms: in such cases, 1D computations were carried out through either through parallel codes, or by adopting simplifying approaches, like skeletal reduction.

2.3 Skeletal reduction

Skeletal reduction approaches have the common purpose of detecting and eliminating, from a kinetic mechanism, those species and/or reactions which are classified as unimportant in the targeted operating space of temperature, pressure and equivalence ratio. The identification of negligible reactions is usually more straightforward, and several approaches were developed since the 80s. Wang and Frenklach [18] proposed the "detailed reduction" methodology, while approaches based on sensitivity analysis were proposed by Rabitz et al. [65] and Tomlin et al. [66]. Reaction elimination was also carried out by Vajda et al. [67], followed by Brown and coworkers [68] via Principal Component Analysis (PCA) technique. Other reaction-based approaches include the Computational Singular Perturbation (CSP) [69] or genetic algorithm optimization [70].

On the other hand, the identification of unimportant species is a higher challenge because of the frequent mutual coupling. Yet, it is the most effective approach since it directly reduces the number of variables, and the computational cost is proportional to the number of species according to a power law, as already said. Therefore, most of the recent efforts have focused in this direction. The

most significant works in this field have been based on sensitivity analysis [71,72], the analysis of the Jacobian matrix [73, 74], and in the last decade, flux analysis. The Directed Relation Graph (DRG) developed by Lu and Law [75] was the first of this class, and was then followed by alternative approaches like DRG with Error Propagation (DRGEP) [76], Path Flux Analysis (PFA) [77] and Reacting Flux Analysis (RFA) [55]. Regardless of the implementation, flux-based approaches create a species ranking in such a way to remove them starting from those with the lowest value. DRG accomplishes this purpose by transforming the kinetic mechanism into an equivalent graph: its vertices are constituted by the species, which are connected by edges, whose strength depends on the reactions linking them. On the other hand, PFA and RFA lie their methodology on the Production and Consumption rates. Regardless of the approach, the evaluation occurs by sampling reaction states in ideal reactors, either discontinuous (batch) or continuous (perfectly stirred). Therefore, the whole process is quite fast, and the computing time is of the same order as the resolution of ideal reactors.

The constitutive steps of a skeletal reduction methodology are here described in the context of the RFA approach. The RFA technique analyzes the behavior of the original mechanism in autoignition phenomena in ideal reactors, whose initial conditions are uniformly spread in the tridimensional space of temperature T, pressure P and equivalence ratio Φ where the mechanism is expected to work. For each reactor, the instantaneous production and consumption rates of the i-th species are evaluated as:

$$P_i = \sum_{i=1}^{N_R} \max(0, \nu_{i,j}\dot{\omega}_j) \tag{2.4}$$

$$C_i = \sum_{j=1}^{N_R} \max(0, -\nu_{i,j}\dot{\omega}_j) \tag{2.5}$$

where $\nu_{i,j}$ is the stoichiometric coefficient of the i-th species in the j-th reaction, N_R is the number of reactions and $\dot{\omega}_j$ the net reaction rate of the j-th reaction. The total flux of each species in each reactor is calculated as:

$$F_i = MW_i \int_0^{\tau} \left(P_i\left(t\right) + C_i\left(t\right)\right) dt \tag{2.6}$$

where MW_i is the i-th species molecular weight, and τ is the reactor residence time. After normalizing them with respect to the local maximum value, a subset of important species is found for each reactor by setting a local threshold. The final mechanism is obtained after merging all the subsets, and forcing the needed

Property	Range
T	600 – 1700 K
P	1 – 40 atm
Φ	0.5 – 2

Table 2.5: Engine-like operating conditions used to generate mechanisms for transportation fuels.

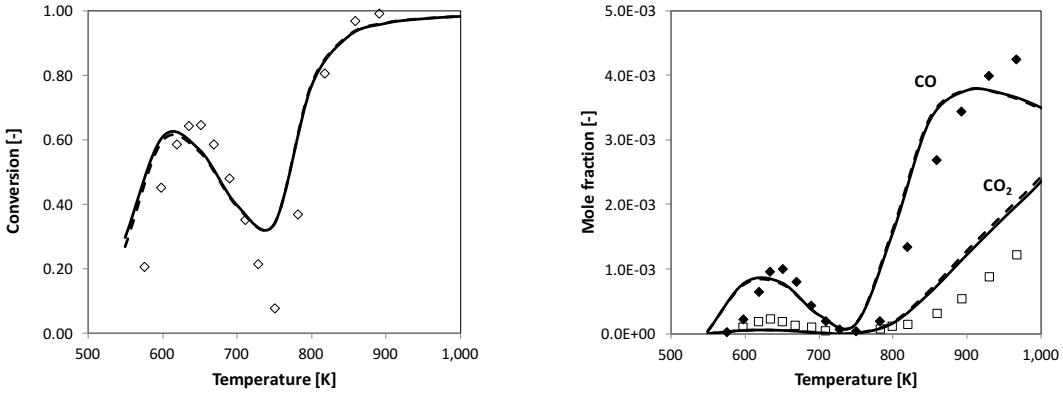

Figure 2.11: *n*-heptane oxidation in a jet stirred reactor at P = 10 bar and $\tau = 1$ s. Continuous lines: POLIMI lumped mechanism. Dashed lines: *n*-heptane skeletal mechanism [78]. Symbols: experimental data [59].

inert species.

Starting from the already described POLIMI mechanism, a *n*-heptane skeletal mechanism, developed in the operating conditions typical of an internal combustion engine (Table 2.5) consisted of 100 species and 1567 reactions. Figure 2.11 shows its application in the same simulations described in Figure 2.8. Apparently, with one third of the overall species, accuracy was preserved almost totally. Similar considerations are valid for *n*-dodecane: with the described procedure, a 120-species mechanism for the combustion of *n*-dodecane was obtained. Figure 2.9 shows that accuracy was satisfactorily retained in this case, too.

In order to understand the benefits and the importance of reducing detailed kinetic schemes for practical applications, the simulation of multidimensional flames was carried out, and the reduced kinetic mechanisms of *n*-heptane and *n*-dodecane was compared with the original lumped kinetic mechanism. Laminar conditions were chosen in order to avoid the complexity due to the numerical modeling of turbulence-chemistry interaction. The burner geometries adopted by Tosatto et al. [79] to carry out experimental and numerical studies of coflow flames fed with JP8 surrogates (Figure 2.13), were used. The inlet fuel was replaced with *n*-heptane or *n*-dodecane, keeping then fixed all the remaining boundary conditions.

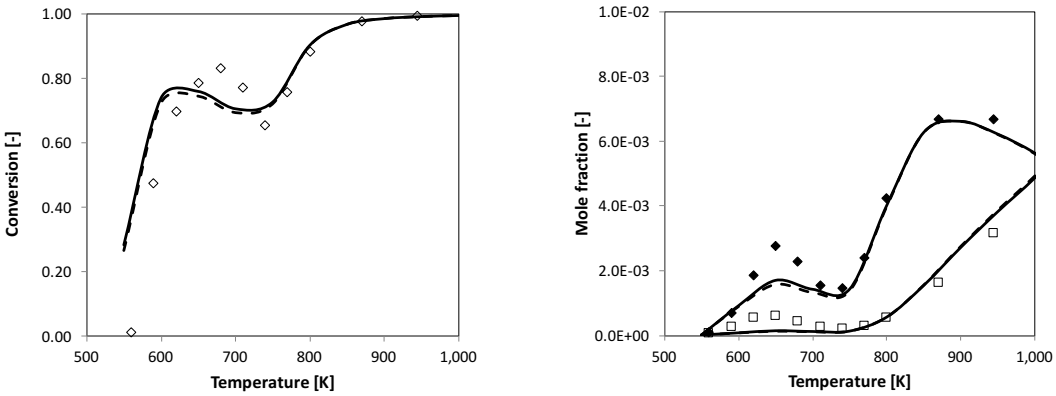

Figure 2.12: n-dodecane oxidation in a jet stirred reactor at P = 10 bar and $\tau = 1\ s$. Continuous lines: POLIMI lumped mechanism. Dashed lines: n-dodecane skeletal mechanism [78]. Symbols: experimental data [60].

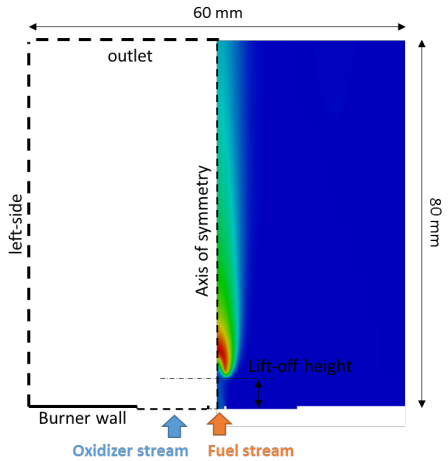

Figure 2.13: Laminar coflow flames: schematic of the diffusion flame setup, and dimensions of the computational domain.

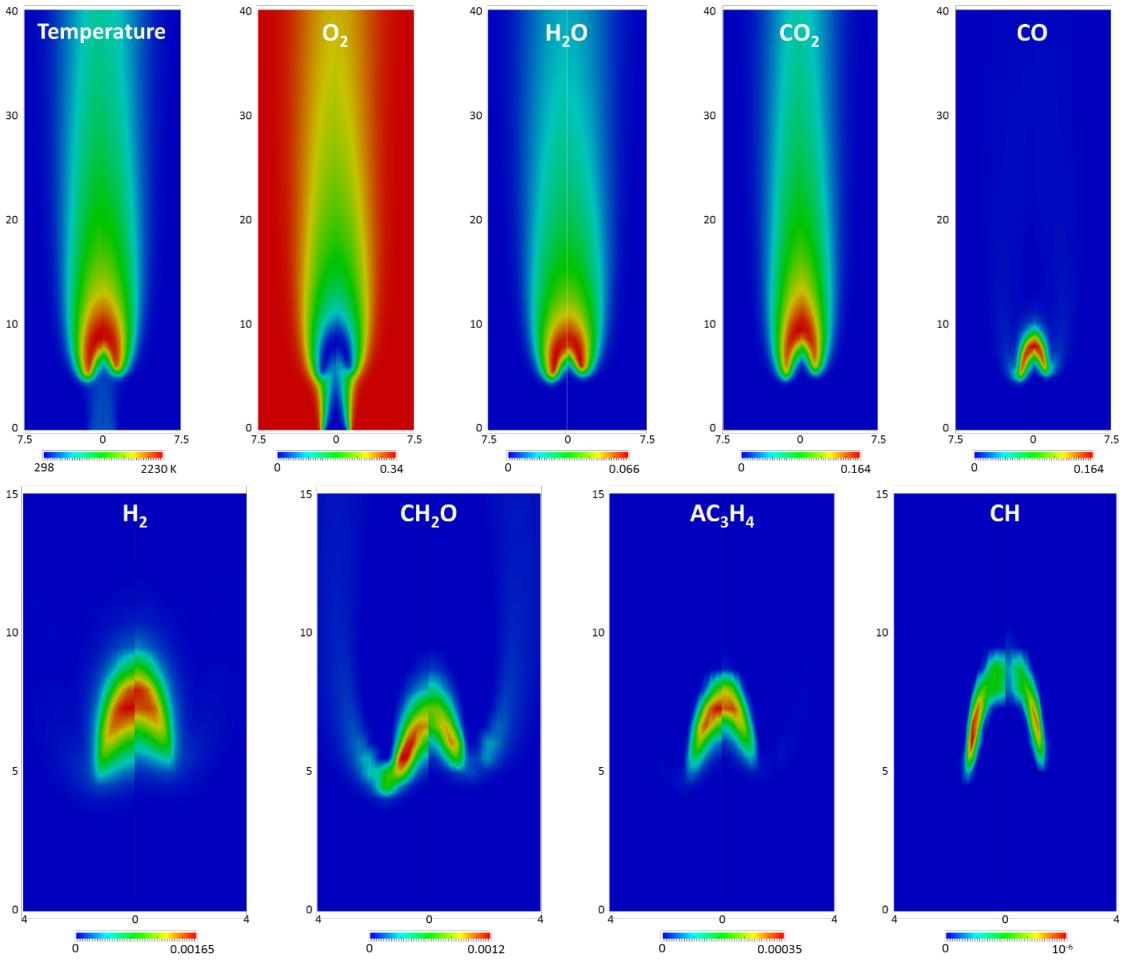

Figure 2.14: Maps of temperature and mass fractions of selected species for the coflow flame fed with *n*-heptane. Skeletal mechanism (left side) vs original methanism (right side). Coordinates in mm.

As a matter of fact, the ability to correctly capture the flame lift-off from a computational point of view is strongly dependent on the reliability and accuracy of the kinetic scheme [80]. Therefore, such kind of flames is a convenient test bench to investigate the quality of the reduced kinetic mechanisms. By using the `laminarSMOKE` computational framework [81], the steady-state equations, in a 2D axisymmetric computational domain, were solved, i.e. (i) Navier-Stokes mass and momentum conservation, (ii) energy balance and (iii) species conservation. Dirichlet boundary conditions were imposed at the fuel inlet, while Neumann conditions were imposed to represent the outflow. Figures 2.14 and 2.15 show the calculated maps of temperature and mass fractions of selected species for the *n*-heptane and *n*-dodecane flames, respectively. The skeletal mechanism results are in reasonable agreement with the original scheme, for temperature as well as major species (CO, CO_2, H_2O). Some discrepancies are present for minor species

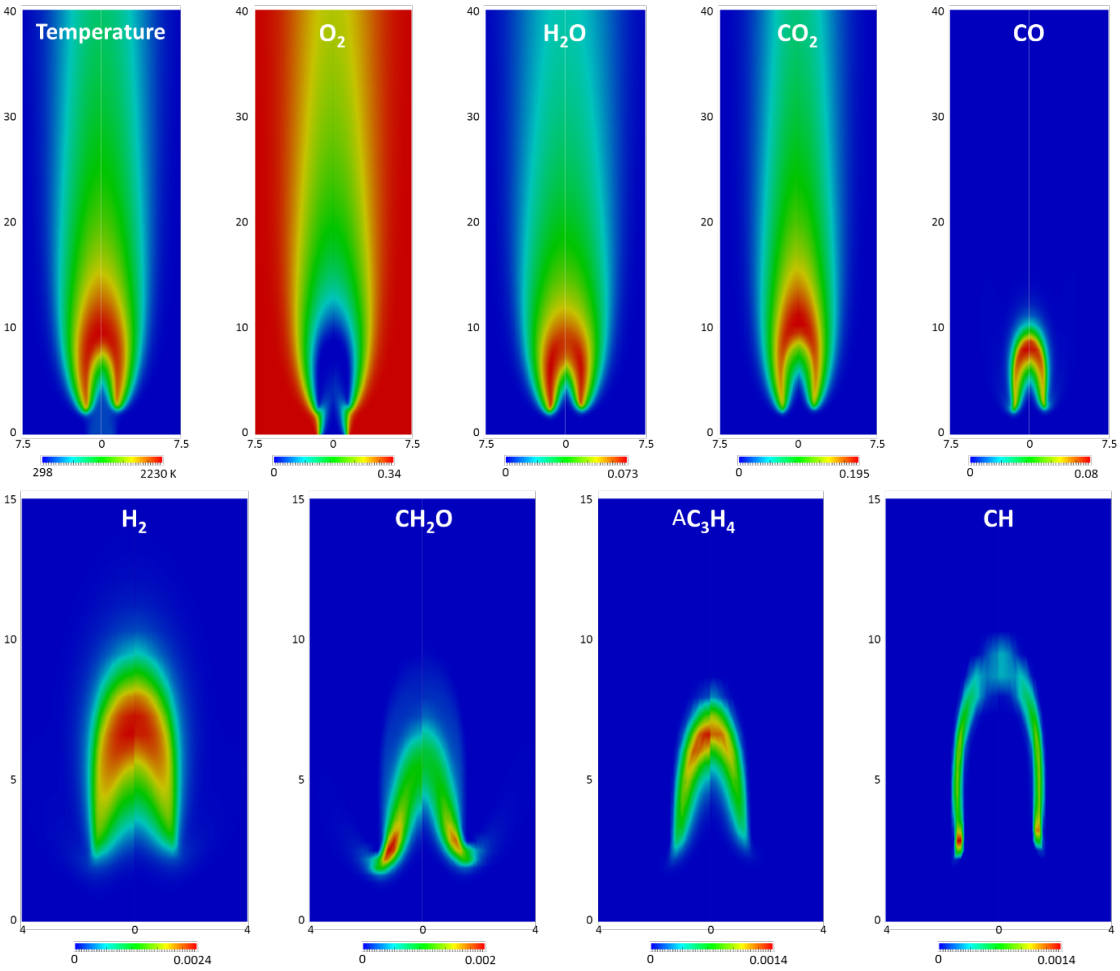

Figure 2.15: Maps of temperature and mass fractions of selected species for the coflow flame fed with *n*-dodecane. Skeletal mechanism (left side) vs original methanism (right side). Coordinates in mm.

Mechanism	Species	Reactions	*n*-heptane			*n*-dodecane		
			R	TP	T	R	TP	T
n-heptane	100	1567	11.66	0.67	2.75	-	-	-
n-dodecane	120	1930	-	-	-	17.92	0.95	3.92
HT1212	198	6274	76.52	2.62	11.09	77.59	2.51	11.35
TOT1212	435	13495	378.41	11.93	57.58	382.96	11.54	59.55
TOT1212NOX	466	14592	445.78	14.01	79.65	448.10	13.97	78.34

Table 2.6: CPU Times [Milliseconds per Single Cell] for the Different Parts of the `laminarSMOKE` code. R: reaction step. TP: Transport properties. T: Transport step.

like CH_2O and CH_4, but considering the simplicity of the reduction methodology, the agreement can be considered satisfactory and for both the flames, the skeletal mechanisms are able to correctly capture the O_2 entrainment at the flame. Appreciable results are obtained for the prediction of the flame lift-off height, too: the results for *n*-heptane flame (Figure 2.14) show that the reduced kinetic scheme predicts a lift-off height of 4.6 mm, while 5 mm are predicted by the original model. For the n-dodecane flame (Figure 2.15), the predicted lift-off heights are equal to 2.1 and 2.3 mm for the reduced and the original mechanisms, respectively.

Since the final goal of the whole reduction process is allowing to carry out reliable simulations of multidimensional systems in human times, a time benchmark was carried out on the two cases, and the CPU time consumption of the different steps was investigated. Indeed, the operator-splitting algorithm behind the `laminarSMOKE` solver is structured in three different phases:

i. The chemical step, where the local, stiff ODE systems are integrated over the chosen time-step;

ii. The calculation of transport properties (mass diffusion coefficients, thermal conductivity, dynamic viscosity, and thermal diffusion coefficients);

iii. The transport step, where the convection and diffusion terms are integrated along the whole time step.

Table 2.6 reports the computational costs for simulating on a single processor (Intel Xeon X5675 – 12Mb cache, 3.06 GHz, 6.40 GT/s Intel QPI) a time interval of 10^{-5} s on the whole mesh. The reaction step results to be the most consuming part of the code, independently of the kinetics, requiring more than 80−85% of the total computational time. More important, Figure 2.16 shows that, as already anticipated in the introduction, the CPU time of the reaction step increases with a power law, whose exponent is found to be around 2.4. Overall, the computa-

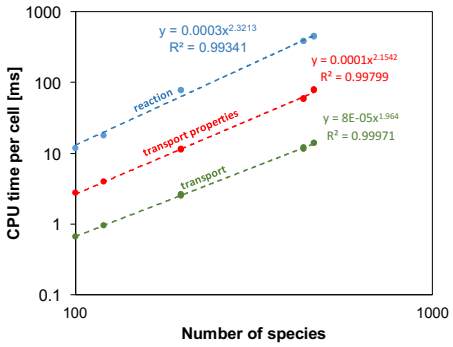

Figure 2.16: CPU times for the single cell for the different phases of the laminarSMOKE code for different number of species in the specific kinetic mechanism.

tional cost of the simulation carried out through n-dodecane skeletal mechanism is $\sim$23 times smaller than the original one. If such trends were only dependent on the number of species, the resolution time of n-dodecane flame with the already mentioned LLNL mechanism [45] would be $\sim$200 times higher than the skeletal kinetic mechanism (120 species).

2.4 Conclusions

Including detailed kinetic information within combustion simulations is a necessary step for their use in a predictive way. Nevertheless, especially when dealing with heavier fuels, kinetic mechanism simplification is a compulsory step to this purpose. After reviewing the state of the art, in this Chapter the advantages of a coupled, synergistic methodology including both lumping and skeletal reduction techniques have been shown. Starting from a detailed mechanism, compact schemes were generated for two sample alkanes, n-heptane and n-dodecane, which are widely used as part of surrogate mixtures, representative of real fuels [78]. Their dimensions are highly competitive with the size of similar models available today in literature [19], which do not exploit such a coupled approach. As a representative example, previous experience from skeletal mechanism generation [82] shows that the skeletal reduction of n-dodecane mechanism resulted in a 295-species mechanism, which was then further simplified through a downstream lumping approach, thus reaching a final size of 188 species. In this case, following the methodology devised by Pepiot-Desjardins and Pitsch [83], the isomers of radical species important in the low-temperature region were grouped according to the size of the ring involved in the transition state of the corresponding isomerization reactions, and a similar approach was carried out on cyclic ether and ketohydroperoxide isomers. This alternative strategy is summarized in Figure

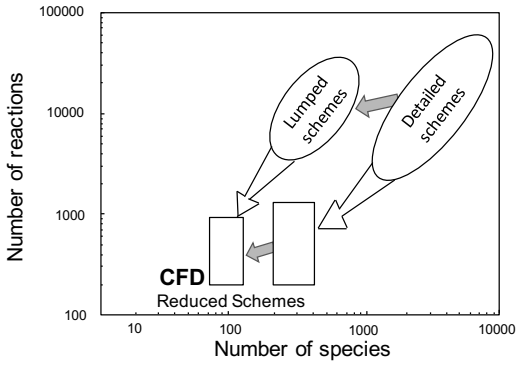

Figure 2.17: Strategies for the reduction of lumped and detailed kinetic schemes. Lumping phase is represented with grey arrows. Adapted from [78].

2.17, where it is represented beside the procedure adopted in this work. Apparently, the size of the skeletal mechanisms derived from lumped mechanisms are smaller than what is obtained by inverting the order of the two steps. Indeed, the major effect of lumping is a significant reduction of the number of species, either directly obtained during the automatic generation of the kinetic scheme or applied to the reduced model derived from the detailed ones. As a matter of fact, the great advantage of a direct use of lumping procedures when generating the detailed kinetic schemes is a simpler and more effective validation phase directly performed on the lumped mechanism.

A more refined reduction can still be obtained through more time consuming approaches, like those based on sensitivity analysis [19, 84] on specific targets, which will be described in Chapter 4. What accomplished here for *n*-heptane and *n*-dodecane is a starting point towards a more systematic reduction targeted at CFD applications. Also, it can be easily extended to multicomponent mixtures, like surrogate fuels, which are often used as physico-chemical representatives of real mixtures (gasoline, jet and diesel fuels). This is even more important for heavier complex fuels, like fuel oils or biofuels, where the number of possible isomers prevent any detailed descriptions of the oxidation. In this case, strong lumping procedures have to be adopted before and reduction techniques are also successively necessary. Here, a further degree of complexity is added because of the difficulty of a proper characterization of the reacting mixtures, which requires the formulation of surrogate mixtures; their modeling is a further challenge for lumping and reduction techniques.

CHAPTER 3

Curve matching: comparing models and experiments

The experimental datasets shown in Chapter 2 are only an example of the huge amount of information which are now available to the combustion community. Such data are of experimental or theoretical origin, and have been constantly increasing over time, as one may easily imagine. From an experimental point of view, the new techniques, like photoionization mass spectrometry, fluorescence or incandescence spectroscopy, high resolution transmission electron microscopy, fast repetition rate imaging diagnostic have been allowing the acquisition of data with higher and higher accuracy, and especially at a faster rate. From a modeling perspective, the exponential increase in available data is being driven by the seemingly endless increase in computer performances, which has made high performance computing a common instrument to carry out new classes of "numerical experiments", like quantum chemistry calculations; this has allowed a higher accuracy in the estimations of rate constants. The easy accessibility to fast and cheap Personal Computers has also contributed to an easier development of kinetic mechanisms for different fuels of different complexity, also thanks to the computer-aided automatic mechanism generation. As a result, it has been already

said that the number of available mechanisms has been exploiting since the early 2000s [10]. Moreover, the investigation towards alternative classes of fuels (e.g. ethanol, biomass, biodiesel) has catalysed such a growth from both sides, since it has further increased the pool of experimental data currently under collection, and has required the development of proper kinetic mechanisms.

As a major consequence of this twofold boost, the benchmark of a kinetic mechanism with respect to larger and larger experimental datasets takes now a significant part of the development of a kinetic model. This is not much related to the computational time to carry out the required simulations (which is constantly decreasing thanks to the constant hardware and software enhancements), but to the manual (and qualitative) accuracy check for all the involved simulations. This is true either when a mechanism is created from scratch, or when a part of it is updated, be it a kinetic subsection, but also thermodynamic [85] and transport properties. As a matter of fact, the hierarchical structure of a kinetic mechanism makes the pyrolysis and oxidation paths of larger molecules depending on the smaller ones. Therefore, the change in performance of mechanisms subsections not directly touched by such updates is not a remote possibility. As a result, comparing the actual improvements from one mechanism to the other is impossible in quantitative terms, and can only be done in a qualitative way, at the cost of huge amounts of time. Also, it must be pointed out that such updates to the kinetic mechanisms are becoming more and more frequent, because of the frenetic evolution of the energy background, fuel specifications and the increasingly stringent regulations on pollutants emissions.

In this scenario, it is immediately clear that the development of a systematic methodology to automatically assess and validate a kinetic mechanism is of utmost importance, since it would significantly decrease the human time required for that. Revolving around this necessity, this Chapter starts from describing the state of the art around this topic in Section 3.1. Then, the development of the generalized Curve Matching methodology is described in Section 3.2 and applied in Section 3.3. Final remarks are done in Section 3.4, where the activity is framed within the context of this Thesis.

3.1 State of the art

The traditional methodology for the validation of a kinetic mechanism has consisted in the graphical, qualitative comparison between experiments and models. The only attempt to use a systematic procedure to this purpose has recently been done by Olm and coworkers [86, 87], who applied it to the comparison of hydro-

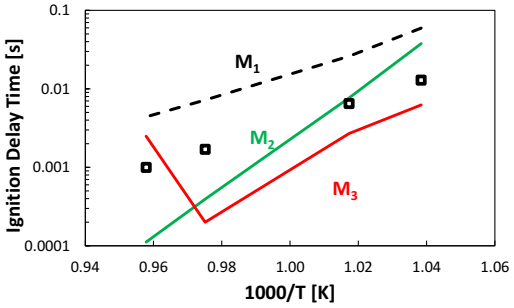

Figure 3.1: Ignition delay times of a stoichiometric hydrogen/air mixture at 50 bar. Predictions from 3 plausible models. Experimental data from Mittal et al. [88]. From [89].

gen and syngas combustion mechanisms. The core of such a procedure is based on the calculation of an average error function E and absolute deviation D for each model, obtained by averaging all the classes of case studies (i.e. ignition delay times, concentrations in jet stirred reactors, concentrations in flow reactors, laminar flame speeds). The average error function is defined as:

$$E = \frac{1}{N}\sum_{i=1}^{N}\left[\frac{1}{n_i}\sum_{j=1}^{n_i}\left(\frac{Y_{ij}^{\mathrm{sim}} - Y_{ij}^{exp}}{\sigma\left(Y_{ij}^{exp}\right)}\right)^2\right] \tag{3.1}$$

where N is the number of datasets, n_i the number of data within each dataset, and Y_{ij} is defined as:

$$Y_{ij} = \begin{cases} y_{ij} & \text{if } \sigma\left(\mathrm{y}_{\mathrm{ij}}^{\mathrm{exp}}\right) \approx \text{constant} \\ \ln\left(y_{ij}\right) & \text{if } \sigma\left(\ln\left(\mathrm{y}_{\mathrm{ij}}^{\mathrm{exp}}\right)\right) \approx \text{constant} \end{cases} \tag{3.2}$$

where y_{ij}^{exp} is the j-th experimental observation of the i-th dataset and $\sigma\left(y_{ij}^{exp}\right)$ its standard deviation. The deviation D is then defined as:

$$D = \frac{1}{N}\sum_{i=1}^{N}\left[\frac{1}{n_i}\sum_{j=1}^{n_i}\frac{Y_{ij}^{\mathrm{sim}} - Y_{ij}^{exp}}{\sigma\left(Y_{ij}^{exp}\right)}\right] \tag{3.3}$$

and is introduced in order to detect systematic under- $(D < 0)$ or over- $(D > 0)$ predictions.

This approach is very straightforward and robust, and is formally based on a total sum of squared deviations between model and experiments, normalized with respect to the standard deviation of experimental data. On the other hand, its simplicity results in a lack of critical interpretation of the trend of the single curves. As an illustrative example, Figure 3.1 shows the application of the Olm et al. procedure to the assessment of three plausible kinetic models in reproducing

Model	E	D
M_1	213	13
M_2	203	-6
M_3	168	-16

Table 3.1: Average error functions E and absolute deviations D for the three models reproducing experimental data in Figure 3.1.

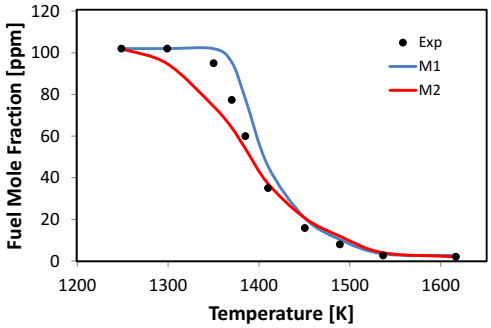

Figure 3.2: Typical mole fraction profile in isothermal reactor versus inlet temperature. Sample experiments (symbols) vs models (lines). From [89].

the ignition delay times of a hydrogen mixture in a rapid compression machine. From the results shown in Table 3.1, one could easily consider M_3 model as the best one, followed by M_2 and then M_1. Actually, a quick look at the graphical profiles would suggest that M_3 is the worst, since it is not monotonic in predicting ignition delay times. In addition, the respective problems could be "diagnosed" for the models M_1 and M_2: the first overestimates ignition delay times, but correctly reproduces the slope (i.e. the apparent activation energy of the model); the second does the opposite. This could not have been understood from the indices reported in Table 3.1.

Similar weaknesses appear after applying the same approach on the case study indicated in Figure 3.2. Here, the typical experimental mole fraction profile in an isothermal reactor is shown, and compared to the output provided by two test models. To the eye of a kinetic modeler, the better performances of M_1 are apparent, since only a 10-15 K delay in the reactivity is observed in that case (M_2 mispredicts the reactivity trend over temperature). Calculating EFV (Table 3.1) would lead to an opposite conclusion, since it is respectively equal to ~8400 and ~7400.

In principle, starting from the graphical interpretation of Figure 3.1 and 3.2, the kinetic modeler could diagnose the problem, then further refine the model, in order to get the desired trend. On the other hand, this is impractical (if not

impossible), when hundreds or thousands of charts like the one shown are to be analysed, and this is to be done in an iterative way. For this reason, an alternative, generalized approach has been devised.

3.2 Functional Data Analysis and application to curve matching

A quantitative evaluation of the ability of a kinetic model in reproducing real behaviors is not a straightforward task. Ranking more of them through a single, comprehensive index is even more difficult. In order to get this target, a mathematical methodology was conceived, based on the analysis of the data coming from both experiments and models. Such a methodology is known in literature as Functional Data Analysis (FDA) and has been applied to the described problem. A flow diagram of the overall procedure, which is illustrated in detail in the following Sections, is provided in Figure 3.3.

3.2.1 Dissimilarity measures

The core of the proposed approach is the formulation of dissimilarity measures between each model and the reference experimental data. These are discrete measurements of the quantity under investigation, and it is assumed that they are noisy point-wise evaluations of an underlying smooth process. Therefore, before computing dissimilarity indices, both experimental data and models are preprocessed through a functional estimation. Data undergo a smoothing process, and the smoothing value is obtained through the following minimization:

$$\hat{f} = \text{argmin}_{f \epsilon F} \left[\sum_{i=1}^{n} \left(y_i - f\left(x_i\right) \right)^2 + \lambda \int \left(f''\left(x\right) \right)^2 dx \right] \tag{3.4}$$

where F is the space of spline functions with a given polynomial degree (5^{th} order in this case) and a fixed number of knots, and λ is a positive smoothing parameter which weights the roughness penalty, on turn preventing the curve from being too sinuous. The effect of λ on the smoothing is effectively illustrated in Figure 3.4. Its value is obtained through a modification of the Generalized Cross-Validation (GCV) criterion [90]. In its original form, the GCV criterion obtains λ through the minimization of:

$$\lambda_{\text{opt}} = \text{argmin}_{\lambda \epsilon R^+} \frac{n \sum_{i=1}^{n} \left(y_i - f(x_i) \right)^2}{\left(n - \text{trace}\left(S\right) \right)^2} \tag{3.5}$$

where S is the smoothing matrix, mapping the data into the estimates. Therefore trace (S) is a measure of the equivalent degrees of freedom of the spline smoother.

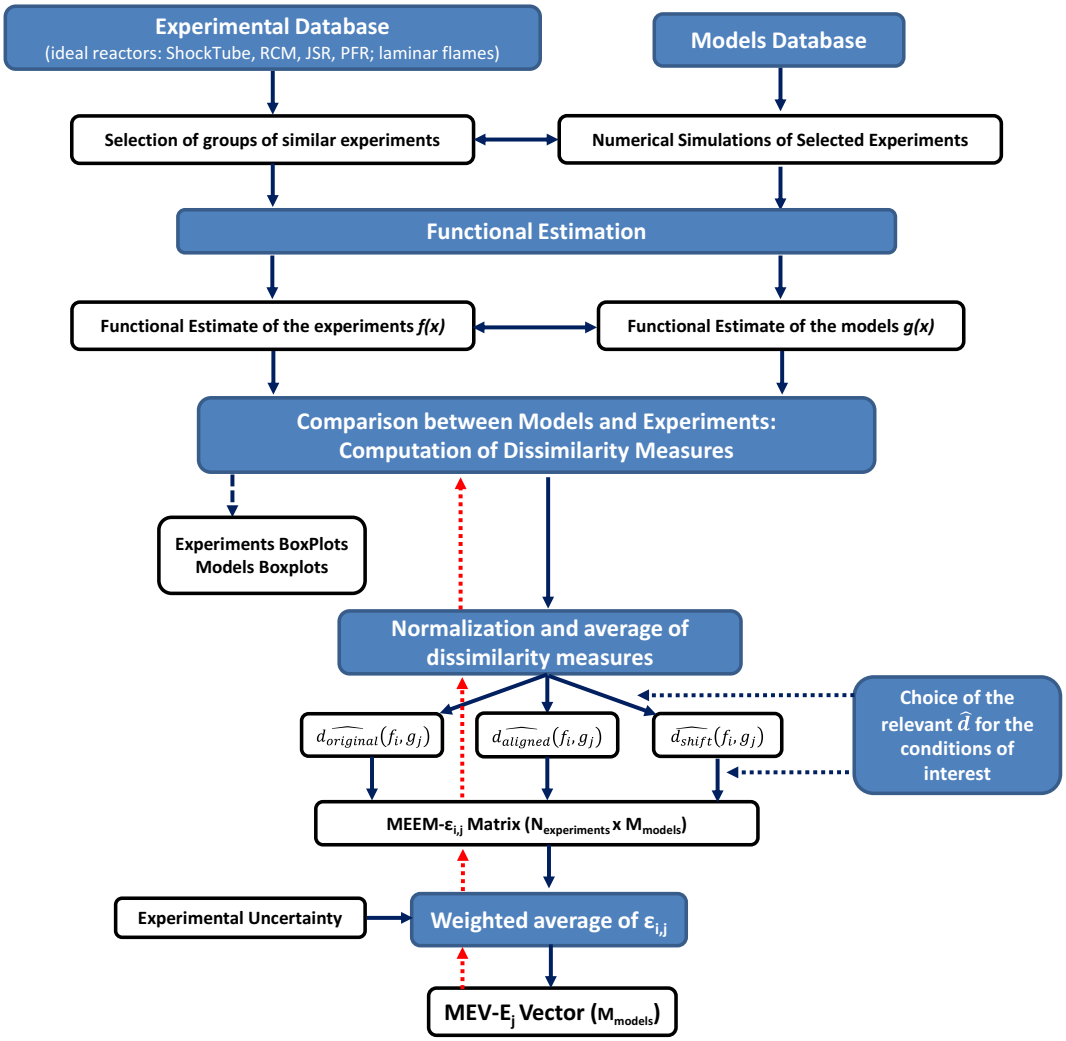

Figure 3.3: Flow diagram of the Curve Matching framework.

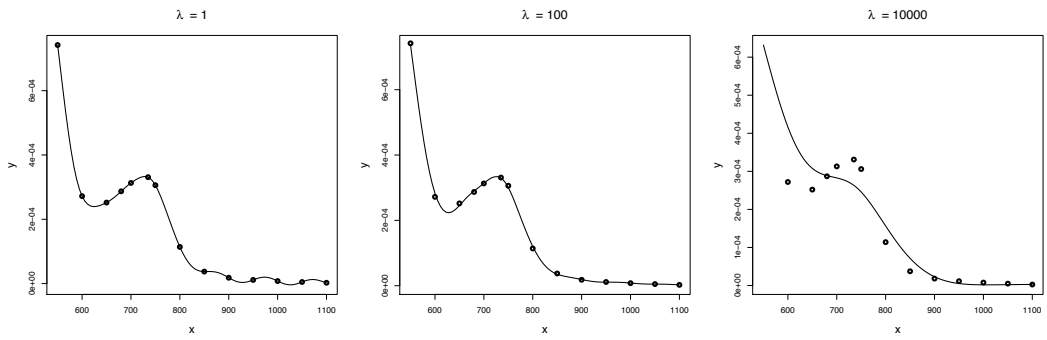

Figure 3.4: Effect of different values of λ on the smoothing function.

Since the indices developed are based on both function values and their first derivatives, GCV function is applied on first derivatives:

$$\lambda_{\text{opt}} = \text{argmin}_{\lambda \epsilon R^+} \frac{n \sum_{i=1}^{n} \left(y_i' - f'(x_i)\right)^2}{\left(n - \text{trace}\,(S)\right)^2} \tag{3.6}$$

where f' are the first derivatives of f, and y' is computed through central finite differences approximation.

In order to define the dissimilarity measures, the assumption of regularity of the involved process is made: for both experimental measurements and model predictions, the functional curves and its first derivatives must be both square integrable. The norm (3.7) and the scalar product (3.8) in the L^2-space must be computable:

$$\|f\| = \sqrt{\int_{\mathbb{R}} f\,(x)^2\, dx} \tag{3.7}$$

$$\langle f, g \rangle = \int_{\mathbb{R}} f\,(x)\, g\,(x)\, dx \tag{3.8}$$

From here on, f is defined as the reference curve, and g the model. Four dissimilarity measures are then evaluated:

$$d^0_{L^2}\,(f,g) = \tfrac{\|f-g\|}{|D|} \quad \epsilon\,(0,+\infty) \tag{3.9}$$

$$d^1_{L^2}\,(f,g) = \tfrac{\|f'-g'\|}{|D|} \quad \epsilon\,(0,+\infty) \tag{3.10}$$

$$d^0_{\text{P}}\,(f,g) = \tfrac{1}{2}\left\| \tfrac{f}{\|f\|} - \tfrac{g}{\|g\|} \right\| \quad \epsilon\,(0,1) \tag{3.11}$$

$$d^1_{\text{P}}\,(f,g) = \tfrac{1}{2}\left\| \tfrac{f'}{\|f'\|} - \tfrac{g'}{\|g'\|} \right\| \quad \epsilon\,(0,1) \tag{3.12}$$

where D is the intersection between the domains of f and g. Before computing L^2-based dissimilarities, the curves are first rescaled by dividing both models and experiments by the maximum value of the experimental curve. As concerns the Pearson dissimilarities (3.11) and (3.12), they can be reconnected to the respective Pearson similarities:

$$\rho^0_{\text{P}}\,(f,g) = \frac{\langle f, g \rangle}{\|f\|\,\|g\|} \tag{3.13}$$

$$\rho^1_{\text{P}}\,(f,g) = \frac{\langle f', g' \rangle}{\|f'\|\,\|g'\|} \tag{3.14}$$

Indeed, $\rho_{Pearson}$ measures the cosine of the angle between the two functions, and

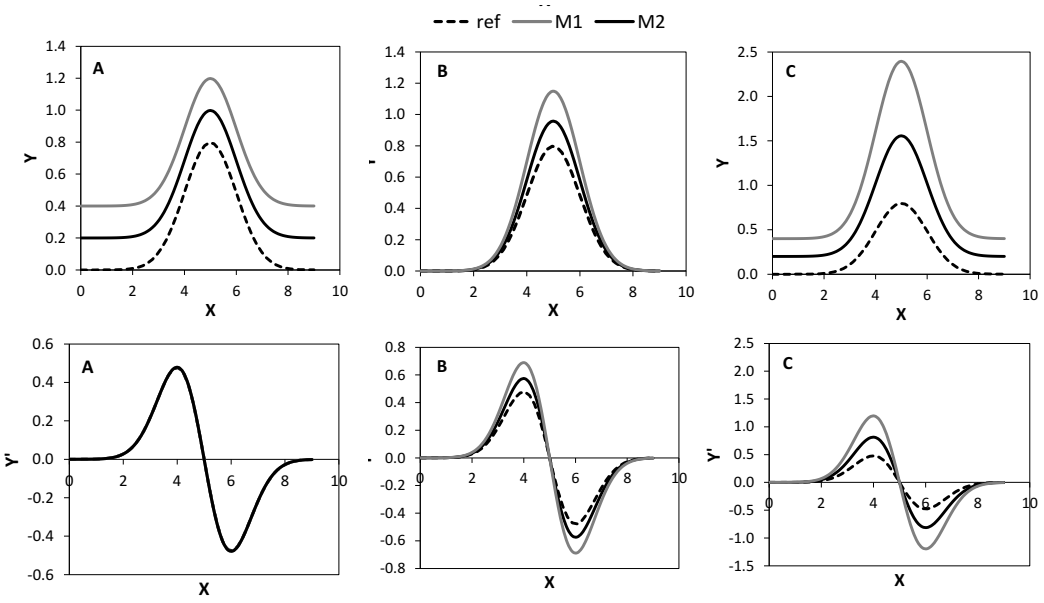

	$d^0_{L^2}$	$d^1_{L^2}$	d^0_P	d^1_P
M_1	0.067	0.000	0.050	0.000
M_2	0.133	0.000	0.113	0.000

	$d^0_{L^2}$	$d^1_{L^2}$	d^0_P	d^1_P
M_1	0.023	0.016	0.000	0.000
M_2	0.059	0.041	0.000	0.000

	$d^0_{L^2}$	$d^1_{L^2}$	d^0_P	d^1_P
M_1	0.135	0.058	0.023	0.000
M_2	0.280	0.124	0.036	0.000

Figure 3.5: Examples of (A) vertical translation, (B) vertical dilation and (C) vertical translation and dilation between curves. Dissimilarity values are reported below each panel.

are related to $d_{Pearson}$ in this way:

$$d_{\mathrm{P}} = \sqrt{\frac{1 - \rho_{\mathrm{P}}}{2}} \tag{3.15}$$

Each of the four indices owns peculiar properties, which can be summarized as follows :

- $d^0_{L^2}$ is the continuous generalization of the sum-of-squares method, thus it is reconnectable to the E index introduced by Olm et al. [86, 87].
- $d^1_{L^2}$ is insensitive to vertical translations (Figure 3.5a), i.e.:

$$d^1_{L^2}(f, f + a) = 0 \quad \forall\, a \,\epsilon\, \mathbb{R} \tag{3.16}$$

- d^0_P is insensitive to vertical dilatations (Figure 3.5b), i.e.:

$$d^0_{\mathrm{P}}(f, f * a) = 0 \quad \forall\, a \,\epsilon\, \mathbb{R} \tag{3.17}$$

- d^1_P is insensitive to both vertical translations and dilatations (Figure 3.5c), i.e.:

$$d^1_{\mathrm{P}}(f, f * a + b) = 0 \quad \forall\, a, b \,\epsilon\, \mathbb{R} \tag{3.18}$$

original	$d^0_{L^2}$	$d^1_{L^2}$	d^0_{P}	d^1_{P}	EFV
M_1	0.54	0.13	0.01	0.02	213
M_2	0.42	4.30	0.07	0.00	293
M_3	0.37	2.60	0.02	0.39	168
shift	$\delta^0_{L^2}$	$\delta^1_{L^2}$	δ^0_{P}	δ^1_{P}	
M_1	0.50	0.01	0.50	0.50	
M_2	0.16	0.00	0.50	0.04	
M_3	0.42	0.36	0.50	0.50	
aligned	$d^0_{L^2}$	$d^1_{L^2}$	d^0_{P}	d^1_{P}	
M_1	0.08	0.13	0.00	0.01	
M_2	0.33	4.30	0.02	0.00	
M_3	0.06	1.38	0.01	0.06	

Table 3.2: Index values for the example in Figure 3.1, as calculated through the proposed framework [89] and the method by Olm et al. [86, 87].

On the other hand, the horizontal differences between the two curves are taken into account by performing an alignment between the functions. For each of the four indices, the optimal shift which minimizes the value of the index itself is evaluated:

$$\delta_{\mathrm{opt}} = \mathrm{argmin}_{\delta} d\left(f\left(x+\delta\right), g\left(x\right)\right) \tag{3.19}$$

where δ is a fraction of the experimental data range, and a maximum threshold of 0.5 is set.

Overall, 12 indices are obtained: 4 before carrying out the alignment, 4 quantifying the shift, and 4 after the alignment. This initial framework can be applied to the initial example of this Chapter (Figure 3.1), and the results are shown in Table 3.2. As expectable, a parallel trend between the values of E and $d^0_{L^2}$ before alignment can be noticed. The analysis of the other indices clearly evidences the peculiar features of each model. The value of $d^1_{L^2}$ before alignment confirms the ability of M_1 in better predicting the apparent activation energy. On the other hand, the anoumalous trend of M_3 is strongly evidenced by the very high values of $d^1_{L^2}$ and d^1_P before the alignment, which remain high after the shift (especially $d^1_{L^2}$), too. Moreover, even after the alignment the value of $d^1_{L^2}$ for M_2 is still very high and this is a clear indication of the inability of the same model in predicting the slope of the curve.

Similarly, the calculation of the 12 dissimilarity measures to the case study shown in Figure 3.2 is able to identify the weaknesses shown by the two models. As shown in Table 3.3, a very small alignment of M_1 would lead to much lower dissimilarity measures. On the other hand, M_2 is almost insensitive to a horizontal

original	$d^0_{L^2}$	$d^1_{L^2}$	d^0_{P}	d^1_{P}	EFV
M_1	0.0035	0.0080	0.0442	0.1517	8400
M_2	0.0036	0.0083	0.0405	0.1676	7400
shift	$\delta^0_{L^2}$	$\delta^1_{L^2}$	δ^0_{P}	δ^1_{P}	
M_1	0.0405	0.0345	0.0365	0.0365	
M_2	0.0265	0.0225	0.0025	0.0305	
aligned	$d^0_{L^2}$	$d^1_{L^2}$	d^0_{P}	d^1_{P}	
M_1	0.0013	0.0055	0.0188	0.0928	
M_2	0.0032	0.0080	0.0404	0.1543	

Table 3.3: Index values for the example in Figure 3.2, as calculated through the proposed framework [89] and the method by Olm et al. [86, 87].

shift, due to the more significant difference in shape. After alignment, the better performance of M_1 becomes apparent.

3.2.2 Index normalization

The ultimate target of the framework relies in obtaining a univocal index, indicating the goodness of a given model in predicting experimental data. A simple summation of all the indices is indeed not applicable, since they are not measuring comparable quantities. A normalization procedure was then included in the Curve Matching framework. In its simplest form, the four indices before alignment can be considered, and a statistical analysis can be carried out on each of them. For the i-th generic experiment, the median value m and the InterQuartile Range IQR can be evaluated for each dataset and each dissimilarity measure (hereby indicated by d). Then, for each j-th of the M models, the normalized difference can be calculated between the related index and the median:

$$d_{norm} = \frac{d\left(f_i, g_j\right) - m}{IQR/2} \tag{3.20}$$

In this way, a dimensionless measure of the way each model behaves, compared to the others, is obtained. It is intuitive that a value of d_{norm} much lower than zero indicates a model behaving much better than the others, and vice versa. This normalized form makes the indices homogeneous, and can then be combined to obtain a single value. Therefore, they can be averaged in order to get an overall

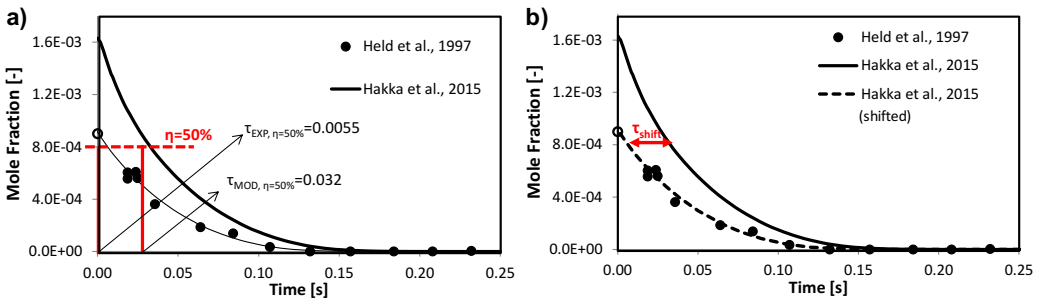

Figure 3.6: Time shift procedure for a plug flow reactor simulation. 0.163% *n*-heptane oxidation in a N_2/O_2 mixture, $\Phi = 2.27$, P = 3 atm and T = 1075 K. Experimental data by Held et al. [91]. Simulations were performed through the mechanism by Hakka et al. [92]. a) before alignment; b) after alignment. From [89].

indication of the ability of the j-th model in reproducing the i-th dataset:

$$\hat{d}\left(f_i, g_j\right) = \frac{1}{4}\left(\frac{d^0_{L^2}(f_i,g_j)-m^0_{L^2}}{IQR^0_{L^2}/2} + \frac{d^1_{L^2}(f_i,g_j)-m^1_{L^2}}{IQR^1_{L^2}/2} + \frac{d^0_P(f_i,g_j)-m^0_P}{IQR^0_P/2} + \frac{d^1_P(f_i,g_j)-m^1_P}{IQR^1_P/2}\right) \tag{3.21}$$

where $m^0_{L^2}$ and $IQR^0_{L^2}$ are calculated by analysing the index distribution of $d^0_{L^2}$ among the different models, and so on.

Example: the Plug Flow Reactor case. Averaging the four indices obtained before the alignment is the simplest way to rank different models, with respect to the others. Nevertheless, the choice of the indices to be considered in such an averaging depends on the dataset considered. As a first lumping of indices, characteristic values before the alignment $\hat{d}_{pre}\left(f_i, g_j\right)$, due to the shift $\hat{d}_{shift}\left(f_i, g_j\right)$ and after the alignment $\hat{d}_{post}\left(f_i, g_j\right)$ may be computed as in Eq. 3.21. Then, the evaluation of an overall index depends from case to case, and a proper framework needs to be created. The case of the Plug Flow Reactor (PFR) simulations is very explicative in this sense: when modeling flow reactors, possibile mixing effects are not accounted for in the 1-dimensional model [16] adopted for the simulations. For this reason, profiles are usually shifted of a time equal to that between the experimental and the calculated 50% fuel consumption (Figure 3.6).

Analysing PFR data within the Curve Matching framework makes the advantages of such a methodology apparent: curves no longer need to be shifted of an arbitrary quantity, which is only empirically justified, to be compared. In this case, a quantification of the accuracy of the model can be provided by considering the four indices obtained after carrying out the alignment introduced in Eq. 3.19. The results shown in Table 3.4 quantify the value of such indices for the sample curves of Figure 3.6. A significant decrease is observed in the values obtained

	$d^0_{L^2}$	$d^1_{L^2}$	d^0_{P}	d^1_{P}
original	0.31	0.64	0.04	0.12
shift	0.06	0.09	0.03	0.05
aligned	0.03	0.12	0.04	0.10

Table 3.4: Dissimilarity measures of the case shown in Figure 3.6 before alignment, due to shift and after alignment.

after alignment. Therefore, in this case the normalization of the index described in Eq. 3.21 should be done by considering only these four values.

3.2.3 Creation of an integrated index

Regardless of which characteristic values are selected, at the end of the procedure a Model-Experiment Error Matrix (MEEM) is obtained. Its number of rows is equal to the number of experimental data, while the columns are as many as the models under investigation. In order to obtain a ranking, the MEEM values must be converted into a vector of global indices, through a proper combination of the results obtained from each dataset. In this combination, the experimental uncertainty of the single experiments is considered, in such a way to give a higher weight to the experimental runs carried out with the higher accuracy. Indices are then combined according to 3.22, thus providing a Model Error Vector (MEV):

$$E_j = \frac{1}{\sum_{i=1}^{n} \frac{1}{\sigma_i}} \sum_{i=1}^{N} \frac{\varepsilon_{ij}}{\sigma_i} \tag{3.22}$$

As a measure of the experimental uncertainty, the standard deviation of experimental data can be used, whether available, or it can be estimated from data. Nevertheless its estimation from the differences between data and smoothing function results in unrealistically low values. Therefore, in those datasets where the standard deviation is not defined, a minimum value is fixed. The same values proposed by Olm and coworkers [86, 87] were used: 10% for ignition delay times, 2 cm/s for laminar flame speeds, and either the lowest measured concentration or 1% of the highest measured concentration for JSR, PFR or laminar flame speciations. This is a strong simplification of the problem, which has a strong impact on the obtained results. Yet, although quantification of experimental errors is an open research field [93], such information remains scarce for most experiments in combustion.

3.3 Comparison of *n*-heptane combustion mechanisms

The Curve Matching framework was successfully tested [89] for the comparison of several kinetic mechanisms describing the combustion of *n*-heptane. Such a validation demonstrated the usefulness of the approach for several purposes.

In addition to quantitatively framing a kinetic mechanism into the available literature, it proved an important instrument to compare different versions of the same mechanism. Indeed, the chemical nature of combustion phenomena is of hierarchical type, and kinetic mechanisms are usually built up accordingly [9]. Therefore, when a modification is introduced at a lower level (i.e. the smallest molecules), the chemistry of the higher levels may be affected, too. For example, when a reaction involving C_0-C_4 molecules is modified to improve the kinetic behavior of *n*-heptane, it may happen that other submodels, like NO_x or aromatics chemistry, are corrupted by such a change [94]. To this regard, the most recent example is the addition of new reaction classes describing the formation of oxygenated species in the (very) low temperature oxidation of *n*-alkanes [42, 53]. Since it involved a lower-hierarchy submechanism, the whole POLIMI mechanism needed a new performance benchmark against the available experimental data.

The application of the Curve Matching framework considered the following datasets:

i. Ignition delay times in shock tubes;

ii. Species formation in JSRs;

iii. Species formation in PFRs;

iv. Laminar flame speeds;

v. Species formation in laminar flames;

12 models were selected for comparison, and are reported in Table 3.5 . The skeletal kinetic mechanism identified as M_5 was generated from M_4 through the algorithm discussed in Chapter 4, targeted at engine-relevant conditions. The validation is summarized for the datasets i, ii and iv (laminar flame speed calculations could not be carried out for the mechanisms with a number of species higher than ~500, because of computational limitations). All the simulations were carried out through the `OpenSMOKE++` suite [16], and Table 3.6 shows the values of the integrated indices, as defined in Section 3.2.3, for the considered models. Over time, a significant improvement of POLIMI mechanisms in predicting species formation in JSR and laminar flame speed could be observed, whilst a slight worsening on

Model ID	Name	Refs
M_1	POLIMI_2008	[95]
M_2	POLIMI_2010	[95]
M_3	POLIMI_2012	[9, 95]
M_4	POLIMI_2014	[53, 95]
M_5	POLIMI_REDUCED_98	[78, 96]
M_6	LLNL_3.1	[54, 97]
M_7	LLNL_2.0	[36, 37]
M_8	LLNL_RED_159	[98]
M_9	AACHEN_OPTIMIZED	[99]
M_{10}	SANDIEGO_2015	[100]
M_{11}	COTTBUS_2015	[101]
M_{12}	HAKKA_2015	[92]

Table 3.5: *n*-heptane kinetic mechanisms compared via Curve Matching framework.

Model ID	Ignition delay times	Jet Stirred Reactors	Laminar Flame Speed
M_1	0.15	0.45	-0.13
M_2	1.34	-0.17	1.05
M_3	0.01	0.25	-0.06
M_4	0.43	-0.56	-0.6
M_5	0.66	-0.36	-0.05
M_6	-1.08	-1.1	-
M_7	0.02	-0.82	-
M_8	-0.17	2.02	2.64
M_9	-0.93	0.34	-0.38
M_{10}	1.38	4.63	-
M_{11}	0.30	0.57	-
M_{12}	2.43	-1.16	0.2

Table 3.6: Value of MEV of the models for 3 different group of models. They account for the three dimensionless indices $\hat{d}_{pre}$, $\hat{d}_{shift}$ and $\hat{d}_{post}$. Negative ($\hat{d}_{ij} > 2$) and positive ($\hat{d}_{ij} < 2$) outliers are colored in red and green, respectively.

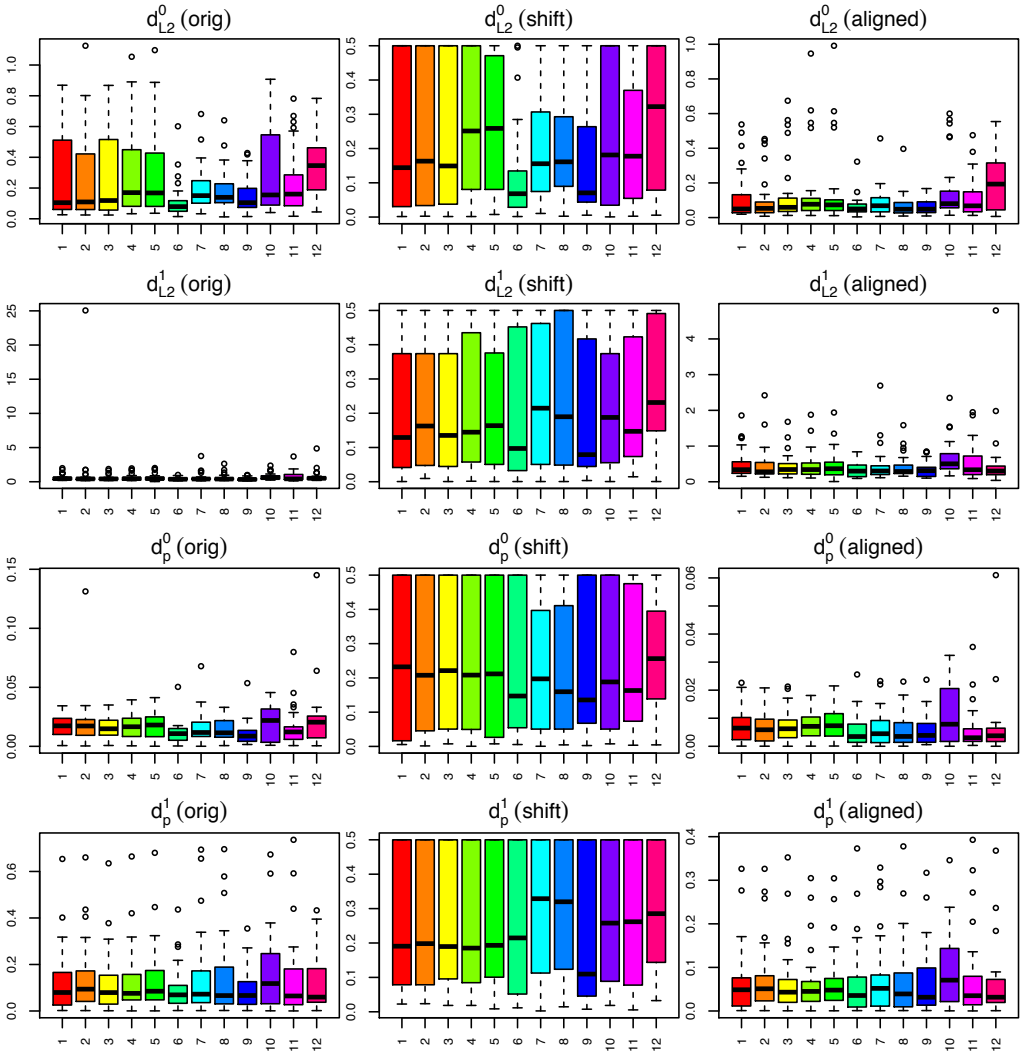

Figure 3.7: Box plots of the investigated models for the dataset i.

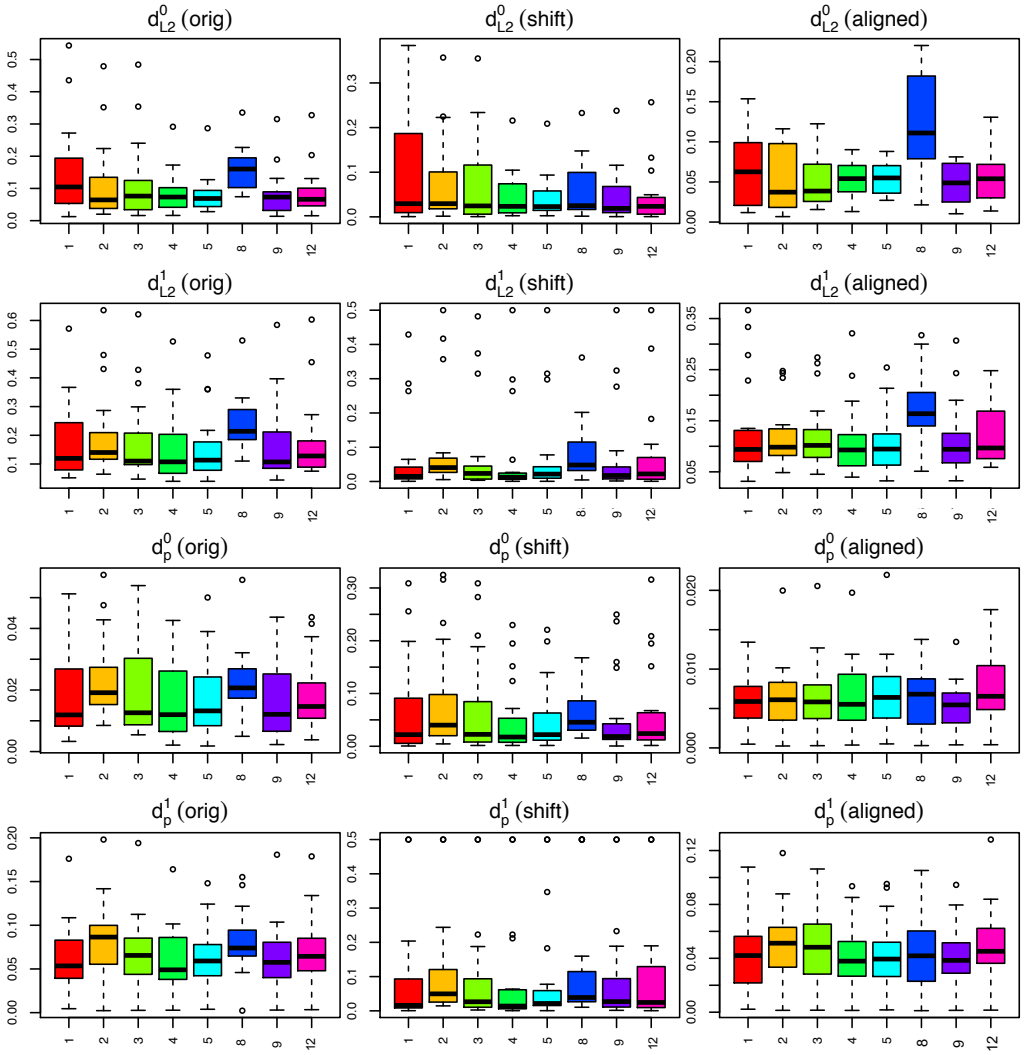

Figure 3.8: Box plots of the selected models for the dataset iv.

	...	49	50	51	52	...	61	62	63	64	65	...
M_1	...	0.70	0.16	-0.61	0.37	...	-0.19	-0.45	-1.37	-0.35	-0.07	...
M_2	...	0.23	-0.09	-0.56	1.32	...	-0.85	-0.42	-0.20	-0.16	-0.47	...
M_3	...	0.55	-0.37	-1.15	1.18	...	-0.46	-0.71	-0.33	-0.89	-0.38	...
M_4	...	-0.02	0.13	0.94	1.60	...	-0.47	-0.42	-0.35	-0.20	0.16	...
M_5	...	0.02	0.57	1.41	1.53	...	-0.47	0.06	-0.38	0.37	0.37	...
M_6	...	-1.52	-1.46	-2.60	-1.04	...	-1.96	-1.35	0.84	-3.15	-0.70	...
M_7	...	-0.55	0.88	0.49	-0.44	...	0.11	0.59	1.53	0.67	1.19	...
M_8	...	-1.12	0.84	0.33	-1.06	...	0.26	1.00	-0.87	0.87	0.90	...
M_9	...	-1.39	-1.88	-1.73	-0.79	...	-2.49	-0.33	2.93	-1.99	-0.54	...
M_{10}	...	0.59	2.89	2.17	0.15	...	2.18	6.67	-1.16	5.50	3.23	...
M_{11}	...	-0.46	-3.70	-0.51	-1.42	...	0.15	1.41	1.18	-1.69	-2.91	...
M_{12}	...	-0.80	1.37	6.63	-0.48	...	2.79	2.18	0.41	5.22	6.22	...

Table 3.7: Portion of MEEM values for the group 1 datasets. Negative ($\hat{d}_{ij} > 2$) and positive ($\hat{d}_{ij} < 2$) outliers are colored in red and green, respectively. Full matrix is available in [89].

ignition delay times can be noticed. Anyway, for all of them the dissimilarity indices distribution is comparable, as shown by the box plots in Figure 3.7. Overall, the LLNL_3.1 mechanism (M_6) showed the best performances for the first two classes, but it could not be used for laminar flame speed evaluations because of the excessive dimensions. On the other hand, LLNL reduced mechanism (M_8), which had been obtained from model M_7, proved the worst in predicting laminar flame speed (note: its development had not been targeted at flame speed predictions, but rather on autoignition properties, as reported by the authors). In the following, details are added on subsets 1 and 4, since they provide case studies for the two major applications of Curve Matching framework, i.e. model improvement and critical experimental conditions.

3.3.1 Ignition delay times in Shock Tubes

The first MEV reported in Table 3.6 shows one negative outlier, i.e. M_{12}. A deeper analysis of the related MEEM, partially reported in Table 3.7, indeed highlights that such model has a bad behavior in simulating several datasets. As an illustrative example, case 65 can be considered ($\varepsilon_{65,M12} = 6.22$). It represents ignition delay time measurements for the *n*-heptane/air stoichiometric mixtures at 12 atm, taken by Shen et al. [102]. For the sake of clarity, only M_9, M_{10}, M_{11} and M_{12} are analysed in this context, thus only the related curves are shown in Figure 3.9. As shown in Table 3.8, if only $d^0_{L^2}$ is considered (i.e. the "continuous"

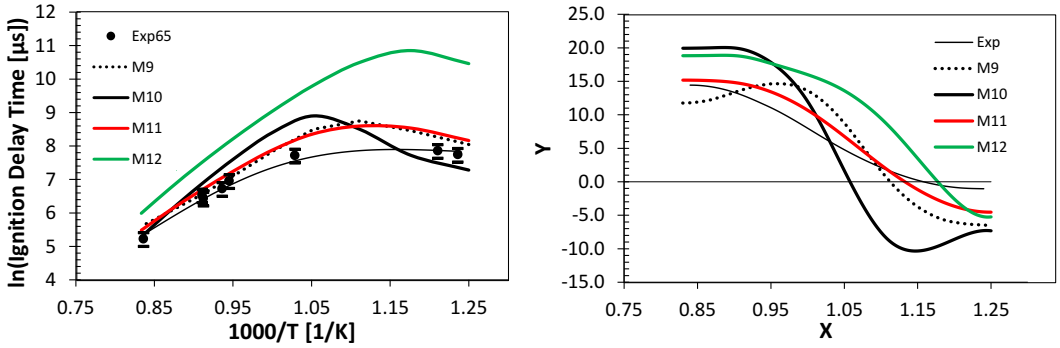

Figure 3.9: Left: Experimental ignition delay times as measured by Shen et al. [102] (Case 65) in a functional representation, and predictions from mechanisms M9, M10, M11, M12. 20% error bars are reported. Note: ignition delay time is in logarithmic units. Right: First derivatives of the related functional values.

original	$d^0_{L^2}$	$d^1_{L^2}$	d^0_P	d^1_P
M_9	0.113	0.418	0.013	0.181
M_{10}	0.139	0.788	0.031	0.247
M_{11}	0.107	0.225	0.007	0.080
M_{12}	0.426	0.673	0.029	0.142
shift	$\delta^0_{L^2}$	$\delta^1_{L^2}$	δ^0_P	δ^1_P
M_9	0.055	0.045	0.040	0.043
M_{10}	0.093	0.018	0.064	0.198
M_{11}	0.075	0.048	0.028	0.006
M_{12}	**0.500**	0.236	0.164	0.144
aligned	$d^0_{L^2,align}$	$d^1_{L^2,align}$	$d^0_{P,align}$	$d^1_{P,align}$
M_9	0.105	0.406	0.011	0.180
M_{10}	0.118	0.787	0.027	0.182
M_{11}	0.094	0.204	0.005	0.079
M_{12}	0.282	0.398	0.004	0.086

Table 3.8: Dissimilarity values for the experimental dataset 65 shown in Figure 3.9.

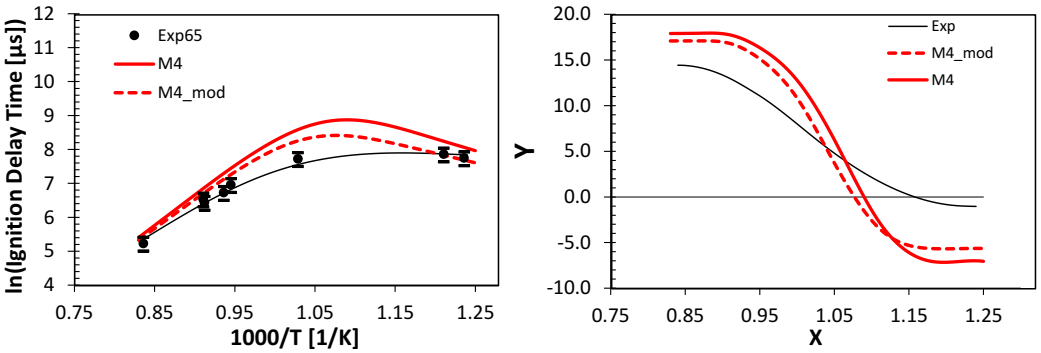

Figure 3.10: Left: Experimental ignition delay times as measured by Shen et al. [102] (Case 65) and predictions from M_4 and M_4-modified mechanisms .Right: First derivatives of the same functional values.

	$d^0_{L^2}$	$d^1_{L^2}$	d^0_P	d^1_P
M_4	0.149	0.529	0.016	0.161
$M_{4,\text{mod}}$	0.088	0.437	0.016	0.160

Table 3.9: Original dissimilarity values for the experimental dataset 65 shown in Figure 3.9, for the original M_4 [53] and its modified version $M_{4,\text{mod}}$.

version of the sum of squared errors), M_9, M_{10} and M_{11} are comparable, while M_{12} is significantly different. On the other hand, larger deviations are observed for first derivatives. Although the ignition delay times are reproduced quite well, in the case of M_{10} the transition from the high to the intermediate temperature regime (relative maximum in ignition delay time) is anticipated of about ~70 K. As a result, both $d^1_{L^2}$ and d^1_P are significantly higher. Since Pearson indices refer to the shape of the curve, the high values computed for M_{10} and M_{12} are easily explained. Moreover, it can be noticed that after the alignment the error trend does not significantly change.

Curve Matching for model improvement. The example just shown can be leveraged for the improvement of the current version of the kinetic mechanism. Figure 3.10 shows the performance of the recently revised POLIMI mechanism [53]. In order to understand the model behavior a sensitivity analysis is carried out at 900 K and 12 atm. Figure 3.11 shows that the rate constant of heptyl radical and hydroperoxy-heptyl radical addition to O_2, and the H-abstraction by HO_2 increases reactivity (i.e. decrease ignition delay times). To assess the impact of reaction rates modification on the dissimilarity values of M_4, the rate constant were multiplied by 1.2 in the test model $M_{4,\text{mod}}$, also shown in Figure 3.10. Table 3.9 shows that a consistent reduction of both L^2 indices is observed, while Pearson

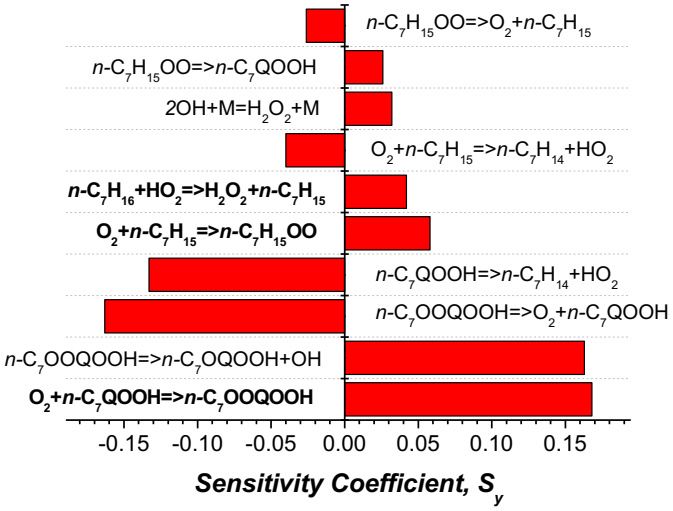

Figure 3.11: Sensitivity of Ignition Delay Times to rate constants in M4 [53]. n-heptane/air, Φ=1.0, T=900 K, p=12 atm.

	...	22	23	24	25	26	27	...
M_1	...	0.50	1.26	0.32	0.26	-0.09	1.10	...
M_2	...	1.53	0.66	-1.00	-1.36	0.24	0.13	...
M_3	...	1.27	0.69	-2.28	-0.20	-0.29	-0.76	...
M_4	...	-1.09	-0.93	0.09	0.54	0.25	-0.27	...
M_5	...	-1.84	-1.36	0.09	1.23	1.47	0.73	...
M_8	...	-1.30	0.68	6.77	2.65	2.93	5.17	...
M_9	...	0.01	-0.54	-0.91	-0.67	-1.75	-1.17	...
$M1_2$	...	0.40	-0.24	2.14	-1.38	-1.09	0.75	...

Table 3.10: Portion of MEEM values for the group 4 datasets. Negative ($\hat{d}_{ij} > 2$) and positive ($\hat{d}_{ij} < 2$) outliers are colored in red and green, respectively. Full matrix is available in [89].

indices are not sensitive to such modifications. The actual improvements are also visible in both graphs, where it can also be observed that the shape of the two curves does not significantly change.

3.3.2 Laminar flame speeds

In this case, too, Table 3.6 (third column) shows one negative outlier, i.e. M_8. As a matter of fact, systematic deviations are present in several simulations, as shown in the related MEEM (Table 3.10). Here, the dataset 24 is considered, and, again, a limited set of models is shown in Figure 3.12 for the sake of clarity. In this specific case, it can be noticed that M_8 and M_{12} are two negative outliers, while M_3 is a positive one. Indeed, both graphically and quantitatively (Table 3.11),

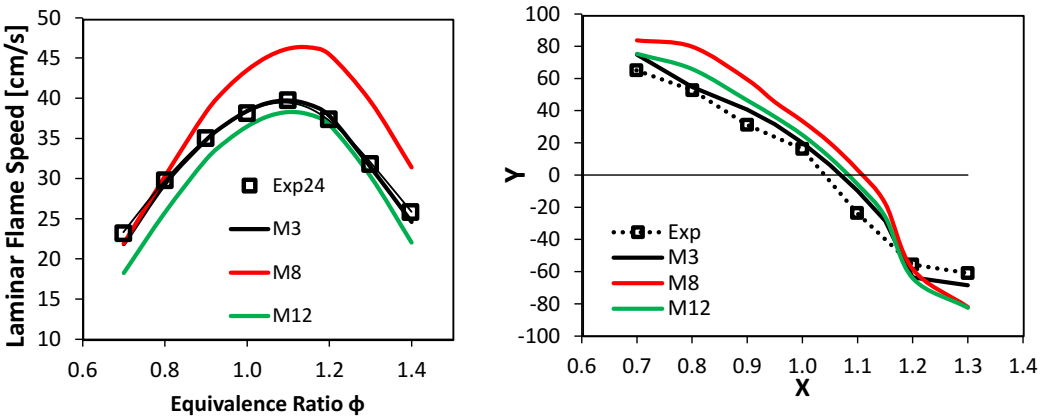

Figure 3.12: Left: experimental laminar flame speed of n-heptane/air mixtures as measured by Huang et al. [103] and predictions from different kinetic mechanisms (M_3, M_8, M_{12}). T=298 K, P=1 atm. Right: First derivatives of the related functional values. Experimental error (~2% [103]) is kept into account through the size of symbols.

original	$d^0_{L^2}$	$d^1_{L^2}$	d^0_P	d^1_P
M_3	0.016	0.099	0.008	0.014
M_8	0.170	0.300	0.032	0.089
M_{12}	0.077	0.179	0.022	0.035
shift	$\delta^0_{L^2}$	$\delta^1_{L^2}$	δ^0_P	δ^1_P
M_3	0.004	0.004	0.004	0.003
M_8	0.027	0.059	0.062	0.056
M_{12}	0.028	0.018	0.026	0.018
aligned	$d^0_{L^2,align}$	$d^1_{L^2,align}$	$d^0_{P,align}$	$d^1_{P,align}$
M_3	0.016	0.099	0.007	0.014
M_8	0.167	0.241	0.007	0.019
M_{12}	0.072	0.171	0.018	0.022

Table 3.11: Dissimilarity values for the experimental dataset 24 shown in Figure 3.12.

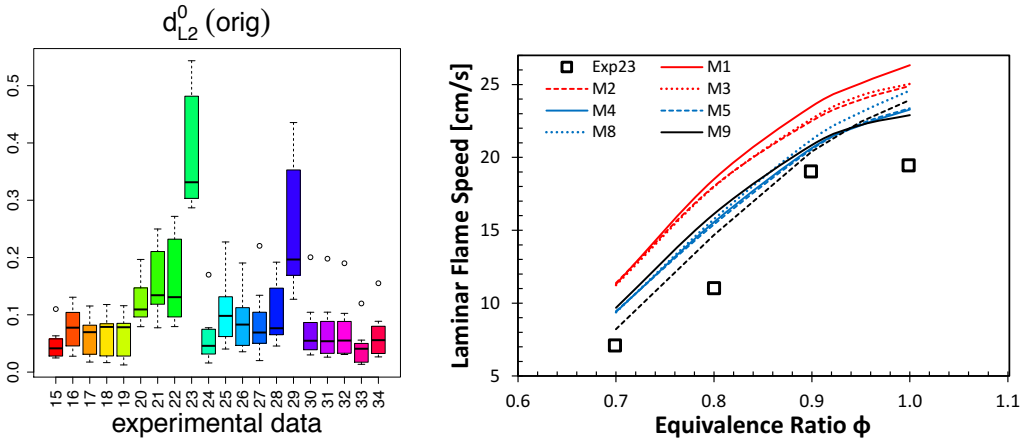

Figure 3.13: Left: Detail of the $d^0_{L^2}$ boxplot for the group of experiments "Laminar Flame Speed". Right: Case 23 - Comparison between experimental laminar flame speed of n-heptane/air mixtures as measured by Jerzembeck et al. [104] and predictions from different kinetic mechanisms. T= 373 K, P=25 bar. Experimental error is 2-2.5 cm/s.

M_3 shows an excellent agreement with experimental data and their derivatives in a functional form. On the other hand, M_8 and M_{12} show deviations in opposite directions, much more apparent in terms of $d^0_{L^2}$. Less significant differences can be observed for Pearson values, since the shape of the curves is comparable in the three cases. Finally, also in this case a negligible impact of the horizontal shift can be noticed, and the four curves remain substantially unchanged after alignment, too.

Curve Matching for detecting critical experimental conditions. Grouping error indices by experiment and viewing in the form of a boxplot turns out as very useful to understand systematic deviations from experimental data. As an example, the $d^0_{L^2}$ values of a subset of the Laminar Flame Speed database are shown in Figure 3.13 (left). While the error distribution is more or less homogeneous for all the experiments, two outliers are present, i.e. cases 23 and 29. Considering case 23, Figure 3.13 (right) shows that every mechanism poorly predicts the experimental measurements, with extreme deviations of about ~7 cm/s for M_1, M_2 and M_3. More important, all mechanisms systematically overestimate the experimental behavior. This indicates that a further investigation on the specific case is required, in order to understand the source of the error. In principle, the reasons behind such anomalies may be either related to a systematic lack of knowledge of all the models, or to an issue with experimental data, which failed in accuracy in a given dataset for some reason (bad instruments calibration, pollution of the reactants, and so on). Important indications for experimentalists, too, might then come out from such an analysis.

3.4 Conclusions

The strong nonlinearity affecting chemical kinetic models makes their analysis a very challenging task: so far, most current approaches are completely qualitative and cannot be considered comprehensive at all. From this point of view, the application of FDA to chemical kinetic analysis is a completely unexplored territory, with a lot of potential though. As a matter of fact, a twofold task can be accomplished:

i. Investigate the capability of kinetic models, in reproducing experimental trends;

ii. Compare different models.

The creation of dissimilarity indices, and their proper framing into the Curve Matching methodology, were able to fulfill both of them. Such a framework is now a very helpful instrument in the hands of the kinetic modeler, who can use it for validating, updating and troubleshooting his/her own mechanism. Indeed, the case studies shown in Sections 3.3.1 and 3.3.2 pointed out that the output provided by the framework can be leveraged in two opposite directions:

i. Highlighting model weaknesses and improving their performance, with the help of chemical kinetic tools like Rate of Production Analysis or Sensitivity Analysis;

ii. Finding out possible anomalies in the experimental datasets, and then guide the design of further experimental investigation.

The applications of such a methodology are manifold, and not limited to the field of combustion model validation, as one may easily imagine. Within the context of this Thesis, it will turn out as an important tool for the development of a species-targeted skeletal reduction approach, able to keep the desired degree of accuracy on fixed chemical species through an error-controlled procedure. In this way, compact and reliable kinetic models describing the chemistry of species with longer time scales (e.g. NO_x, Polycyclic Aromatic Hydrocarbons - PAH, soot) can be created in an automatic way starting from a detailed, and well-verified, model. Such a topic is considered in detail in Chapter 4, where it is integrated to the most general framework for systematic mechanism reduction.

CHAPTER 4

A multi-step approach to mechanism reduction

CHAPTER 2 showed that the combined use of lumping and flux-based skeletal reduction techniques can significantly decrease the size of kinetic mechanisms. Nevertheless, especially when transportation fuels are involved, even such a coupling is often insufficient to obtain mechanisms applicable to multidimensional applications. A further refinement in the analysis of important species and reactions is thus necessary, although it may require a significantly higher computational effort. The problem to be addressed is then twofold: conceptual and numerical, because the generation of a skeletal mechanism must be also provided in reasonable computational times.

As pointed out by Xin et al. [105], when a detailed mechanism is reduced, the species composing the original mechanism may be divided into three categories: critical, marginal and nonessential. After defining the $T - P - \Phi$ space of operating conditions, an optimal reduction methodology must be able to remove nonessential species quite straighforwardly, and to make the best possible selection of the marginal ones, according to the fixed level of accuracy. Expectably, there is an opposite trend between the effectiveness of a reduction technique and its computational demand. Therefore, a multi-step approach becomes convenient in this context, by applying the faster (and rougher) approaches on the original

mechanism, and computationally heavier (but more accurate) ones on already reduced models. More accurate approaches are usually based on sensitivity analysis [19, 84], by which the importance of each species in the accuracy of a given target is estimated. Nevertheless, in most cases they have been focused on keeping the overall reactivity, e.g. in terms of ignition delay time or laminar flame speed properties. Therefore, so far no work on mechanism reduction has been carried out on species not directly related to the reactivity behavior, like NO_x, PAH or soot.

The need of generalizing the reduction procedure to create *ad hoc* skeletal mechanisms is then apparent. In this Chapter, the development of a multi-step methodology and its implementation into a numerical tool are described. Its starting point relies on the combination of flux analysis and sensitivity analysis on species, as already done in literature. Flux analysis is introduced in Section 4.1, where the approach proposed by Pepiot-Desjardins and Pitsch [76] is illustrated. An improved sensitivity analysis on species is then described in Sections 4.2, and an extension to reactions is proposed in Section 4.3. In the second part (Section 4.6 onwards) sensitivity analysis is extended through the Curve Matching framework, discussed in Chapter 3, which is applied here to obtain skeletal mechanisms with the desired level of accuracy on specific species. Applications in Sections 4.5 and 4.7 show sample skeletal mechanisms development through the obtained framework.

4.1 Directed Relation Graph with Error Propagation

The main concepts of the DRGEP approach, devised by Pepiot-Desjardins and Pitsch [76], are recalled and framed into the complete procedure. Like DRG, DRGEP transforms the original kinetic mechanism into an equivalent graph, whose species constitute the vertices, on turn connected by reactions (edges). In a given reaction state, the importance of species B in forming species A is estimated through the related Direct Interaction Coefficient (DIC):

$$r_{AB} = \frac{\left| \sum_{j=1}^{NR} \nu_{A,j} \dot{\omega}_j \delta_j^B \right|}{\max\left(P_A, C_A\right)} \tag{4.1}$$

where P_A and C_A are defined as in Eqs. (2.4) and (2.5), δ_i^B is a boolean variable, representing the presence of B in the j-th reaction, $\nu_{A,j}$ is the stoichiometric coefficient of species A in the j-th reaction, and $\dot{\omega}_j$ is the net reaction rate of the j-th reaction. Once one or more target species are set up, a path-dependent interaction

coefficient is calculated via a damping procedure:

$$r_{AB,p} = \prod_{i=1}^{n_p-1} r_{S_i S_{i+1}} \tag{4.2}$$

where S is the generic intermediate species, interposing in the p-th reaction path between the target species A and B. The importance of species B in the prediction of A is then calculated through the Overall Interaction Coefficient (OIC):

$$R_{AB} = \max_{\text{all paths p}} (r_{AB,p}) \tag{4.3}$$

Several algorithms can be adopted to find the path with the maximum product of DICs: in their work, Niemeyer and Sung [106] showed that Dijkstra's shortest path algorithm [107] is the most performing for this type of problems, as well as independent on the order of the species in the kinetic mechanism. When reaction states are sampled in dynamic reactors, these coefficients can be corrected according to the scaling procedure proposed by Pepiot-Desjardins and Pitsch [76]. A time-dependent scaling factor is introduced to quantify the contribution of the target species X to the instantaneaous system reactivity. To this purpose, the time-dependent production and consumption rates of the generic atom a are calculated as:

$$P_a = \sum_{i=1}^{N_S} N_{a,i} \max(0, P_S - C_S) \tag{4.4}$$

$$C_a = \sum_{i=1}^{N_S} N_{a,i} \max(0, C_S - P_S) \tag{4.5}$$

where P_S and C_S are defined as in Eq. 2.4 and 2.5, and $N_{a,i}$ is the number of atoms a of the i-th species. For the X target, a scaling factor related to the atom a can be then defined as:

$$\alpha_{a,X}(t) = \frac{N_{a,X} |P_X - C_X|}{P_a} \tag{4.6}$$

For each time t, the maximum scaling factor among all atoms is chosen, normalized with respect to the maximum scaling factor throughout the whole integration:

$$\alpha_X(t) = \max_{\text{all atoms}} \frac{\alpha_{a,X}(t)}{\max_t \alpha_{a,X}(t)} \tag{4.7}$$

Therefore, the coefficient representing the importance of species B is evaluated by analyzing all target species and all the time steps, i.e.:

$$\widetilde{R}_B = \max_{X,t} \left(\alpha_X \left(t \right) R_{XB} \left(t \right) \right) \tag{4.8}$$

Reaction states are sampled by setting up ideal reactors (batch or perfectly stirred [19,75,108]) in the $\mathrm{T} - \mathrm{P} - \Phi$ space. In this framework, the focus is set on autoignition phenomena in adiabatic batch reactors, chosen at constant pressure or volume according to the application which they are intended to (e.g. atmospheric flame or internal combustion engine). For each reactor, a local threshold is set up (around 10^{-3}) and fuel and oxidizer are considered as target species. The species with an $\widetilde{R}_i$ higher than the threshold are kept, and a reduced mechanism is created for each sampled point of the $\mathrm{T} - \mathrm{P} - \Phi$ space. Reduction continues then independently for each mechanism through the sensitivity analysis described in Section 4.2.

4.2 Sensitivity analysis to ignition delay time

Like all flux-based approaches, DRGEP is very quick in determining species ranking, and the overall computing time is not much longer than the time required for the resolution of the ideal reactors. Nevertheless, the importance ranking provided by a flux analysis is always to be considered as approximate. Niemeyer et al. [19] showed that the correlation between species OIC and the error induced from their removal is not linear at all, and by increasing the threshold the risk of losing critical species increases. A more refined reduction can then only be achieved by using more time consuming approaches, which quantify the actual effect of the removal of a species from the original mechanism. Such a methodology, known as sensitivity analysis, was implemented in approaches like DRGASA and DRGEPSA as already mentioned in Chapter 2. In those frameworks, the investigated property was ignition delay time (IDT), considered as representative of the overall system reactivity. Such a methodology was integrated in the developed multi-step procedure for each local mechanism obtained from flux analysis. Not all the species undergo sensitivity analysis to IDT, though. Indeed, a relatively low error in predicting IDT following the removal of a given species does not imply the same degree of accuracy in other cases, like laminar flame speed. To prevent this to happen, a smaller subset of species is analysed. They are detected through a double criterion:

- Following Zheng et al. [84], the i-th species is excluded from sensitivity anal-

ysis if its $\widetilde{R}_i$ value (4.8) is higher than a defined threshold (usually 0.1 – 0.4).

- Similarly, the i-th species is excluded if its normalized overall flux value is higher than a defined threshold (usually 0.05 - 0.10). This is defined as:

$$F_i = \frac{MW_i \cdot \int_0^{t_{ign}} (P_i + C_i)\, dt}{\max\limits_{\text{all species S}} \left(MW_S \cdot \int_0^{t_{ign}} (P_S + C_S)\, dt \right)} \tag{4.9}$$

  where t_{ign} is the reactor ignition delay time, and P_i and C_i are defined as in Eqs. (2.4) and (2.5). This allows to further reduce the size of the marginal species subsets, without significant effects on the size of the final mechanism.

The selected species are locally ranked according to the error on ignition delay following their removal: for the i-th species, it is calculated as:

$$\varepsilon_{i,L} = \frac{|\tau_{ign,i} - \tau_{DRGEP,i}|}{\tau_{DRGEP,i}} \tag{4.10}$$

where $\tau_{DRGEP,i}$ and $\tau_{ign,i}$ are the ignition delay times before and after the removal, evaluated as the time where the maximum temperature gradient occurs.

Once ranked, species can be progressively removed from the mechanisms obtained in 4.1. Adopting a local procedure allows to solve the same problem with a locally lower number of involved variables. Indeed, the local mechanisms where sensitivity analysis is carried out are smaller than the one obtained by merging species subsets, as done in traditional DRGASA and DRGEPSA. The local strategy can be further refined: since the couplings among species cause a strong nonlinearity within the kinetic mechanism, species ranking cannot be considered as invariant throughout the reduction procedure. A restart factor ρ is then introduced, and the species ranking is updated once σ_k/ρ species have been removed, with σ_k being the current size of the local marginal subset for the k-th reactor. The value of ρ is arbitrary, and depends on both mechanism size and computational availability. Anyway, a convergence of results was observed for $\rho > 5 - 10$. A similar observation was also recently made by Niemeyer and Sung [108], who improved the original DRGEPSA by recalculating the global ranking after each species removal.

For each mechanism, this procedure is carried on until the error on IDT reaches a defined threshold in each point. Local subsets are then merged and a first, comprehensive mechanism is created. Merging subsets results in the addition of more species to each investigated point. This obviously changes the performance

of the final mechanism in the single point, and most often decreases the local error because of the higher number of added variables. The DRGASA approach of Zheng et al. [84] can be then applied in the whole $\mathrm{T}-\mathrm{P}-\Phi$ domain, after selecting the uncertain species through the two already mentioned criteria. In this case, the removal ranking is generated by calculating the maximum error on IDT in the whole domain:

$$\varepsilon_{i,G} = \max_{\mathrm{T-P-\Phi}} \frac{|\tau_{ign,i} - \tau_{DRGEP,i}|}{\tau_{DRGEP,i}} \tag{4.11}$$

Species can then be progressively removed, and such a ranking is updated every n iterations. Like for ρ, the value of n depends on the size of the original algorithm and computational availability. Niemeyer and Sung [108] used a value of n equal to 1 for the generation of a gasoline surrogate. Although this is the most rigorous way of ranking generation, it may result in impractical computational times when applied to large mechanisms, like heavy n-alkanes [45] or fuel surrogates [54].

4.3 Sensitivity analysis on reactions

Regardless of the investigated variables, sensitivity analysis has always been a fundamental tool to identify the governing parameters in numerical models. In numerical combustion, it has been used in several ways [68, 109–112]. Currently, thanks to the higher computational availabilities, such analyses can be carried out also in systems with a large number of involved parameters. This is the case of detailed kinetic mechanisms, whose number of involved reactions can be of the order of thousands or more. In this case, the concerned parameters are the reaction rates, and sensitivity analysis can be carried out either on pre-exponential factor or activation energy. Here, first-order sensitivity coefficients of pre-exponential factors are considered. Their equations can be derived from the Ordinary Differential Equation (ODE) system representing the (dynamic) ideal reactor:

$$\begin{cases} \frac{d\mathbf{y}}{d\xi} = f\left(\mathbf{y}, \xi, \boldsymbol{\alpha}\right) \\ \boldsymbol{y}\left(\xi_0\right) = \boldsymbol{y_0} \end{cases} \tag{4.12}$$

where $\mathbf{y}$ is the variables vector (mass fractions + temperature), ξ the reaction coordinate and $\boldsymbol{\alpha}$ the vector of parameters (i.e. pre-exponential factor of kinetic constants), whose value set and control the whole system evolution. In the case of unsteady reactors, like those analysed here, the sensitivity coefficients of the

i-th variable with respect to the j-th parameter are then defined as:

$$s_{ij}(\xi) = \frac{\partial y_i(\xi)}{\partial \alpha_j} \tag{4.13}$$

and in their normalized form:

$$\tilde{s}_{ij} = \frac{\partial \ln y_i}{\partial \ln \alpha_j} = \frac{\partial y_i}{\partial \alpha_j} \cdot \frac{\alpha_j}{y_i} \tag{4.14}$$

For each time step, the number of sensitivity coefficients to be evaluated is equal to the product of the number of variables N_E by the number of parameters (i.e. reactions) N_P. Therefore, it may easily become huge for a detailed mechanism. By differentiating the system with respect to the parameters α_{ij}, an ODE system is obtained for each j-th vector of parameters:

$$\begin{cases} \frac{d\boldsymbol{s_j}}{d\xi} = \boldsymbol{J}\boldsymbol{s_j} + \frac{\partial \boldsymbol{f}}{\partial \alpha_j} & j = 1 \dots N_P \\ \boldsymbol{s_j}(\xi_0) = 0 \end{cases} \tag{4.15}$$

where $\boldsymbol{J}$ is the ODE system (4.12) Jacobian matrix, $\mathrm{J_{ij}} = \frac{\partial \mathrm{f_i}}{\partial \mathrm{y_j}}$, and $\mathbf{s_j}$ has the size of $\mathbf{y}$ (number of variables). These equations are added to the ODE system (4.12) and are dependent on them (but the opposite is not true). Therefore, such a system can be extremely demanding and directly solvable only for a small number of variables. Nevertheless, Cuoci et al. [16] showed that proper simplifying assumptions can make the problem affordable. Indeed, since the second, right-hand-side term in Eq. 4.15 does not depend on sensitivity coefficients, the Jacobian matrix associated to the whole system is very sparse and block-structured. Therefore, instead of solving the system as a whole, the ODE systems defined in Eq. 4.15 can be solved independently. In addition, the independence of ODE system from sensitivity equations allows to solve them serially in a decoupled way. Actually, this can be done only if it is assumed that the ODE system (4.12) dictates the integration step. Yet, in small systems where a fully coupled approach was computationally feasible, a maximum error of about 5% in their value was experienced, which is more than acceptable for the purposes of this application.

In order to decouple the importance of pressure-dependent reactions from pressure behavior, this step is always carried out in isobaric reactors. After the reactor is solved and sensitivity coefficients are gathered throughout the whole reactor length, they are post-processed to understand their relative importance in the kinetic mechanism in the considered conditions. If preserving the overall reactivity is the target of reduction, fuel and oxidizer are chosen as target species, or

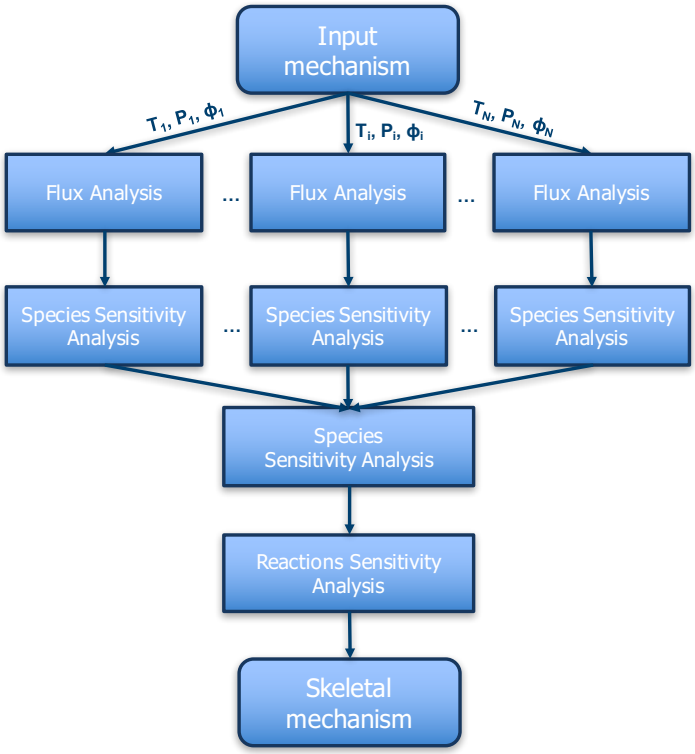

Figure 4.1: Flux diagram of the multi-step reduction procedure described in this Chapter.

if a particular species is of interest the related coefficients can be investigated. A characteristic coefficient of the j-th reaction with respect to the i-th species is evaluated as the maximum value of the absolute sensitivity profile over the reaction coordinate:

$$\hat{s}_{ij} = \max_{t \,\epsilon\, [0,\tau]} \tilde{s}_{ij}\,(\xi) \tag{4.16}$$

where τ is the reactor residence time. Once the coefficients are evaluated, the j-th reaction may be discarded if, for all the reactors, $\hat{s}_{ij}$ is lower than a defined threshold for all the selected species. It was observed that 10^{-3} can be considered as a conservative reference threshold to keep accuracy on system reactivity. Finally, if all the reactions involving a given species are classified as unimportant, the same species can be removed.

4.4 Algorithm implementation

An overview of the overall methodology is described in Figure 4.1, in the form of a flux diagram. Its constituting steps can be summarized as follows:

i. According to the selected points in the $\mathrm{T} - \mathrm{P} - \Phi$ space, ideal reactors are set up considering all the possible combinations of the provided points. On each

of them, flux analysis (Section 4.1) is carried out, and species are ranked accordingly. Species with a maximum DRGEP coefficient lower than the defined threshold are excluded, and a mechanism is created for each reactor.

ii. Sensitivity analysis is locally carried out on each mechanism obtained at the previous step, following Section 4.2. When the error threshold is reached, a smaller subset of important species is identified for each point.

iii. Species subsets are merged, and only one mechanism is obtained. Sensitivity analysis on species is again carried out on it like in the previous section, until the error theshold is exceeded. At that point, the final set of important species is identified.

iv. Sensitivity analysis on reactions is carried out as described in Section 4.3, and the reactions having a characteristic coefficient lower than the threshold are eliminated. Moreover, if after this operation there are species no longer involved in any reaction, they are eliminated from the final output.

This approach was implemented into `DoctorSMOKE++`, a C++ software based on the open-source software `OpenSMOKE++` [16]. `OpenSMOKE++` is a C++ framework for the numerical simulation of reacting flows with detailed kinetic mechanisms. It allows the resolution of the numerical models of 0D reactors (batch, perfectly stirred, plug flow and shock tube reactors), as well as 1D flames, both premixed and counterflow. It includes interfaces with several open source ODE solvers, and also implements its own in-house solver. `DoctorSMOKE++` supports the MPI standard for parallel computing, thus fully exploiting the *divide-and-conquer* paradigm underlying the multi-step approach devised. It is currently available upon request, and is expected to be released (for academic purposes) for Linux, Mac OS X and Windows systems on `http://creckmodeling.chem.polimi.it` around mid-2016.

4.5 Applications

The effectiveness of the methodology is here demonstrated through two case studies. Section 4.5.1 shows the development of a skeletal kinetic mechanism for the combustion of *n*-decane, i.e. one of the reference alkanes used in surrogate models of real fuels. Then, Section 4.5.2 extends the application of the framework to the development of a Gasoline surrogate for the CFD simulation of ICEs. Both the mechanisms were developed in the $T - P - \Phi$ space indicated in Table 4.1, and are available upon request. They were built up with a target of 15% maximum

Variable	Range
Temperature	$600\,\mathrm{K} - 1800\,\mathrm{K}$
Pressure	$1\,\mathrm{atm} - 50\,\mathrm{atm}$
Equivalence ratio	$0.5 - 2$

Table 4.1: Operating conditions used for the skeletal mechanisms obtained in Sections 4.5.1 and 4.5.2.

error on the final ignition delay, using an intermediate threshold of 7.5% for the local DRGEP phase. Maximum and average errors are defined as:

$$\varepsilon_{\max} = \max_{\mathrm{T-P-\Phi}} (\varepsilon_k) \tag{4.17}$$

$$\bar{\varepsilon} = \frac{\sum_{k=1}^{n} \varepsilon_k}{n} \tag{4.18}$$

where n is the total number of reactors.

4.5.1 *n*-decane

As already said in Chapter 2, real fuels are made up of a huge amount of compounds and isomers, and a direct modeling of such systems is then unfeasible. For this reason, their physical and chemical behavior is reproduced through surrogate compounds. Fuel surrogates are made up of a limited number of reference species, whose properties are well known: thus, they can be used for both experimental and numerical studies in the targeted conditions.

In this background, *n*-decane has been considered one of those reference compounds for representing both aviation [113–115] and diesel [116–118] fuels. Experiments in ideal reactors were carried out in the latest decades, and comprehensive kinetic models were developed, describing its combustion in a wide range of operating conditions. Nevertheless, their size [41, 45] prevented them from a direct application in CFD applications. Therefore, in the recent past skeletal mechanisms were developed *ad hoc* for such a compound [39, 119], thus obtaining a significant degree of reduction in the mechanisms size.

Starting from the lumped model of Ranzi et al. [41], the general framework implemented into `DoctorSMOKE++` was adopted to generate a skeletal mechanism for this fuel. The reduction process was carried out on a parallel, Linux-based architecture, by using 24 cores, and required about 2.4 hours. A maximum error of 15% on ignition delay time was set as target, and 90 adiabatic, constant-volume reactors were uniformly distributed in the operating space indicated in Table 4.1.

Mechanism	Species	Reactions	Max Error %	Mean Error %
POLIMI_1412	451	17848	-	-
DRGEP	140	3302	8.6	2.5
Sensitivity Analysis	100	1555	10.7	2.9
Reactions Sensitivity	100	697	8.8	3.5

Table 4.2: n-decane kinetic models: size of detailed [41] and progressively reduced mechanisms, and related errors.

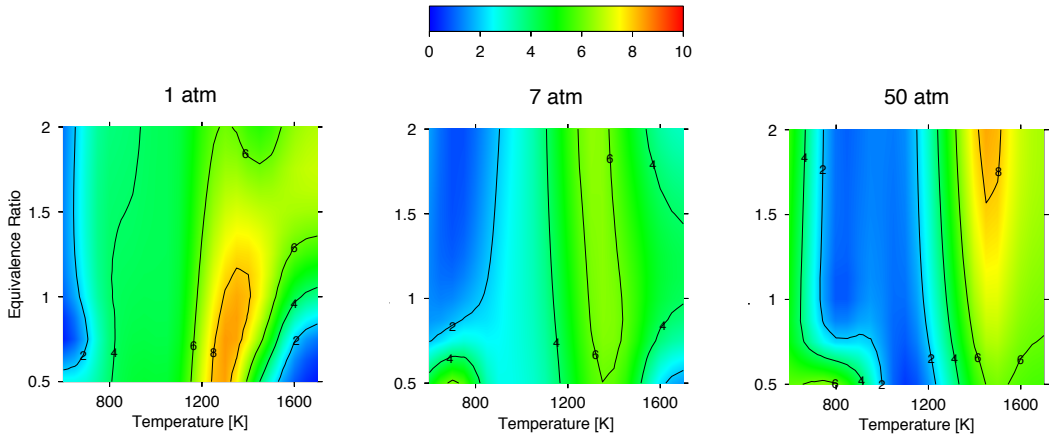

Figure 4.2: Ignition delay error maps for the n-decane mechanism (100 species): comparison at low, intermediate and high pressures.

Table 4.2 shows the dimensions of the obtained skeletal models, compared with the original mechanism, and the related errors.

After carrying out all the reduction steps, the final mechanism is made up of 100 species and 697 reactions. Its validation towards the target property, i.e. ignition delay time is shown in Figure 4.2, where the related error is mapped in the whole operating range. It can be noticed that such an error is kept reasonably low almost everywhere.

A more extensive validation was carried out by comparing the mechanism performance in several case studies, either 0-dimensional or 1-dimensional. In each of them, a direct comparison between original and skeletal mechanism is still possible, since the maximum length of the simulations is of the order of days (with the detailed model). All of them were carried out through the `OpenSMOKE++` solvers [16].

Species Formation in Jet Stirred Reactors. Investigating the oxidation of n-decane in Jet Stirred Reactors (JSR) is a useful test for at least two reasons: (i) like all the heavy n-alkanes, n-decane shows a significant Negative Temperature Coeffi-

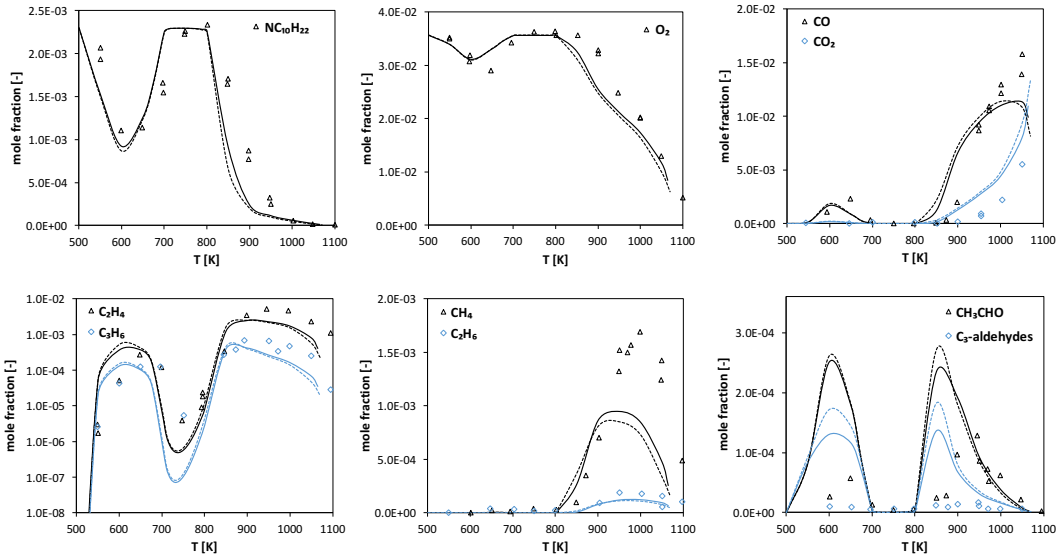

Figure 4.3: Experimental and numerical profiles of species mole fractions after oxidation in a JSR (τ = 1.5 s, P = 1 atm, Φ = 1, $x_{C_{10}}$= 0.23% in a helium-diluted mixture). Continuous lines: POLIMI_1412 mechanism. Dashed lines: *n*-decane skeletal mechanism.

cient (NTC) behavior [20], resulting from the competition between low and high temperature mechanisms. Retaining such a trend in a skeletal mechanism is not straightforward, but is an essential requirement; (ii) Setting ignition delay as target property is not a direct guarantee of accuracy retainment on the single species.

The low temperature oxidation of *n*-decane in JSRs was experimentally studied by Biet et al. [120], who used a stoichiometric *n*-decane/air mixture, diluted with helium to avoid temperature gradients inside the reactor (having a residence time of 1.5 s). Inlet temperature was varied between 550 K and 1100 K, while pressure was atmospheric. Such experiments were numerically reproduced through both detailed and skeletal mechanisms, and the results are shown in Figure 4.3. In most cases, the accuracy in species formation is satisfactorily retained; more significant differences can be observed only for C_3-aldehydes. Moreover, the NTC behavior is correctly reproduced, as shown by the profiles of the major species.

Laminar flame speed. A correct prediction of laminar flame speed is an essential requirement for a kinetic mechanism, especially in those situations where flame propagation is the controlling factor (like internal combustion engines). As pointed out by Ranzi et al. [9], it embodies and manifests the net effects of diffusivity, exothermicity and reactivity. Moreover, models were developed to estimate turbulent flame speed from laminar flame speed [121]. Laminar flame speed of *n*-decane was experimentally investigated by Kumar and Sung [62] and Ji et al. [64] at atmospheric pressure and different inlet temperatures. Following such operat-

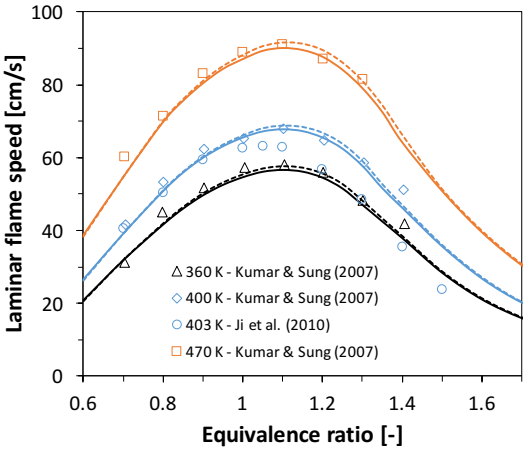

Figure 4.4: Laminar flame speeds of n-decane at atmospheric pressure. Experimental data by Kumar and Sung [62] and Ji et al. [64]. Continuous lines: POLIMI_1412 mechanism. Dashed lines: n-decane skeletal mechanism.

ing conditions, the value of laminar flame speed as a function of the stoichiometric ratio was calculated via both detailed and skeletal mechanisms. The results are shown in Figure 4.4. In this case, too, a good agreeement is observed between detailed and skeletal mechanism. It must be pointed out, though, that this is not an obvious consequence if the reduction algorithm is targeted at matching ignition delay, because species controlling flame propagation may have a low influence on ignition delay. As already done in DRGASA [84] and DRGEPSA [19] algorithms, this can be somehow prevented by properly excluding *a priori* such species from sensitivity analysis. This is done in the multi-step algorithm, too, as already explained in Section 4.2, by setting threshold values to DRGEP (Eq. 4.8) and flux (Eq. 4.9) coefficients to select the marginal species to be analysed. As a result, detailed and original mechanisms behave pretty similarly in predicting flame propagation, too, at the price of a slightly larger kinetic mechanism.

Autoignition of isolated droplets. The combustion of droplets in microgravity conditions allows to study, in very simplified conditions (isolated environment, spherical simmetry, no flow velocity), what occurs in several industrial applications where liquid fuels are involved (gas turbines, diesel engines, etc.) and autoignition is a determining factor. In particular, the microgravity assumption allows treating the problem as 1-dimensional, such that it can be solved with a detailed mechanism, too, in human times. Therefore, the accuracy of a skeletal mechanism can be checked, and time savings can be quantified. A 1D mathematical model of microgravity droplet combustion was implemented by Cuoci et al. [122, 123], and validated through comparison with experimental data carried out for several

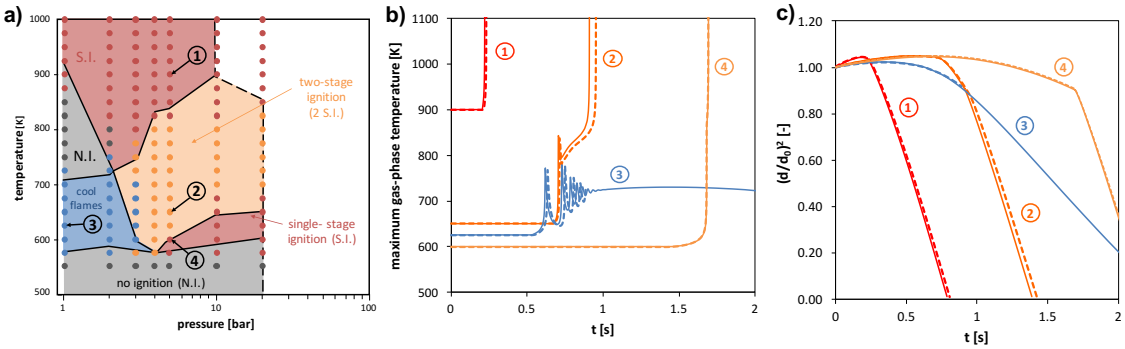

Figure 4.5: Autoignition of n-decane droplets. Panel a): ignition regions, as detected experimentally [124, 125] by using an initial diameter $d_0 = 0.7\,mm$. Numerical predictions by Cuoci et al. [123]. Panel b): Maximum gas-phase temperature for n-heptane droplets.. Panel c): squared dimensionless droplet diameter over time. Continuous lines: detailed model. Dashed lines: skeletal model.

# Simulation	Detailed mech [min]	Skeletal mech [min]	Ratio [-]
1	3453	42	82
2	4290	67	64
3	1318	21	63
4	4725	68	69

Table 4.3: Execution times [min] of autoignition simulations reported in Figure 4.5, and ratio between detailed and skeletal simulations.

n-alkanes in a wide range of temperature and pressure. Different phenomena like no-ignition (NI), cool flame ignition (CF), single-stage (SI) and two-stage (2SI) ignition could be observed according to fuel type, initial temperature, pressure and droplet diameter. Figure 4.5a compares the autoignition modes, as obtained experimentally and numerically via POLIMI_1412 mechanism.

From a kinetic point of view, having a comprehensive mechanism with sufficient accuracy in the whole operating range is then an essential requirement. The four dynamics of autoignition were assessed, one for each characteristic region, with both detailed and skeletal mechanism, and the results are shown in Figure 4.5b. Again, the agreement is satisfactory and confirms what seen so far: while high temperature ignition dynamics are matched very well, the most critical region is where high and low temperature phenomena are competing. On the other hand, even by coupling vaporization to the autoignition problem, the highest errors are of the same order. The most significant differences are observed in curve 2, where the time shift between maximum gas-phase temperature is about 8%. It is worth noting the savings in the related simulations: as listed in Table 4.3, the average ratio between the required times is 70, against a ratio between the respective

	Gasoline	Jet Fuel	Diesel	Biodiesel
Specific gravity at 15°C	0.72 – 0.78	0.77 – 0.83	0.83 – 0.85	0.86 – 0.90
Boiling point range (°C)	30 – 220	150 – 300	200 – 350	260 – 360
Flash point (°C)	−43	38	52 – 60	140 – 170
Autoignition temperature (°C)	370	230	254	-
Research octane number (RON)	91 – 100	-	-	-
Motor octane number (MON)	82 – 92	-	-	-
Cetane number (CN)	< 15	-	45 – 55	55
Lower heating value (MJ/kg)	42 – 44	43 – 44	43 – 45	37

Table 4.4: Physico-chemical properties of the different class of transportation fuels. Adapted from [78].

species of 4.5. This result is in line with the expectations, since the construction and the factorization of the Jacobian matrix are the rate determining steps, and as already said their computational cost scale with the second and the third power of the number of species, respectively.

4.5.2 Toluene Reference Fuel

The use of monocomponent fuels is often too simplistic to mimick the countless physico-chemical properties of interest in transportation fuels, some of which are listed in Table 4.4. Therefore, the use of multicomponent surrogates to reproduce such a behavior has been gaining increasing importance in the latest decades. To this purpose, the state of the art was recently reviewed by Pitz and Mueller [126]. Here, the multi-step approach previously developed is applied for the formulation of a skeletal mechanism of a gasoline surrogate, belonging to the class of Toluene Reference Fuels (TRF). The reference composition by Gauthier et al. [127] was adopted for the ideal reactor calculations: they selected a a 63/20/17 mixture (in mole fractions) of *n*-heptane, iso-octane and toluene as reference composition of the *RD387* gasoline. Such a composition was also the reference for the development of the LLNL model by Mehl et al. [54]. 81 adiabatic, constant volume batch reactors were uniformly spread in the operating space indicated in Table 4.1. In this case, the reduction process required about 5.3 hours on a parallel cluster with 24 cores. Table 4.5 lists the main features of the skeletal mechanisms progressively obtained via `DoctorSMOKE++`.

A final mechanism of 114 species and 845 reactions was then obtained, and the error on the ignition delay time is mapped at three different pressures in Figure 4.6. As a further comparison, Figure 4.7 shows the ignition delay times in a PRF

Version	Species	Reactions	Max Error %	Mean Error %
POLIMI_1412	451	17848	-	-
DRGEP	181	5652	7.3	2.2
Sensitivity Analysis	114	1807	13.5	4.9
Reactions Sensitivity	114	845	17.6	6.0

Table 4.5: POLIMI *RD387* kinetic models: size of detailed and progressively reduced mechanisms, and related errors.

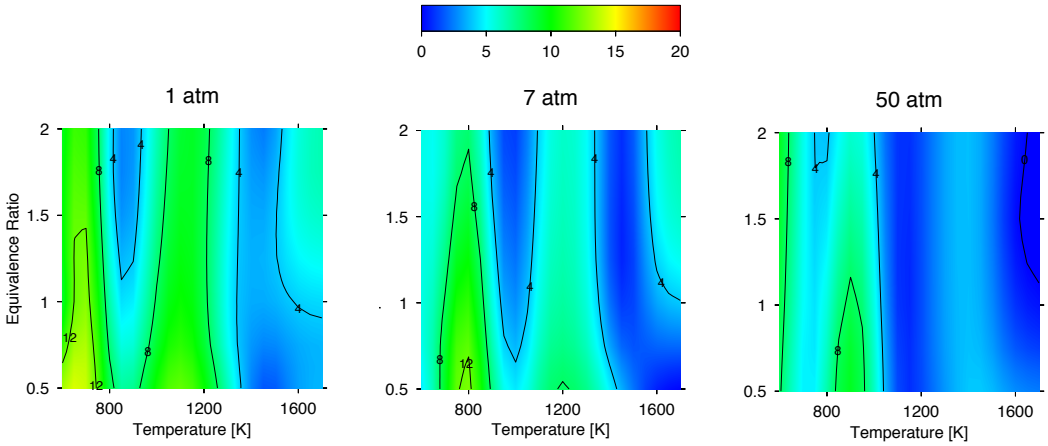

Figure 4.6: POLIMI *RD387* mechanism (115 species) error maps: comparison at low, intermediate and high pressures.

at different iso-octane/n-heptane ratios, as well as the sensitivity of n-heptane/air mixture to equivalence ratio.

Following the recommendation of Sileghem and coworkers [129], the laminar flame speed of a gasoline mixture was calculated with a starting equivolume liquid mixture of n-heptane, iso-octane and toluene (corresponding to a 30.4/27.2/42.4 mixture in mole fractions). Figure 4.8 compares experiments with the values predicted by detailed and skeletal mechanism. The agreement is almost complete, and the skeletal mechanism also behaved well for the three pure components. This results in a high flexibility of the obtained model, which can then represent also TRFs with a different composition from the one used for reduction. Such an agreement in different conditions is also confirmed by the predictions of species formation in n-heptane and iso-octane premixed flames.

Figure 4.9 and 4.10 show that the profiles of both fuel and oxidizer are almost overlapped, while minor differences are experienced for intermediate species. Such deviations are more evident for species not directly related to the reactivity time scales, like benzene.

It must be pointed out that the development of dedicated skeletal mecha-

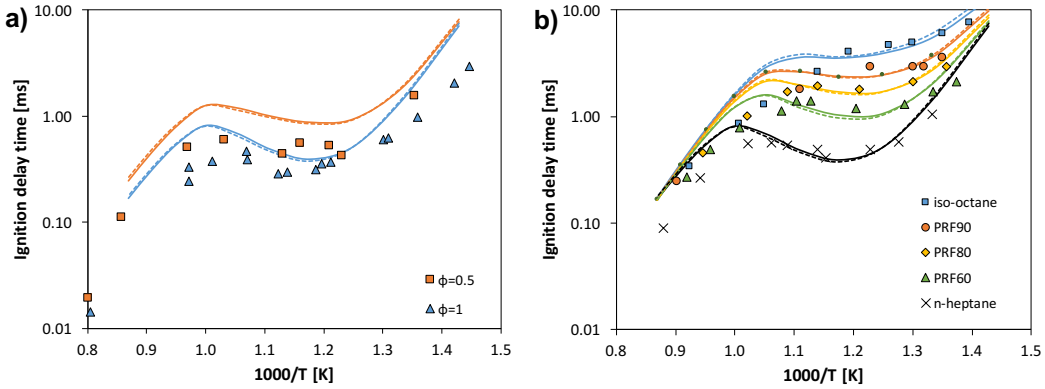

Figure 4.7: a) Sensitivity of *n*-heptane/air mixture to equivalence ratio. Experimental data by Shen et al. [102] b) PRF ignition delay times at P = 40 bar and stoichiometric conditions. Experimental data by Fieweger et al. [128]. Continuous lines: POLIMI_1412 model. Dashed lines: skeletal (114 species) model.

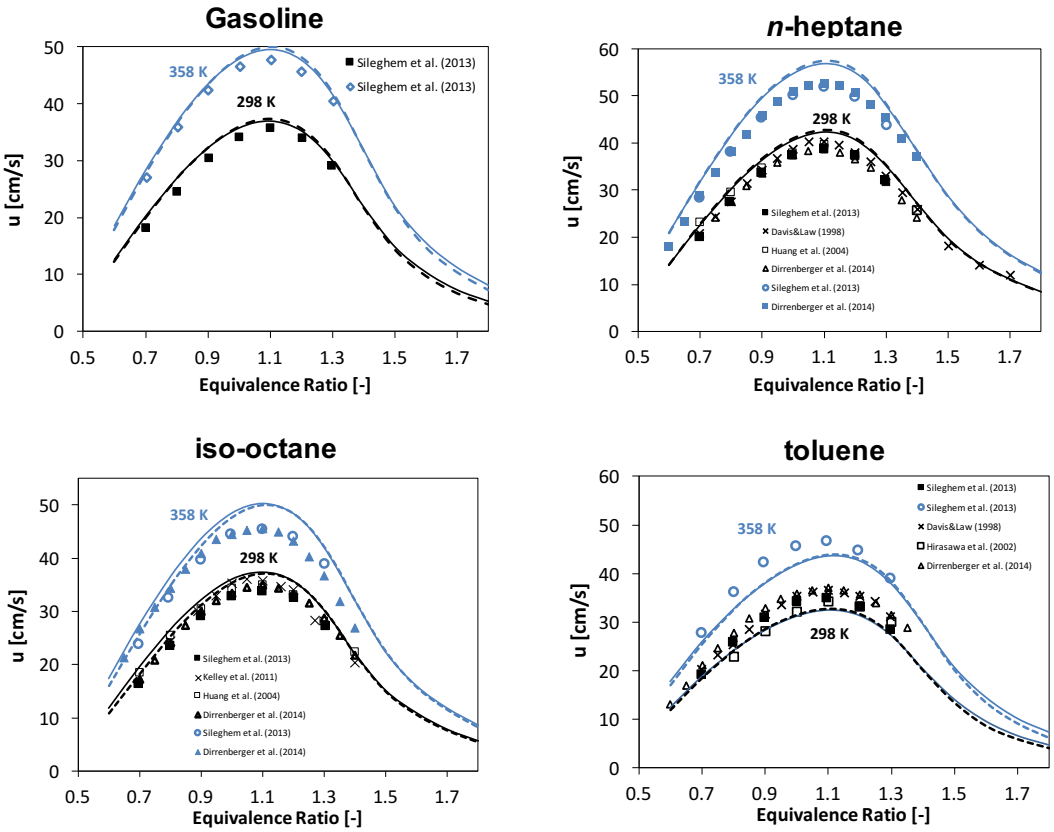

Figure 4.8: Laminar flame speeds of gasoline surrogate (1/3 n-heptane, 1/3 i-octane, 1/3 toluene) and pure components. Continuous lines: detailed model. Dashed lines: POLIMI *RD387* skeletal model. Experimental data from [103, 129–133].

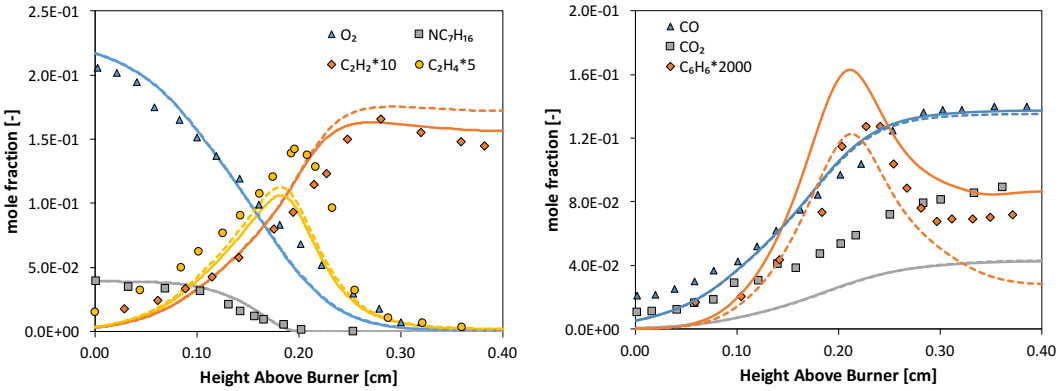

Figure 4.9: Species profiles in a *n*-heptane/O_2/N_2 laminar flame. $x_{n\text{-heptane}} = 3.98\%$; $\Phi = 1.9$; P = 1 bar. Experimental data from [134, 135]. Continuous lines: detailed mechanism. Dashed lines: POLIMI *RD387* skeletal mechanism (114 species).

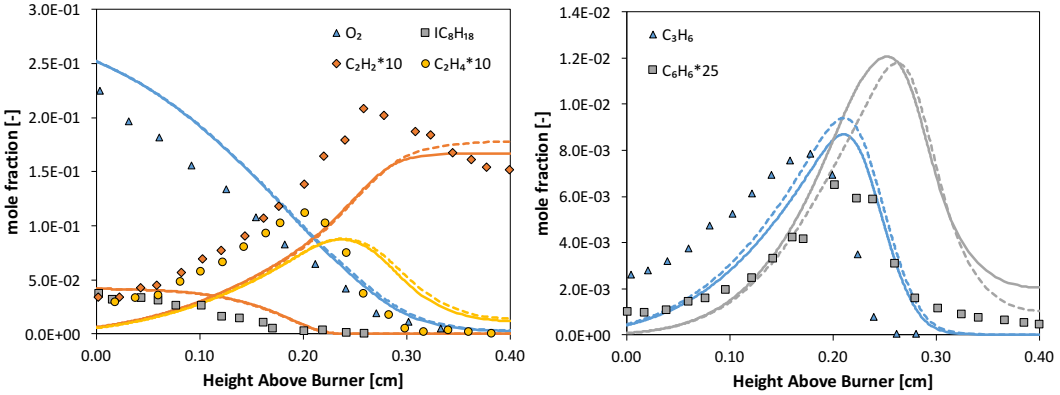

Figure 4.10: Species profiles in a iso-octane/O_2/N_2 laminar flame. $x_{\text{iso-octane}} = 4.23\%$; $\Phi = 1.9$; P = 1 bar. Experimental data from [134, 135]. Continuous lines: detailed mechanism. Dashed lines: POLIMI *RD387* skeletal mechanism (114 species).

Author	Reference	Species	Reactions	Notes
Niemeyer and Sung	[108]	97	873	High-temperature only
Mehl et al.	[54]	312	2606	Not tested on pure components
Cai and Pitsch	[99]	335	1613	Including PAH chemistry
Luong et al.	[15]	171	1620	PRF mechanism.

Table 4.6: Recently available kinetic mechanisms for gasoline surrogate.

nisms for surrogate mixtures is still an almost uncharted territory: Niemeyer and Sung [108] obtained a 233-species skeletal model for a TRF mechanism operating in conditions typical of Homogeneous Charge Compression Ignition (HCCI), and a 97-species mechanism for a TRF fuel operating in Spark Ignition (SI) or Compression Ignition (CI) engines. Mehl et al. [54] developed a 312-species skeletal mechanism for a gasoline surrogate operating in lean conditions, typical of HCCI engines, while Luong et al. [15] obtained a 171-species skeletal model for lean primary reference fuel/air mixtures. More recently, Cai and Pitsch [99] developed an optimized chemical mechanism for PRF/toluene mixtures, consisting of 314 species and 2327 chemical reactions. Those mechanisms are summarized in Table 4.6, and for the sake of completeness, Figure 4.11 compares the performance of POLIMI mechanisms (detailed and skeletal) with all of them.

The smaller dimensions of the POLIMI skeletal mechanism stand out: as previously explained in Chapter 2, they benefit from the upstream lumping approach, thanks to which the starting dimensions are significantly lower than a full model, like the one used by Mehl et al. [54] in their work (about 1550 species and 6000 reactions). The performance benchmarks shown in Figure 4.7, 4.8, 4.9 and 4.10 are a clear indication of validity of the lumping methodology, and the coupling with skeletal reduction approaches shows its best application in the development of surrogate models.

4.6 Species-Targeted Sensitivity Analysis

The development of the Curve Matching framework and its capability to compare different curves, discussed in Chapter 3, found an immediate application in the multi-step algorithm proposed here. As a matter of fact, although the flux-sensitivity coupling is a consolidated approach to retain accuracy on the global reactivity by fixing ignition delay as target property, this is not a guarantee of accuracy in all the phenomena and timescales not directly related to them. The example shown in Figures 4.9 and 4.10 highlighted that species not directly related

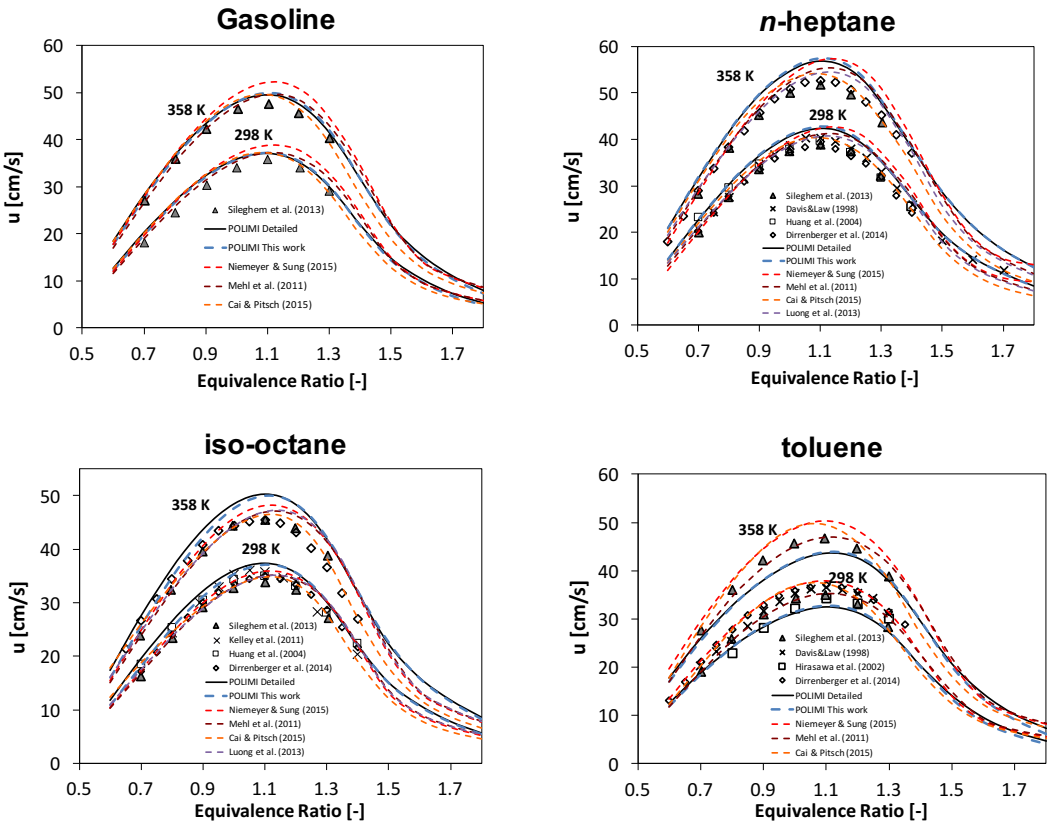

Figure 4.11: Laminar flame speeds of gasoline surrogate (1/3 n-heptane, 1/3 i-octane, 1/3 toluene) and pure components. Continuous lines: detailed model. Dashed lines: POLIMI *RD387* skeletal model. Experimental data from [103, 129–133].

to the ignition delay time, like benzene, may be affected by significant mispredictions. In general, two weaknesses may be highlighted:

- As already pointed out by Lu and Law [136], a reduction algorithm should provide *a priori* error control, in order to guarantee the accuracy of the reduced mechanism. When a specific accuracy is desired on certain species (i.e., reduction is species-targeted), an on-the-fly error control while performing flux analysis is not straightforward, since it would require error quantification in the tested reactors.

- In the same way, sensitivity analysis to the ignition delay time is not applicable as such, because it uses a single value (ignition delay) to gather the importance of a species in the final accuracy of the mechanism. When the dynamics of formation of a species is to be preserved, a different approach must be conceived.

These considerations brought to the coupling between `DoctorSMOKE++` and Curve Matching frameworks, thus obtaining a comprehensive tool to obtain skele-

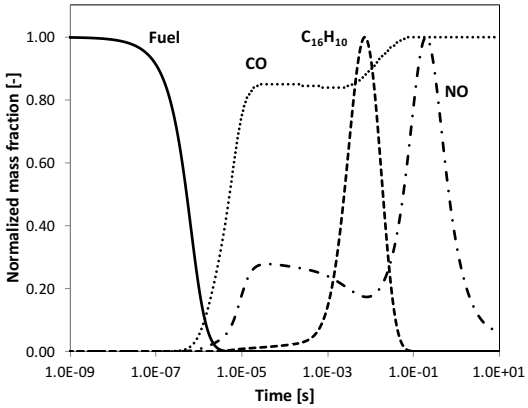

Figure 4.12: Typical time scales and lifetime of several species, as detected in an isothermal plug flow reactor. Fuel: C_3H_8. Oxidizer: air. T = 1900 K. P = 1 atm. $\Phi = 2$. The simulation was carried out through the POLIMI_1412 mechanism [9].

tal mechanisms with the required accuracy on the desired target properties. Such a procedure, fully described in [96], is hereafter summarized.

4.6.1 Sensitivity analysis on species formation

The principle of the procedure described in Section 4.2 was adapted towards a Species-Targeted Sensitivity Analysis (STSA). The first step is common to both approaches, i.e. carrying out DRGEP analysis in each sampled point, using in this case the desired target species to calculate the coefficients of Eq. 4.8. A conservative ε_{DRGEP} is fixed (10^{-3} or lower), and the species with an OIC value smaller than that are removed from the local mechanisms. Then, the marginal species which undergo sensitivity analysis are considered and selected for each point by fixing an upper threshold to $\tilde{R}_i$ (like in the traditional algorithm). According to the typical lifetime of the different species, a lower and an upper threshold are selected, and for each reactor the target molar fraction is obtained as a function of the logarithm of the reactor time. The same profiles are then obtained through the single removal of the marginal species under investigation. Function derivatives are not considered in this case for the sake of simplicity. Each of them is compared to the reference curve via an FDA-based procedure, similar to the one described in Section 3.2. Species profiles are converted into functions through linear interpolation of the obtained solution. Smoothing procedures are not carried out in this case since they would significantly increase the computating time, but after all they are not needed because of the high density of the curves in terms of number of points. In order to quantify the difference between the reference

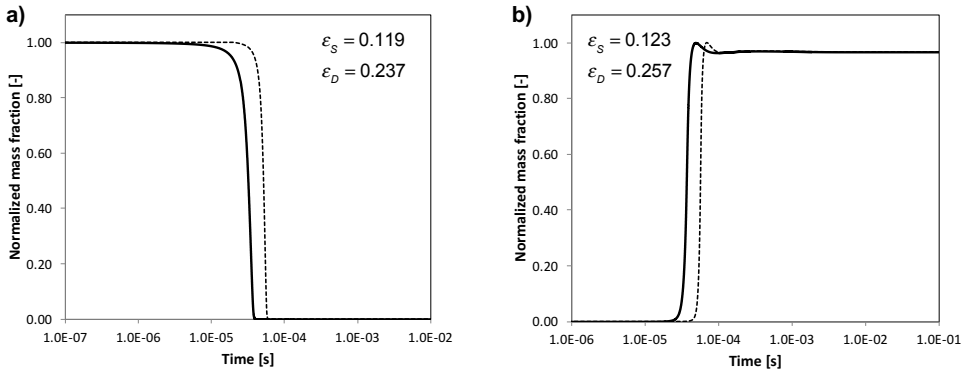

Figure 4.13: Mass fraction time history of a) CH_4 and b) CO_2 in an adiabatic batch reactor. T = 1900 K. P = 1 atm. $\Phi = 2$. Continuous lines: original profiles. Dashed lines: profiles shifted in the x direction. ($dt = 2 \cdot 10^{-5} s$). The simulation was carried out through the POLIMI_1412 mechanism [9].

function f and the tested function g, two dissimilarity measures are created:

$$\varepsilon_D(f,g) = \frac{\|f-g\|}{\max\left(\|f\|, \|g\|\right)} \tag{4.19}$$

$$\varepsilon_S(f,g) = \frac{1}{2}\left\|\frac{f}{\|f\|} - \frac{g}{\|g\|}\right\| \tag{4.20}$$

where ε_D is the normalized L^2-distance between f and g, and ε_S is the Pearson dissimilarity measure between f and g (same as Eq. 3.11). The formulation of Eqs. 4.19 and 4.20 binds both the indices to assume values between 0 and 1.

ε_D is the normalized integral of the residual Sum of Squares, i.e. the same as Eq. 3.9, bound between 0 and 1. In presence of large plateaux (where $f \neq 0$ and $f' = 0$), its value is sensitive to the choice of the boundaries. Figure 4.13 shows two typical cases where it can occur. For illustrative purposes, CH_4 and CO_2 profiles were artificially shifted in order to obtain the dashed lines, and the two error indices (4.19) and (4.20) were calculated. In the first case (Figure 4.13a), moving the left boundary from 10^{-7} to 10^{-6} would increase ε_D from 0.237 to 0.300. Similarly, in Figure 4.13b, changing the right boundary from 10^{-1} to 10^{-3} would result in an increase of ε_D from 0.257 to 0.336.

On the other hand, ε_S is insensitive to boundary shifts, as long as they occur in the flat regions, but is insensitive to vertical dilatations, too, as already mentioned in Eq. 3.17. To illustrate this, Figure 4.14 shows the mass fraction profiles of $C_{16}H_{10}$ and NO, obtained through the simulation of an isothermal batch reactor, then dilated in order to obtain the dashed lines. As a result, the value of ε_S is zero in both cases, whilst ε_D is affected by such a dilatation, and is then higher

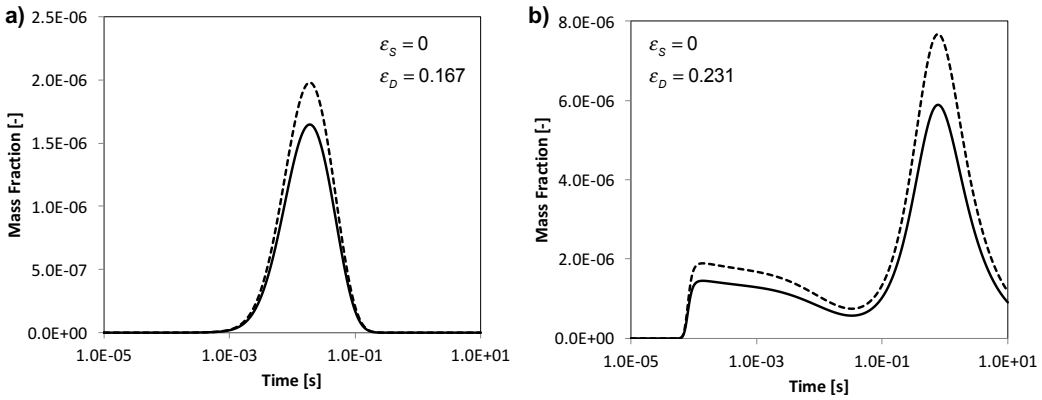

Figure 4.14: Mass fraction time history of a) $C_{16}H_{10}$ and b) NO in an isothermal batch reactor. T = 1800 K. P = 1 atm. $\Phi = 2$. Continuous lines: original profiles. Dashed lines: original profiles multiplied by a factor 1.2. The simulation was carried out through the POLIMI_1412 mechanism [9].

than zero. The use of both indices makes then the procedure more robust and comprehensive.

The creation of the species ranking is similar to the procedure described in Section 3.2.2, whereas only two indices are considered. For each reactor, the median value and the Median Absolute Deviation (MAD) are computed. The latter corresponds to the median of the absolute deviations from the median values:

$$\mathrm{MAD} = \mathrm{median}_p \left(|\varepsilon_p - \mathrm{median}_i \left(\varepsilon_i \right)| \right) \tag{4.21}$$

For each i-th species, both indices are converted in terms of normalized deviations from the median value:

$$\hat{\varepsilon}_{Di} = \frac{\varepsilon_{Di} - \tilde{\varepsilon}_D}{MAD_D} \tag{4.22}$$

$$\hat{\varepsilon}_{Si} = \frac{\varepsilon_{Si} - \tilde{\varepsilon}_S}{MAD_S} \tag{4.23}$$

where $\tilde{\varepsilon}_D$ and $\tilde{\varepsilon}_S$ are the median values of all the tested models, and MAD is related to considered errors subset. Like in Eq. 3.21, the normalized values are summed up and a species ranking is created for each k-th reactor. This ranking is used to progressively remove species from the local subset, while both indices are lower than defined threshold values:

$$\varepsilon_{D_k} < \check{\varepsilon}_D \tag{4.24}$$

$$\varepsilon_{S_k} < \check{\varepsilon}_S \tag{4.25}$$

After completing the procedure for each point, the species subsets are merged,

and like in Section 4.2 an overall sensitivity analysis on species is carried out considering the whole $\mathrm{T}-\mathrm{P}-\Phi$ range:

$$E_{D_i} = \max_{\mathrm{T-P-\Phi}} \varepsilon_{D_i} \tag{4.26}$$

$$E_{S_i} = \max_{\mathrm{T-P-\Phi}} \varepsilon_{S_i} \tag{4.27}$$

The normalized deviations (4.22) and (4.23) are calculated, and the removal is carried on while the conditions (4.24) and (4.25) are valid on the whole range::

$$\max_{\mathrm{T-P-\Phi}} (\varepsilon_{D_k}) < \check{E}_D \tag{4.28}$$

$$\max_{\mathrm{T-P-\Phi}} (\varepsilon_{S_k}) < \check{E}_S \tag{4.29}$$

where $\check{E}_D$ and $\check{E}_S$ are two user-defined threshold values.

4.6.2 Reactor type and species dynamics

Flux-based skeletal reduction has usually been carried out through the analysis of reaction states in transient autoignition phenomena, although in the past, DRG and DRG-based approaches have also considered PSRs for the evaluation of the interaction coefficients [19,75,108]. Moreover, flux analyses have always considered adiabatic reactors because of the focus on the overall reactivity. Therefore, being ignition delay the only target, coupling mass and energy balance in an ideal, dynamic reactor is the most obvious way to reach the target.

Conversely, when the interest is directed towards the dynamics of formation of one (or more) species, the analysis of adiabatic reactors might be counterproductive. The main danger could reside in masking the time scales of low temperature phenomena, whose importance may become even competitive with the higher temperatures in operating conditions dissimilar from adiabatic reactors, where they would be insignificant. A representative example can be provided by the different mechanisms concurring to $\mathrm{NO_x}$ formation, which is kinetically controlled. It occurs through two main reaction paths [137], known as thermal and prompt mechanism. Thermal mechanism is very sensitive to temperature, and the $\mathrm{NO_x}$ formation increases exponentially with it; its time scales are of the order of the second. Prompt mechanism is not so sensitive to temperature as the thermal, since it depends on the hydrocarbon radicals in the first pyrolysis steps of the hydrocarbon chain, and it has then characteristic times of the order of milliseconds. If adiabatic simulations are used for mechanism reduction, the $\mathrm{NO_x}$ formation through the prompt mechanism would be overcome by thermal,

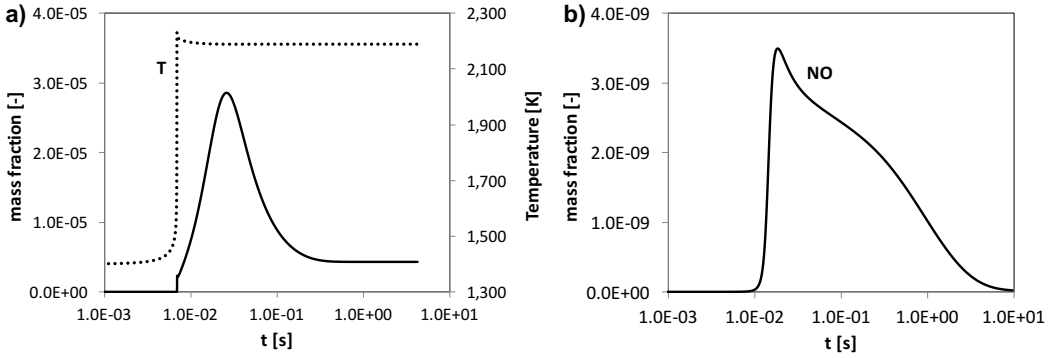

Figure 4.15: Mass fraction time history of NO in a) adiabatic and b) isothermal batch reactor. Fuel = CH_4. Oxidizer: air. $T_0 = 1400\,K$. P = 1 atm. $\Phi = 3$. The simulation was carried out through the POLIMI_1412_NOx [9] mechanism.

once ignition has occurred, and adiabatic flame temperature has been reached. The resulting skeletal mechanism would be able to accurately replicate trends in autoignition phenomena, but not in different systems, where ignition may not be the only determining factor, and mixing conditions might be not ideal. Figure 4.15a shows the nitrogen formation over time in an adiabatic batch reactor, in fuel-rich conditions. The two mechanisms bringing to the formation of NO may be distinguished, as well as the final reduction of NO in rich conditions because of the reburning mechanism [138]. However, the quantitative formation of NO through the prompt path is much lower $(5 - 10\%)$ than the maximum amount, because the temperature rise due to autoignition increases the importance of the thermal path, which ultimately overwhelms the prompt. By using isothermal reactors, decoupling mass and energy balance provides a clearer reproduction of the involved time scales, and the relative importance of the different mechanisms for an assigned set of initial conditions. Figure 4.15b shows the mass fraction profile of NO in an isothermal batch reactor, with the same initial conditions as Figure 4.15a. Expectably, in the considered conditions the prompt mechanism is the only formation path present, due to the high activation energy of the thermal one. The varying importance of the two submechanisms as a function of temperature is still considered, though, by setting up isothermal reactors at different operating temperatures: in other words, it is assumed that if accuracy is retained for the dynamics of isothermal mixtures, and the temperature range is sufficiently sampled, non-isothermal phenomena will be reproduced with a comparable degree of accuracy, too.

4.7 Skeletal mechanisms for NO_x chemistry

The validation of STSA approach was carried out through the generation of skeletal mechanisms for methane combustion with the inclusion of NO_x chemistry. So far, the automatic generation of skeletal models for species not directly dependent on autoignition have not been obtained. In the past a decoupling methodology has been applied, based on an upstream removal of the sub-model of interest, application of skeletal reduction on the remaining mechanism, and merging the two subsets at the end of it [139].

Variable	Range
Temperature	800 K – 1800 K
Pressure	1 atm
Equivalence Ratio	0.5 – 2

Table 4.7: POLIMI CH_4/NO_x: Operating conditions used for reduction.

Reduction is carried out in isothermal, constant pressure batch reactors, and starting conditions are set up to cover the operating space identified in Table 4.7. The POLIMI detailed mechanism for the combustion of C_1-C_3 fuels with NO_x chemistry was used (version 1412), made up of 148 species and 3211 reactions. First, a maximum 15% error on ignition delay time was used to obtain a core mechanism of 27 species and 181 reactions, after sensitivity analysis on ignition delay. Then, NO was identified as target species, and two different threshold values of ε_D and ε_S were set, in order to assess their influence on the final accuracy. Then, the two obtained mechanisms underwent sensitivity analysis to reactions, where CH_4, O_2 and NO were used as target species. Table 4.8 shows the progressive sizes of the different mechanisms.

Interestingly, the size of the most accurate mechanism decreased after merging and sensitivity analysis. This must not be considered surprising, and is due to the strong coupling betweeen species. As a result, the progressive removal process may retain a species A, whose importance with respect to the concerned target is significant only when coupled to a species B. If B is successively removed, the

			Core mech		NO sub-mech		Final mech	
ID	ε_D	ε_S	Species	Reactions	Species	Reactions	Species	Reactions
1	0.15	0.05	27	181	60	623	59	459
2	0.3	0.1			55	490	55	400

Table 4.8: Threshold values and sizes of the two NO_x mechanisms obtained via STSA.

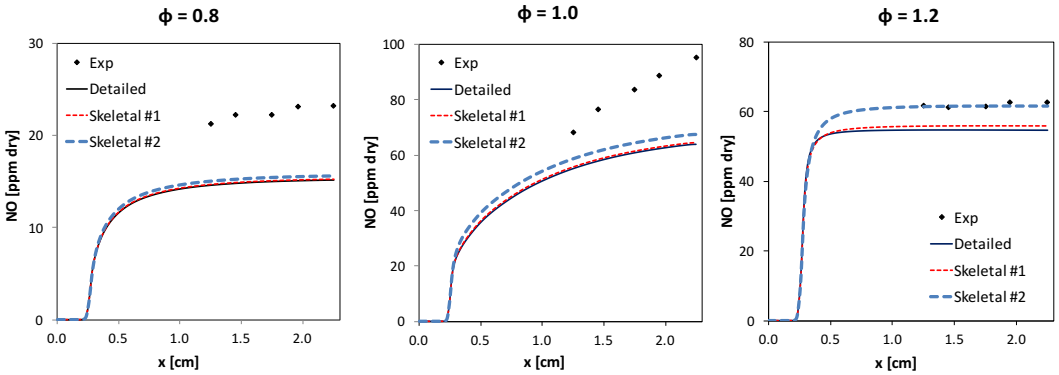

Figure 4.16: NO formation in the postflame zone of a laminar premixed flame (CH_4/O_2) at atmospheric pressure. Experimental data by Konnov et al. [140].

importance of A becomes negligible, but this cannot be detected by the algorithm because the decision of retaining A has already been made. This issue is fixed in the last step, when sensitivity analysis on reactions finds a negligigble sensitivity coefficient in all the reactions where A is involved, and removes it then from the final mechanism.

The four species retained in mechanism 1, but not in mechanism 2 are mostly non-nitrogen species, i.e. the carbon radical (C), acetyl radical (C_2H), propane (C_3H_8) and isocyanate radical (NCO). Since they do not belong to the 27-species core mechanism (and 3 of them do not even contain nitrogen), they could not be detected via a decoupling methodology. A NO-directed analysis proved then necessary to quantify their importance in the accuracy of the final output.

For both mechanisms, an extensive benchmark was carried out through comparison with experimental data and performance of the detailed mechanism. Focusing on the operating conditions used by Konnov and coworkers [140], the NO molar fractions in the postflame region of a CH_4/O_2 laminar flame at atmospheric pressure was assessed. A parametric study to equivalence ratio was performed, by varying it from 0.8 to 1.2, and 3 axial profiles are shown in Figure 4.16. An almost total agreement can be observed between detailed and the 59-species mechanism, but a good agreement can be observed for the 55-species one, too, since the highest relative errors amount to about 15% in the worst case. The observed errors are higher at a higher equivalence ratio.

Similarly, the formation of NO in a CH_4/H_2/air flame (with the two fuels being in a 85/15 ratio) was calculated, by reproducing the experimental conditions of Coppens et al. [141]. Figure 4.17 shows the obtained results: the laminar flame speed preditions (left panel) confirm the solidity of the core mechanism, since the two curves are completely overlapped between detailed and skeletal model. It is

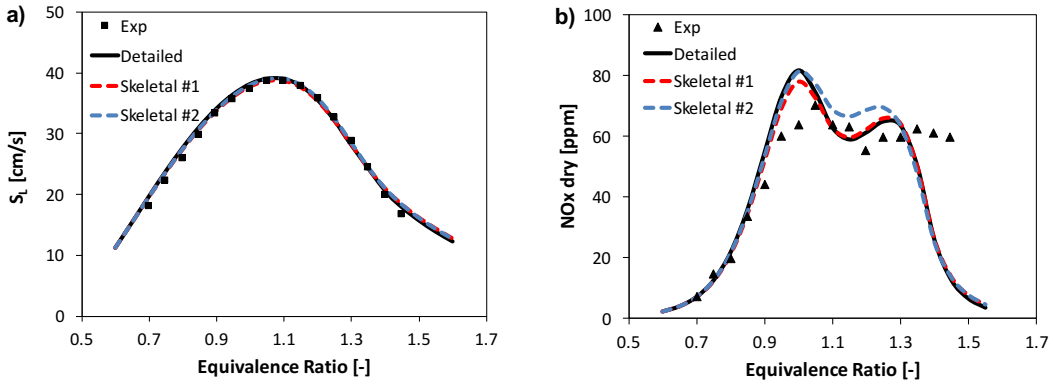

Figure 4.17: NO formation in a laminar premixed flame (85% CH_4/ 15% H_2 in air). a) Laminar Flame speed. b) NO concentration (dry) evaluated at 10 mm. Experimental data by Coppens et al [141].

worth remarking that NO profiles (right panel) show a double peak at $\Phi = 1.05$ and $\Phi = 1.35$, which is well predicted by skeletal mechanisms, too. This is due to the competition between the two formation pathways, bringing to the formation of NO. The maximum at $\Phi = 1.05$ corresponds to the highest temperature of the burning flame, reached in proximity of stoichiometric ratio (about 2230 K). here, the thermal path is dominant. On the other hand, the prompt path is emphasized in richer conditions [137], and this results in the second maximum at $\Phi = 1.35$. Both detailed and skeletal mechanisms are not able to predict the continued formation of NO at higher equivalence ratios, rather showing a drop in their formation. This was also experienced by Coppens and coworkers [141], though, and was attributed to possible buoyancy effects, possibly leading to an exchange of oxygen with the surrounding air. This would allow the continuation of the prompt NO path, even at higher equivalence ratios, where the reduction of NO to N_2 increases in importance.

Lastly, the accuracy of the skeletal mechanisms was assessed through the analysis of laminar counterflow diffusion flames. In addition to being a 1D case which completes then the validation of the obtained models, a high interest in this setup is motivated by the theoretical foundations of flamelet-based models of turbulent combustion [142], through which turbulent flow and mixture fields are solved separately from chemistry. In the past, they were successfully applied to the prediction of nitrogen oxides in turbulent, nonpremixed flames [143, 144]. Several counterflow configurations were investigated for the analysis of NO emissions [145–147]. For the purposes of this validation, the experimental configuration of Shimizu et al. [145] has been numerically reproduced, and the operating conditions of the two flames investigated are reported in Table 4.9. Air was used as oxidizer in both

#	T_{fuel} $[K]$	T_{ox} $[K]$	P $[atm]$	v_{fuel} $[cm/s]$	v_{ox} $[cm/s]$	d $[cm]$	a_c $[1/s]$
1	300	300	1	15.2	12.5	1	50
2	300	300	1	70	70	1.5	163

Table 4.9: Counterflow flame setup of CH_4/Air flames in the experimental setup of Shimizu et al. [145].

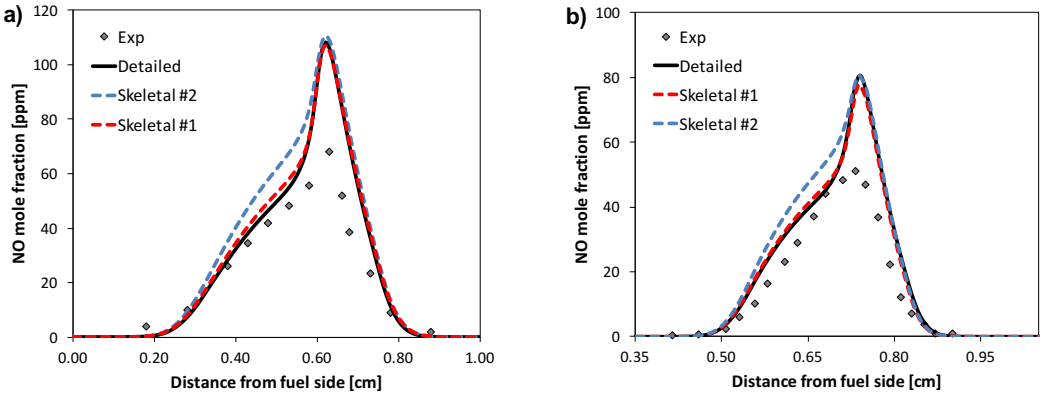

Figure 4.18: NO formation in laminar counterflow flames. Experimental data by Shimizu et al. [145].

experiments. Due to the low involved temperatures (inlet temperature is 300 K, while the peak value is 2000 K), the prompt mechanism is prevailing. The NO profiles in Figure 4.18 show again a satisfactory agreement between detailed and skeletal mechanisms. The peak location is also well caught by both of them, with a maximum 2-5% error on its absolute value. This serves as a further confirmation that most of the accuracy on the prompt mechanism has been satisfactorily retained in the reduction procedure.

Further validation case studies are not reported in this Thesis for the sake of compactness, but are available in [96] as supplemental material.

4.8 Conclusions

The first part of the activity presented in this Thesis has been focused on the development of a systematic methodology aimed at obtaining manageable kinetic mechanisms according to the desired target properties. It has been carried out following two basic principles: (i) generality of the procedure, such that it can be applied to any detailed mechanism, once the operating conditions and target properties are known; (ii) user-friendliness, so that it can be widely used as a preprocessing tool before carrying out more computationally demanding applications. For these reasons, a multi-faceted approach proved necessary and was then implemented. From a kinetic standpoint, the lumping simplification successfully

provided an upstream reduction, without sacrificing accuracy on both reactivity and species formation, and its coupling with skeletal reduction proved a synergistic combination to reach an optimal final size. On the other hand, generality was attained by leveraging the Curve Matching framework and its capability to quantify the difference between curves in terms of dissimilarity measures and error indices. The development of a Species-Targeted Sensitivity Analysis was the final output of such integration, and skeletal reduction can now be headed towards the desired target property, be it reactivity (i.e. Ignition Delay Time) or the dynamics of formation of a specific species.

The overall methodology has been implemented into a structured, multistep approach based on the consolidated coupling between flux analysis and sensitivity analysis. Three main improvements to the traditional approach were introduced:

i. Split of sensitivity analysis on species into a local, *divide-and-conquer* research of the minimum number of species in the $\mathrm{T} - \mathrm{P} - \Phi$ considered space, followed by a global procedure. Considering that this is the heaviest part of the methodology, a significant speedup was obtained.

ii. Introduction of a restart factor ρ, i.e. a dynamic recalculation of species ranking, updated with a frequency dependant on the size of the marginal species subset.

iii. Improvement on the selection of marginal species in the sensitivity analysis phase, through an additional criterion based on production and consumption rates.

The final output, `DoctorSMOKE++`, was succeffully used in several works for the reduction of kinetic mechanisms [55, 78, 96, 148]. Its completion constitutes a solid starting point for the use of detailed chemistry data in large-scale simulations. As a matter of fact, a significant breakthrough may be provided in several fields, where the current use of simplified mechanisms prevents a comprehensive understanding of such phenomena where the role of chemistry may be determining. The next Chapters show two applications in this direction.

CHAPTER 5

Multicomponent droplet ignition in a homogeneous spray/air mixture

As already shown in Chapter 2, a detailed chemical modeling of real fuels is an impossible task because of the high number of involved species, which exponentially grows with the molecule size. For this reason, a common practice in combustion modeling is trying to emulate their physico-chemical properties (Table 4.4), which determine fuel behavior in the related combustion devices, through the use of surrogate fuels [126,149]. Main topics of discussion have focused on the selection of the set of species constituting the surrogate, their relative composition, and the specific properties to be matched by a particular surrogate mixture. In order to provide a comprehensive fuel description, both physical (density, molecular weight, H/C ratio, viscosity, etc.) and chemical (ignition delay, flame propagation, soot formation, etc.) targets should be ideally kept into account. Few studies have actually focused on both of them [150, 151]. More often [114, 152], major emphasis was attributed to the description of the gas-phase behavior. However, this choice neglects the interaction between liquid and gas phase, which can actually be important in such devices like gas turbines and diesel engines.

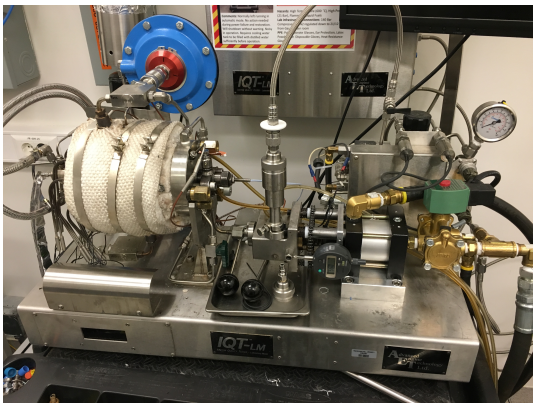

Figure 5.1: Ignition Quality Tester (IQT) - courtesy of King Abdullah University of Science and Technology (KAUST).

Moreover, constraining the surrogate formulation to meet specific targets does not imply a complete knowledge of its behavior. Combustion devices operate over a wide range of conditions, and the evaluation of conditions that affect the two-phase interaction in combustion, such as temperature, pressure or droplet diameter, introduce a substantial degree of complexity if included in the fuel formulation. For example, it is widely acknowledged [115] that the ignition delay time is one of the key properties to be reproduced by surrogate fuels. For both jet and diesel fuels, ignition delay time is usually contained in frameworks for the surrogate formulation through the experimental measurement of the Derived Cetane Number (DCN). Such measurement is carried out through a standardized procedure [153], within the Ignition Quality Tester (Figure 5.1). As a result, no direct control over droplet size distribution or local equivalence ratio is possible, and the obtained value is to be considered as a global estimation of the fuel ignition propensity. Therefore, a downstream analysis of the influence of operating parameters on the ignition delay time can be of paramount importance to possibly further constrain a surrogate description.

At the same time, fundamental studies on the two-phase ignition of real fuels have been carried out. In order to isolate chemical processes from other phenomena affecting combustion in real devices, and to make the problem computationally tractable using detailed kinetic mechanisms, they have usually considered idealized conditions (isolated environment, spherical simmetry, no slip velocity). So far, most attention has been dedicated to single-component droplet combustion both experimentally [124, 125, 154] and numerically [122, 123, 155, 156]. Indeed, the study of multicomponent fuel droplets adds theoretical and computational complexities to existing models, because it requires (i) the consideration of liquid-phase internal diffusion, (ii) non-ideal phase equilibrium and (iii) extended kinetic

mechanisms, to include pyrolysis and oxidation paths of all the fuel components. On the other hand, the ignition of multicomponent fuel droplets may be influenced by preferential evaporation and internal composition gradients resulting from evaporation itself. This has been already recognized in automotive applications [157–159], but so far it has not been investigated in aviation fuels at gas-turbine relevant conditions.

As a direct application of the methodology developed in the first part of this Thesis, the effects of multicomponent diffusion and preferential evaporation on the ignition of fuel mixtures are investigated in this Chapter. In numerical terms, the highest complexity is represented by the significant increase in the size of kinetic mechanism. In droplet fundamental studies, the use of a detailed scheme is not possible even for the simplest liquid fuels like *n*-heptane, where the number of species would exceed ~500 [36]. Moreover, if one also considers that (i) aviation fuels are heavier than *n*-heptane and that (ii) at least 3-4 species are present in a fuel surrogate, the need of a different approach becomes apparent. To isolate the phenomena under investigation from the intricate coupling with the gas phase transport arising in two-phase flow combustion, this study considers an idealized configuration in which the gas phase is represented by a semi-batch reactor. A mathematical model is developed to represent the spatial evolution of the liquid phase inside monodispersed droplets, and the temporal evolution of the homogeneous gas phase. Such model is presented in Section 5.1, where its single components are described in detail. In Section 5.2, the model is applied for the study of the autoignition of the 2nd-generation surrogate of the POSF 4658 Jet-A fuel [160]. The effects of droplet diameter and global equivalence ratio on the ignition process is carried out, and the overall relevance of multicomponent evaporation is quantified through a comparison with a zero-diffusivity (or point-particle) model, i.e. the state of the art in the current CFD two-phase solvers.

5.1 Mathematical model

The model investigates the evaporation and ignition of a monodispersed spray cloud in a homogeneous gas phase, in order to isolate the effect of preferential evaporation from gas-phase transport. Indeed, previous numerical studies had shown that (i) in non-premixed systems, for low to moderate strain rates, ignition exhibits a behavior similar to that found for homogeneous systems, with slower dynamics because of diffusive losses [161]; and (ii) that in droplet-cloud systems, the ignition process tends to behave in a homogeneous way with decreasing droplet diameters [155]. As such, this configuration can be regarded as a

two-phase extension to homogeneous gas-phase ignition studies, widely employed for chemistry studies. Ignition was considered either if occurring during droplet ignition, or after it has completely evaporated. Five basic assumptions are made:

- Spherically simmetric and monodisperse droplets;
- Absence of reactions in liquid phase;
- Dynamic equilibrium with the underlying gas phase (no slip velocity);
- Constant pressure;
- Gas/liquid equilibrium at the droplet interface.

5.1.1 Two-phase model

Conservation of species, energy and velocity is solved in spherical coordinates [122]:

$$\rho_L \left(\frac{\partial Y_{L,i}}{\partial t} + v_L \frac{\partial Y_{L,i}}{\partial r} \right) = - \frac{1}{r^2} \frac{\partial}{\partial r} \left(r^2 j_{L,i} \right), \tag{5.1}$$

$$\begin{aligned} \rho_L C_L \left(\frac{\partial T_L}{\partial t} + v_L \frac{\partial T_L}{\partial r} \right) =& \frac{1}{r^2} \frac{\partial}{\partial r} \left(r^2 k_L \frac{\partial T_L}{\partial r} \right) \\ & - \sum_i j_{L,i} C_{L,i} \frac{\partial T_L}{\partial r}, \end{aligned} \tag{5.2}$$

$$\frac{\partial \rho_L}{\partial t} + \frac{1}{r^2} \frac{\partial}{\partial r} \left(r^2 \rho_L v_L \right) = 0, \tag{5.3}$$

where the subscript L refers to liquid-phase properties. ρ is the density, v is the convective velocity, Y_i is the i-th species mass fraction , r is the radial coordinate, j is the diffusion flux, k is the thermal conductivity. $C_{L,i}$ and C_L are respectively the heat capacity of the i-th species and of the mixture.

Diffusion fluxes are described through Stefan-Maxwell theory [162]. Therefore, differently from a Fick-based approach, the diffusion flux of the i-th species depends on the composition of the overall mixture. In radial coordinates, molar diffusion fluxes $\mathbf{J}_L$ are then calculated by solving the linear system:

$$\mathbf{J}_L \cdot \mathbf{B} = -c_{L,tot} \mathbf{\Gamma} \frac{\partial \mathbf{x}}{\partial r} \tag{5.4}$$

where $c_{L,tot}$ is the liquid-phase concentration, $\frac{\partial \mathbf{x}}{\partial r}$ is the radial gradient of molar

fractions. The $\mathbf{B}$ matrix is evaluated as:

$$\begin{cases} B_{ik} = -x_i \left(\frac{1}{\mathcal{D}_{ik}} - \frac{1}{\mathcal{D}_{in}} \right) & i \neq k \\ B_{ii} = \frac{x_i}{\mathcal{D}_{in}} + \sum_{\substack{j=1 \\ j \neq i}}^{n} \frac{x_j}{\mathcal{D}_{ij}} \end{cases} \tag{5.5}$$

where $\mathcal{D}_{ij}$ is the Stefan-Maxwell binary diffusion coefficient, calculated following Wesselingh and Krishna [163]:

$$\mathcal{D}_{ij} = \left(\mathcal{D}_{ij}^{0} \right)^{(1+x_j-x_i)/2} \cdot \left(\mathcal{D}_{ji}^{0} \right)^{(1+x_i-x_j)/2} \tag{5.6}$$

and, on turn, $\mathcal{D}_{ij}^{0}$ is the infinite dilution diffusion coefficient of the i-th species into j, which can be evaluated through the Siddiqi-Lucas correlation [164], for example, for both polar and non-polar systems. $\mathbf{\Gamma}$ is the activity matrix, whose elements are defined as:

$$\Gamma_{ij} = \delta_{ij} + x_i \left(\frac{\partial \ln \gamma_i}{\partial x_j} \right)_{T,P,x_{k \neq j=1 \ldots n-1}} \tag{5.7}$$

where γ_i is the i-th activity coefficient, evaluated through a UNIFAC approach [165]. Note that $\mathbf{J}_L$, $\mathbf{B}$ and $\mathbf{\Gamma}$ are of order $n-1$, because the n-th diffusion flux is not independent, and is evaluated through flux closure:

$$J_n = -\sum_{i=1}^{n-1} J_i \tag{5.8}$$

Molar fluxes $\mathbf{J}_L$ are then converted into mass $\mathbf{j}_L$ [162] to make them homogeneous into Eqs. 5.1 and 5.2.

Spherical simmetry implies a zero-velocity boundary condition at the center, and homogeneous Neumann conditions for temperature and mass fractions. Interface properties are evaluated through termodynamic equilibrium, where the fugacity of both phases is evaluated through the Peng-Robinson equation of state [166], and mass/energy flux continuity. The set of equations is discretized using an adaptive grid, with local adaptation near the droplet interface. 30 grid points are used for liquid-phase discretization, since it had been previously shown [122, 123] that a further refinement did not bring about significant changes in the model output.

Liquid/gas phase coupling is based on an equilibrium model based on the Spalding mass-transfer model [167]: the evaporation flux of i-th species and the heat

flux at the droplet surface are given by:

$$\phi_{s,i} = \frac{\dot{m}_{evap,i}}{\pi d_l^2} = -\frac{1}{\pi d_l^2}\frac{\mathrm{Sh}_i m_d}{3\mathrm{Sc}_i \tau_d}\ln(1+\mathrm{B_{M,}}_i), \tag{5.9}$$

$$\phi_{s,T} = \frac{\dot{T}}{\pi d_l^2} = \frac{1}{\pi d_l^2}\left[\frac{\mathrm{Nu}c_p f_2}{3\mathrm{Pr}c_L\tau_d}(T - T_{L,s}) + \frac{\sum_{i=1}^{N}\dot{m}_{ev,i}l_{v,i}}{m_d c_L}\right] \tag{5.10}$$

where the subscript s refers to droplet surface conditions. In Eqs. 5.9 and 5.10, m_d is the droplet mass and Sh_i , Sc_i and $\mathrm{B}_{M,i}$ are the Sherwood number, the Schmidt number and the mass Spalding number of the i-th species. The droplet relaxation time is $\tau_d = \bar{\rho}_L d_L^2/18\mu$ with $\bar{\rho}_L$ being the average droplet density, d_L is the droplet diameter, and μ the dynamic gas viscosity. Nu is the Nusselt number, Pr is the Prandtl number and $l_{v,i}$ is the latent heat of evaporation of the i-th species. f_2 is a correction factor to account for the Stefan flux in the interface heat balance.

Finally, the 0D semi-batch reactor equations for the gas-phase mass fractions and temperature are coupled to the liquid phase through the droplet number density n_L:

$$\frac{\partial \rho Y_i}{\partial t} = \dot{\omega}_i + n_L \delta_{i\{f\}}\dot{m}_{i,evap}, \tag{5.11}$$

$$c_p\frac{\partial \rho T}{\partial t} = \dot{\omega}_T + n_L\left[c_L m_d \dot{T} + \sum_{i\in\{f\}}\dot{m}_{i,evap}\left(c_{p,i}T_{L,s} + l_{v,i}\right)\right] \tag{5.12}$$

where $\delta_{i\{f\}}$ is the Kronecker delta function, equal to 1 if the species belongs to the liquid species set (i.e. the fuel), and 0 otherwise, $\dot{\omega}_i$ is the chemical source term of the i-th species, $\dot{\omega}_T = -\sum_i h_i\dot{\omega}_i$ is the heat release rate, with h_i the enthalpy of i-th species and $c_{p,i}$ is the constant-pressure specific heat of the i-th species. The droplet number density n_L is related to the global equivalence ratio Φ and the initial droplet diameter $d_{L,0}$ through $n_L = \Phi\rho_{\mathrm{air}}s/m_{d,0}$ with s the stoichiometric mass fuel-air ratio.

Property target	Major influence on	*n*-alkanes	*iso*-alkanes	aromatics
Molecular weight	Fuel diffusion	↑	=	↓
H/C ratio	Adiabatic Flame Temperature	↑	=	↓
Threshold Sooting Index	Soot formation	↓↓	↓	↑
Derived Cetane Number	Ignition delay time	↑	↓	↓

Table 5.1: Summary of combustion property targets [160].

5.1.2 Surrogate formulation

In the latest years, several surrogates for aviation fuels have been proposed [78]. In this application, the Jet-A POSF 4658 fuel blend has been chosen as a case study for two reasons. First of all, a surrogate for this fuel was formulated by following a comprehensive approach devised by Dooley et al. [160]. Such methodology is based on matching four combustion property targets of the corresponding real fuel, indicated in Table 5.1. Second, a wide range of experimental data about it are now available to the combustion community, which can be leveraged for benchmarking kinetic models. The surrogate identified by Dooley et al. [160] is made up of four species, representative of the three main classes of hydrocarbons present in a Jet-A fuel:

i. *n*-dodecane ($C_{12}H_{26}$);

ii. iso-octane (C_8H_{18});

iii. 1,3,5-trimethylbenzene (C_9H_{12});

iv. *n*-propylbenzene (C_9H_{12}).

Dooley and coworkers [160] found that the four target properties for a Jet-A POSF 4658 fuel (MW = 142 g/mol; $\frac{H}{C} = 1.96$; TSI = 21.4; DCN = 47.1) were matched by a mixture 40.4/29.5/7.3/22.8 (in molar fractions) of the mentioned species. Such composition was then recommended as second-generation fuel surrogate for POSF 4658.

5.1.3 Kinetic mechanism reduction

Although the gas-phase is simplified in the form of a semi-batch reactor, the use of a detailed mechanism for a two-dimensional parametric study would result in excessive computational times. On the other hand, the hierarchical and modular structure of the POLIMI lumped mechanism provides a solid starting point to obtain a usable model. In its complete form, it describes the pyrolysis, partial

Property	Range
Temperature	500 – 1700 K
Pressure	22.1 atm
Equivalence Ratio	0.25 – 2

Table 5.2: Operating conditions for Jet-A POSF 4658 mechanism reduction.

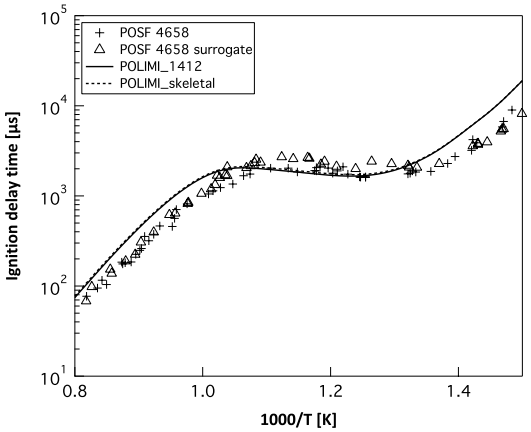

Figure 5.2: Ignition delay times for the stoichiometric POSF 4658 fuel [115] and the 2nd-generation surrogate [160], compared to predictions obtained from the POLIMI complete and skeletal mechanisms (P = 20 atm).

oxidation and combustion of hydrocarbons up to C_{16} and oxygenated fuels, and contains 451 species and 17848 reactions (version 1412 [9]). To make calculations viable, the complete mechanism underwent the reduction approach described in Chapter 4, and implemented in `DoctorSMOKE++`. For each surrogate component, a subset of important species was obtained after sampling the operating range described in Table 5.2 through adiabatic, constant-pressure batch reactors. A target of maximum error on ignition delay time below 10% was set for each species, and a final mechanism of 181 species and 4089 reactions was obtained after merging the subsets of component mechanisms.

As a test bench for original and skeletal mechanism, both of them were utilized to predict the ignition delay time of the fully prevaporized 2nd-generation surrogate. Experimental data were obtained by Dooley et al. [115] for both POSF 4658 and its 2nd-generation surrogate. A constant-volume batch reactor was used to model the autoignition without pressure correction in the whole temperature range. Ignition was calculated as the time when the maximum OH mass fraction occurred, and results are shown in Figure 5.2.

A good agreement is found with experimental data, also considering the experimental uncertainty, reported by Dooley et al. [160], and the idealized conditions

of the 0D constant-volume simulations. These differences are also coherent with those shown by Vasu et al. [57] between shock tube experiments for n-dodecane and the POLIMI mechanism. As a matter of fact, n-dodecane is the most abundant species within the surrogate, as well as the most reactive.

5.1.4 Thermodynamic and transport properties

Fuel descriptions usually contain compounds for which physical properties are not present in the existing literature due to their high number (cfr. Table 2.1). For this reason, a general methodology based on group contribution [168] was adopted. In this way, critical conditions for pressure, temperature and volume, as well as acentric factors, depend on linear contributions from the respective functional groups. Thermodynamic properties like heat capacity, molar specific volume and latent heat of vaporization are then calculated by adding a second-order correlation, accounting for the interactions between the different groups. To account for pressure and temperature dependencies, corrections are applied [169] via:

- Peng-Robinson equation of state for gas and liquid density;
- Thodos correction for latent heat of vaporization;
- Wilke-Lee correction for low pressure vapor diffusion coefficients;
- Lee-Kesler correction the for saturated vapor pressure;
- UNIFAC approach for the estimation of species activity.

Liquid properties were applied to POSF 4658 in idealized systems. Figure 5.3a shows the variation of a sample droplet diameter during evaporation, and the numerical results are compared to the data by Burger et al. [170]. The initial increase in diameter is related to an increase in density, not balanced by a sufficiently high evaporation rate. After that, the diameter decreases following the d^2-law [172]. A good agreement between them can be observed. The same calculations were carried out using the POSF 4658 surrogate. The use of such a mixture slightly underpredicts the total evaporation time. Figure 5.3b shows the distillation curves, compared with experimental data from advanced distillation measurements. The experimental trend is bounded between two asymptotic limits, i.e. flash and fractional distillation curves. Such limits are calculated for both real mixture and surrogate. Again, a reasonable agreement is observed, and for the real fuel the experimental data are bounded by the two asymptotic approaches. A good agree-

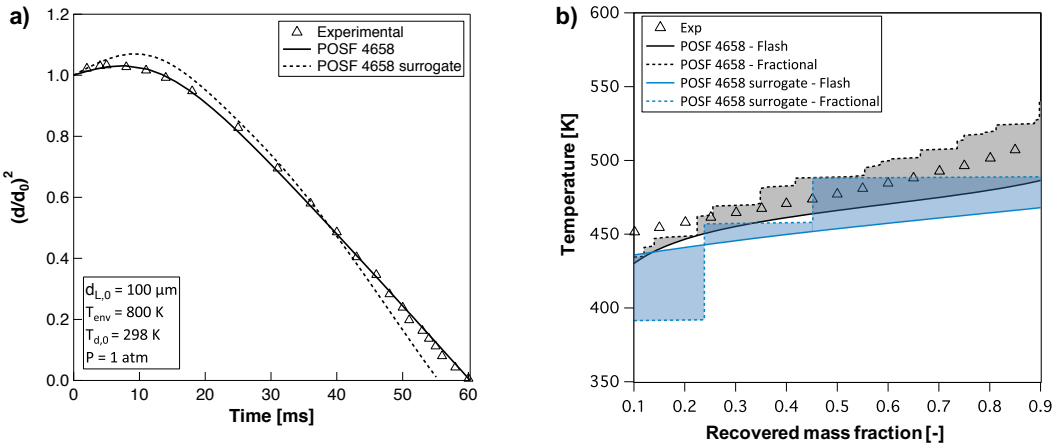

Figure 5.3: a) Comparison between experiments [170] and numerical results for the evaporation of an isolated droplet. b) Comparison between distillation curve measurements [171] and predictions obtained through flash and fractional distillation calculations for POSF 4658 fuel and surrogate.

ment is observed for the surrogate mixture, too, with the flash distillation curve reasonably close to the one obtained from the full fuel description.

5.1.5 Implementation

Numerically, the problem to be faced corresponds to a large system of Differential-Algebraic Equations (DAE). It has been implemented by relying on the `OpenSMOKE++` framework for the liquid-grid discretization and the management of gas-phase kinetics, the `BzzDAE` library [173] for DAE system solution and the `GroupContribution` library [174] for the evaluation of liquid-phase thermodynamic and transport properties.

5.2 Autoignition of multicomponent droplets

In order to understand and delineate the importance of preferential evaporation, the operating conditions of temperature and pressure used in the evaluation of the DCN standard were adopted, i.e. $T_0 = 833$ K and P = 22.1 atm. The ignition delay time was evaluated as a function of initial droplet diameter $d_{L,0}$ (10 – 100 µm) and global equivalence ratio Φ (0.5 – 2), i.e. in conditions usually found in gas turbine applications [175]. As an example of the temporal droplet evolution over time, the evolution of different species within a droplet with $d_{L,0} = 20\ \mu m$ and $\Phi = 1$ is reported in Figure 5.4. A significant difference in composition can be observed between center and interface (Figure 5.4c), which is coherent with the species relative volatility. For the considered surrogate, the least volatile species is n-dodecane, whose evaporation rate is low at the beginning (Figure 5.4c), in

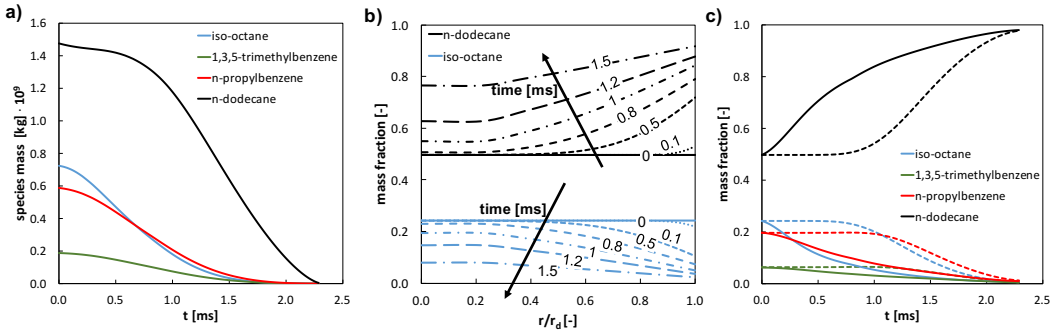

Figure 5.4: Species profiles in a single droplet ($d_{l,0} = 20\,\mu m$, $\Phi = 1$): a) total liquid species mass over time, b) normalized radial profile of n-dodecane and iso-octane over time, c) center (dashed line) vs. interface (continuous line) mass fraction over time.

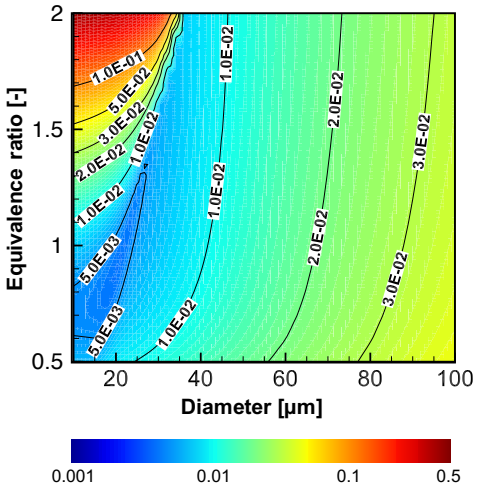

Figure 5.5: Ignition delay times τ_{ign} [s] with finite diffusion for the 2nd-generation surrogate of POSF 4658.

spite of being the most abundant species. The evaporation rate increases only when the mass fraction of n-dodecane approaches the value of unity near the surface. On the other hand, iso-octane, i.e. the most volatile species within the surrogate, evaporates at a significantly higher rate, reaching in the end a lower mass fraction than *n*-propylbenzene, initially present at a lower concentration. As a consequence, the gas-phase composition significantly changes over time: for the considered droplet, *n*-dodecane requires about half of the droplet lifetime to become the prevailing fuel species ($> 80\%$) in the gas phase despite being the controlling species for the ignition initiation.

The complete set of results is shown in the form of a contour map in Figure 5.5, where ignition delay time τ_{ign} is considered as the time at which the temperature in the gas-phase reaches its maximum slope, either before or after droplet complete evaporation. Apparently, the most reactive region is characterized by

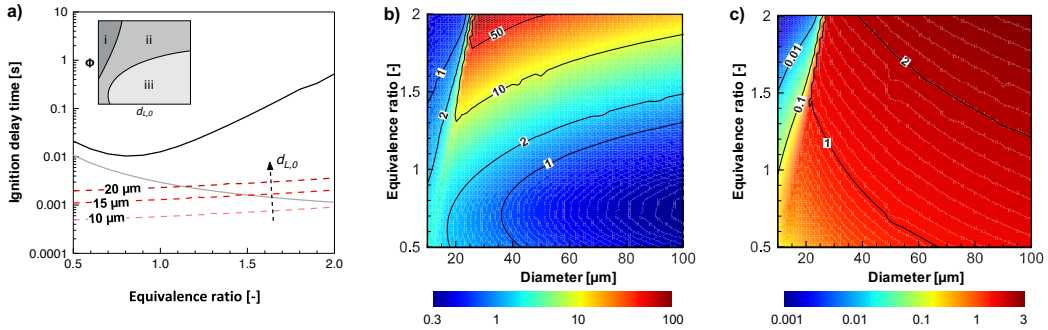

Figure 5.6: a) Ignition delay times of fully prevaporized mixture considering cooling effect (black full line) and without heat transfer by evaporation (gray full line). Evaporation time without combustion (dashed line). b) $(\tau_{evap} + \tau_{pv,ign})/\tau_{ign}$ and c) (τ_{evap}/τ_{ign}) ratios, where τ_{ign} was calculated with a constant-fuel composition (zero-diffusivity model).

small droplet diameters and low equivalence ratios; a minimum ignition delay is observed around $d_{L,0} = 20\,\mu m$ and $\Phi = 0.8$. Such minimum is the result of the non-monotonic behavior of both parameters under investigation. Above all, such trends are qualitatively similar to the results observed by Moriue et al. [155] for the autoignition of isolated droplets of *n*-heptane, in simulations where both liquid and gas phase had been spatially discretized. This can be considered as an indication that the model proposed here is able to reproduce essential physical mechanisms to describe the competition between evaporation and ignition time scales.

Indeed, in the present model the droplet ignition delay is controlled by two main parameters: the availability of fuel and the gas temperature. Both are related to the evaporation process and thus influenced by the droplet size and number density (or equivalence ratio). The classical literature assumption [176] considers the droplet cloud ignition delay as the result of two serial processes, i.e. evaporation and gas-phase autoignition. In this way the total ignition time can be approximated as $\tau_{ign} = \tau_{evap} + \tau_{pv,ign}$, respectively the evaporation and autoignition time of the prevaporized mixture. For small droplet diameters, where $\tau_{evap} \ll \tau_{pv,ign}$, this assumption holds and τ_{ign} is found to mainly depend on equivalence ratio (region (i) in Figure 5.6a): for pre-vaporized mixtures, the heat extracted from the gas phase to achieve evaporation is directly proportional to the equivalence ratio. Because of the exponential dependance of $\tau_{pv,ign}$ with temperature (Figure 5.2), a comparable exponential increase of the ignition delay time with Φ is observed. This effect is shown in Figure 5.6a, where the difference between prevaporized ignition delay with and without heat losses by evaporation progressively increases from a factor two to two orders of magnitude with increasing Φ. On the other hand, for large initial droplet diameters ($d_{l,0} > 40\,\mu m$), τ_{ign} is limited

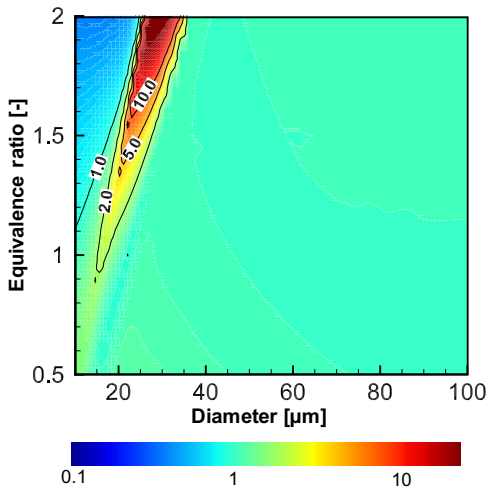

Figure 5.7: Map of the ratio between τ_{ign}, as calculated via finite diffusion model (Figure 5.5) and zero-diffusivity model.

by fuel availability: with increasing equivalence ratio the ignition delay monotonically decreases as a result of the higher total evaporation rate. In this case, τ_{ign} can no longer be represented by the sum of τ_{evap} and $\tau_{pv,ign}$. At low equivalence ratios (region (iii) in Figure 5.6a), its value is higher because of the low reactivity of the initially lean mixture. Instead, this trend is opposite at higher equivalence ratios, where the higher fuel availability allows a faster ignition. Figure 5.6b shows that at the boundary between regions (i) and (ii) ignition is even 100 times faster than the sum of τ_{evap} and $\tau_{pv,ign}$. In this case, the balance between τ_{evap} and τ_{ign} (Figure 5.6c) makes this region more sensitive to preferential evaporation, determining the composition of the evaporating mixture, and then changing τ_{ign}. In order to further understand the importance of this composition, a comparison with the results provided by a zero-diffusivity model is carried out. Because of the assumed zero-diffusivity in the liquid phase, the composition of the gaseous phase remains constant throughout evaporation. In numerical terms, this was approximated by multiplying all diffusion coefficients by a factor 0.001. The ratio between the autoignition times for the case with finite diffusion and the zero-diffusivity model is presented in Figure 5.7. As predicted from the previous analysis, no significant difference are observed for large diameters. On the other hand, important differences appear in the left part of region (ii). Here the zero-diffusivity model significantly underpredicts autoignition time, and the ratio varies by a factor 2 or higher. To better understand the different behavior of the ignition delay time in the zero-diffusion limit, the compositional variation of the surrogate mixture during the ignition is evaluated. This is compared with the ignition delay of the corresponding prevaporized mixture at $T = 833\,K$ and

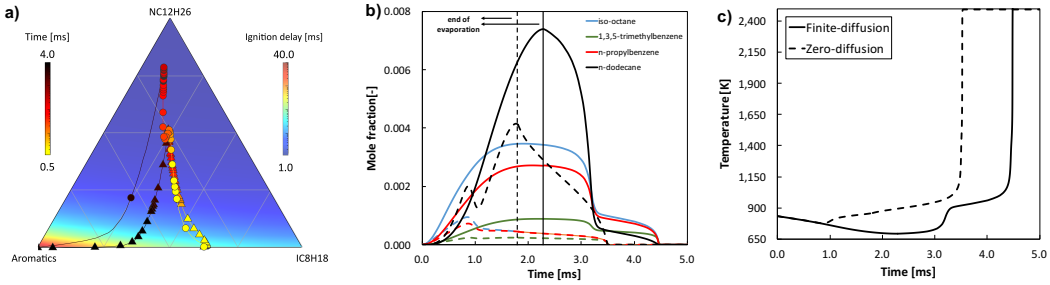

Figure 5.8: Temporal evolution for $d_{L,0} = 20\,\mu$m and $\Phi = 1$ ($P = 22.1$ atm. $T_0 = 833$ K). a) Map of ignition delay time for the ternary prevaporized mixture (color scale), and trajectories of gas-phase composition during evaporation colored by simulation time. Finite- (triangles) vs zero-diffusion (circles) models. b) Species mole fractions and c) temperature in gas-phase, as obtained with finite- (continuous lines) and zero-diffusion models (dashed lines).

P = 22.1 atm. For the sake of clarity, the aromatic (and least abundant) species (1,3,5-trimethylbenzene and *n*-propylbenzene) are combined. Results are shown in Figure 5.8a in the form of a triangular contour map. The vertices and edges of the triangle represent the pure compounds and binary mixtures, respectively. As expectable, *n*-dodecane is found to dominate the ignition behavior for most of the ternary mixtures. The trajectories plotted on top of the gaseous composition space correspond to droplet with $d_{L,0} = 20\,\mu m$ and $\Phi = 1$. The trajectories are colored by the simulation time in order to highlight the time difference between both cases. The zero-diffusion limit is found to induce a significantly faster evaporation and higher content of *n*-dodecane, and therefore results in a faster ignition. The successive rapid consumption of the *n*-dodecane indicates that the ignition is driven by its high reactivity. Figure 5.8b and c show the corresponding time evolution. Apparently, the different diffusion models result in a different reactivity behavior: in the zero-diffusivity limit, the higher concentration of *n*-dodecane causes an earlier low-temperature ignition. Then, the evolution of the n-dodecane mole fraction results from the competition between oxidation and evaporation. The first maximum in *n*-dodecane (0.9 ms) is due to the initiation of the low-temperature ignition. At a second time, since *n*-dodecane exhibits an NTC behavior (cfr. Section 2.3), its reactivity decreases and its concentration increases again because of evaporation. The increase in the gas-phase temperature due to low-temperature ignition accelerates the total evaporation rate, too, resulting in a ~30% droplet faster evaporation. Conversely, this behavior is not observed for the finite-diffusion case, where the evaporation of *n*-dodecane is not high enough to start the low-temperature mechanism during evaporation. Rather, it occurs only after the droplet has fully evaporated, and can be observed from the double inflection point of both temperature and concentration profiles.

5.3 Conclusions

The reliability of multidimensional simulations is always dependant on the number and the quality of assumptions behind them, which are necessary to carry them out in human times. In particular, when dealing with the two-phase combustion of real fuels, two important aspects are, too often, oversimplified:

i. The description of chemical kinetics;

ii. The description of liquid phase and its interaction with gaseous environment.

As concerns the first, it has been already shown that the complex composition of fossil fuels prevents a detailed description of all the species and their mutual interactions. Yet, the focus shift from fuels composition to their physico-chemical behavior, and the formulation of surrogate mixtures, has allowed to tackle this issue and to decrease the problem size. The POSF 4658 case study, formulated through a rigorous approach, based on Combustion Target Properties, shows the success of this strategy. Moreover, the application of the reduction framework implemented into `DoctorSMOKE++` has further simplified such description without losing in accuracy, and a skeletal kinetic mechanism has been obtained and successfully tested against both the real fuel and its surrogate.

As a result, a wider range of fundamental studies on real fuels behavior has been made possible. Deepening the investigation on the second issue, i.e. the assumptions behind the liquid phase, is a viable possibility, and it has been the subject of this Chapter. As a matter of fact, the use of a standardized "property-targeted" framework like the one proposed by Dooley et al. [160] for POSF 4658 formulation requires the right attention downstream, when the same surrogate is utilized in the targeted application, in non-standard conditions. In this direction, the effect of multicomponent diffusion and preferential evaporation, which are currently neglected by most two-phase solvers, was here investigated. The use of the mentioned skeletal mechanism allowed to use sufficient detail for the relevant physical phenomena characterizing liquid phase, like (i) multicomponent diffusion, described through a Stefan-Maxwell approach and (ii) thermodynamic equilibrium at the interface, for which the Peng-Robinson equation of state was adopted. Using the obtained model, an extended range of operating conditions, spanning over droplet diameter and equivalence ratio, at DCN testing conditions (T = 833 K, P = 22.1 atm) was investigated for the POSF 4658 fuel. It was found that the competition between the fuel evaporation and the subsequent cooling of the gaseous mixture determines the ignition delay time, whose behavior as a function of global equivalence ratio is non-monotonic for small diameters. Moreover, it was

found out that droplet ignition cannot be considered as the simple summation of droplet evaporation time and the ignition time of the prevaporized mixture. The analysis of the deviation from the ideal behavior allowed to identify three regions:

- A region where ignition is driven by chemical kinetics: $\tau_{ign} \approx (\tau_{evap} + \tau_{pv,ign})$ and $\tau_{evap} \ll \tau_{pv,ign}$;
- A region where ignition is controlled by evaporation: $\tau_{ign} > (\tau_{evap} + \tau_{pv,ign})$ and $\tau_{evap} \gg \tau_{pv,ign}$;
- A region where two-phase ignition significantly deviates from the ideal behavior, and droplet evaporation and ignition time scales become comparable. At these conditions, the sensitivity to preferential evaporation is most pronounced. A comparison with the autoignition map obtained with a zero-diffusivity model emphasizes significant discrepancies in ignition delay times compared to a finite-diffusion model.

Therefore, the indication that multicomponent evaporation and liquid diffusion may actually have a significant effect on ignition delay time in a range of diameters and equivalence ratios, relevant for gas turbine application, emerged from this analysis. Further investigation can be carried out through in different directions. Starting from the results obtained so far, physical variables excluded from this study can be incorporated in this model. Although adding non-negligible computational complexity, the influence of gas-phase transport or slip velocity on the ignition delay time can be useful extensions of this analysis, and compounding effects of different physical processes relevant to multicomponent spray combustion can be evaluated. Finally, the use of this level of detail may turn out of primary importance when applied to surrogates of nonconventional jet fuels, where the presence of compounds like alcohols and, more in general, oxygenated species can introduce significant non-idealities in both the diffusion and equilibrium model. The availability of the UNIFAC model for activity coefficients is able to account for such behavior in both cases, and might highlight even more significant differences with respect to the state-of-the-art approaches, where mixture ideality is one of the basic assumptions.

CHAPTER 6

Soot formation from isolated fuel droplets

NOWADAYS liquid fuels occupy the largest share in the transportation market, and their dominant role is expected to be retained for the decades to come [177]. Their favorable energy density, large availability and the consolidated distribution network make them the preferred energy vector for ICEs. Yet, the tighter and tighter emission rules [5, 178] are pushing towards changes to fuels and propellants [179] in such a way to make them compliant with the current standards. To this purpose, having reliable kinetic models able to describe the formation paths of the different pollutants and their coupling with the pyrolysis and oxidation routes of the different hydrocarbons is a necessary step. From a numerical standpoint, the verification of such mechanisms cannot be directly carried out on the models of combustion engines, because of their computational weight, as well as the coupling of chemistry with a number of separate phenomena (heat transfer, turbulence closure, etc.), which would make mechanism troubleshooting an impossible task.

In the case of soot, the problem is further complicated by the intrinsic unsteadiness of the related formation and destruction processes [180, 181]. In spite of its complexity, the interest on such topic is particularly high, because of its multiple negative impacts on human health [182], environment [183] and combustion effi-

ciency. Yet, the overlapping and mutual interaction between the different steps characterizing its dynamic behavior [184] prevent a complete chemistry assessment in the simplest 0-dimensional reactors, as it happens instead in the case of pyrolysis and oxidation paths. As a matter of fact, the presence of atomized fuel in diesel and gas turbine engines and its progressive evaporation results in spatial composition gradients, thus creating favorable conditions for its formation and growth. Therefore, soot formation in such systems is far higher than gas-phase only devices like gasoline engines.

The simplest system able to represent the fundamental processes behind heterogeneous fuel combustion is represented by an isolated droplet in microgravity conditions, fixed in a gas-phase environment. In such idealized conditions, it represents the simplest heterogeneous 1-dimensional system, thanks to the spherical symmetry, where the transport induced by fuel evaporation is coupled to combustion chemistry. In spite of its ideality, several processes actually taking place in real devices must be properly considered, like gas and soot radiation, heterogeneous properties and so on. In this way, a deeper insight into the flame evolution, droplet evaporation and soot formation can be gained. The importance of such idealized conditions is also mirrored by the large experimental activity, which has focused on such idealized conditions and carried out reduced-gravity combustion experiments, either in drop towers [185] or in the outer space [186].

In kinetic terms, representing soot is not straightforward. There are two main differences with respect to the other classes of pollutants: (i) the solid phase and (ii) a heterogeneous distribution of particle size and morphology. This prevents from a traditional approach to kinetic modeling, and requires a proper methodology to couple gas-phase chemistry to solid-phase formation and growth. Several approaches were proposed in this direction, e.g. method of moments [180], Monte Carlo methods [151], polymerization models [187] or discrete sectional approaches [188]. The resulting complexity makes the use of the overall model computationally expensive, such that even 1D simulations like isolated droplets can be prohibitive.

In this context, the reduction framework developed in this Thesis finds a direct application. In Section 4.6 it has been shown that an STSA approach has the capability to perform optimal mechanism reduction by focusing on the dynamics of formation on specific species. Although soot cannot be considered as a species on its own, such technique can be conveniently adapted to focus on *ad hoc* property targets, and obtaining a mechanism which retains sufficient accuracy on them. Starting from the description of the gas-phase kinetic model and the coupling

with solid phase (Section 6.1), skeletal reduction is then performed on the global mechanism, and the performance of the obtained scheme is verified against the original one and experimental data in a series of 1- and multi-dimensional case studies. The isolated droplet model is then briefly recalled in Section 6.2. This is applied in Section 6.3, where a comprehensive investigation of the *n*-alkane droplets, for which a wide range of experimental data are available, is carried out and then discussed. Indications involving future developments of this activity are then provided in the conclusions.

6.1 Kinetic model

The hierarchical and modular approach behind the POLIMI mechanism [9] allows to easily isolate the gas-phase mechanism of interest for the current purposes. Specifically, the high-temperature only mechanism including PRF, PAH and real fuels (version 1412) includes 200 species and 6907 reactions. Similarly, the low- and high-temperature mechanism for the same species contains 352 species and 13264 reactions. Thermodynamic properties were obtained from databases [189], or estimated through group additivity method [190] where not available.

The coupling with gas-phase is carried out through the discrete sectional approach recently developed by Saggese and coworkers [188]. Such a methodology represents the aerosol distribution through a 2-dimensional discretization into pseudo-species, defined as BINs, representing (i.e. lumping) a class of particles according to their size and composition (in terms of H/C ratio). According to their size, BINs are divided into heavy PAHs (MW $\leq$ 2000), soot particles (2000 $<$ MW $\leq$ 500000), and soot aggregates (MW $>$ 500000). Soot particles differ from aggregates because of their assumed spherical shape; on the contrary, aggregates are considered as mass fractals, having a fractal dimension equal to 1.8 [191]. A detailed description of the soot model is provided in [188, 192]. For the purposes of this Thesis, it is important to highlight that, like the gas-phase model, it is conceived following a reaction-class approach (cfr. Section 2.1), involving both gas-phase species and solid-phase pseudo-species:

- Hydrogen-abstraction-carbon-addition (HACA) mechanism;
- Soot inception;
- Surface growth;
- Dehydrogenation;
- Coalescence/aggregation;

- Oxidation;

The reaction rates of the different classes are derived from comparable, gas-phase reactions, already present in the gas-phase model. One advantage of such a description is the possibility of describing the coupled system in a pseudo-homogeneous way, and a CHEMKIN-compatible structure of kinetic input can be retained. The complete mechanism is made up of 297 species and 16797 reactions considering only the high-temperature, and 426 species and 20145 reactions for the low- and high-temperature reaction paths.

6.1.1 Skeletal reduction of the coupled mechanism

Although getting a benefit from the lumped formulation of both gas- and solid-phase species, the size of the final mechanisms is still high for their large-scale employment in the desired application. The STSA methodology implemented in `DoctorSMOKE++` was exploited to carry out substantial reduction. For the specific case of soot dynamics, though, it required a proper adaptation.

First of all, unlike the NO_x case, it is not possible to address sensitivity analysis towards a specific species, because every BIN represents only a portion of the continuous particle distribution constituting soot. An alternative approach was then devised. Three macroscopic properties are usually evaluated from the soot aerosol: (i) volume fraction f_v, (ii) number density N_d and (iii) particle size distribution function (PSDF). They are not independent each other, since N_d can be obtained through integration of PSDF and f_v can be obtained through combination of mass fractions and particle density. Therefore, considering isothermal 0D reactors as described in Section 4.6.1, two targets are selected to constrain sensitivity analysis and consequent species removal:

- Soot mass fraction profile over time in a 0D reactor;
- Soot PSDF, chosen at the time where soot mass fraction is maximum.

Following the usual procedure, by evaluating ε_D (4.19) and ε_S (4.20) for each of the two, the error following the removal of marginal species can be estimated.

The second aspect to take into account for a proper reduction is the competition between the dynamics of formation and destruction of soot particles. Indeed, their formation and growth occurs in rich conditions, but their destruction is due to oxidation, i.e. in fuel/air ratios close to stoichiometric. In multidimensional systems, this happens because of gas and particle transport. On the other hand, this is impossible to observe in 0D reactors, like those used for mechanism reduction. Thus, the use of a single reacting system to collect reaction states would

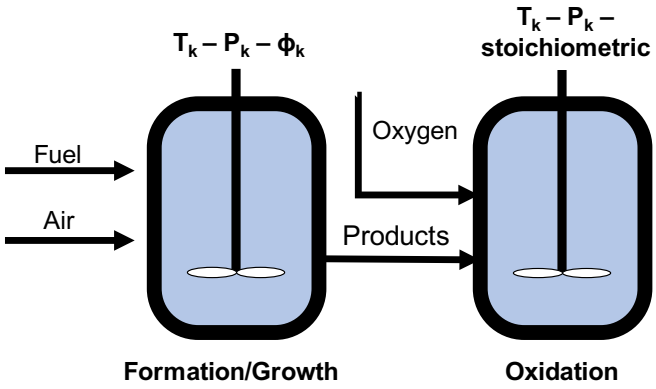

Figure 6.1: Double-batch configuration implemented in `DoctorSMOKE++` for the reduction of soot mechanism.

			Original mech		Ignition mech		Soot mech	
Mechanism	ε_D	ε_S	Species	Reactions	Species	Reactions	Species	Reactions
HT	0.15	0.06	297	16797	58	734	195	8135
LT+HT			426	20145	92	1145	262	11865

Table 6.1: Threshold values and sizes of the two soot mechanisms obtained via modified STSA.

not be a guarantee of accuracy on oxidation pathways. To keep into account this behavior, too, the outlet products coming from the first reactor enter a second one with the same operating conditions, in terms of temperature and pressure, and oxygen is fed in parallel at stoichiometric conditions. Dynamics of oxidation is built through mass fraction profile, and the error following marginal species removal is calculated again via ε_D and ε_S. Figure 6.1 outlines the described system.

Overall, six error indices (two per each of the three curves) are obtained. Their combination is carried out after summing up all the normalized values, obtained according to Eqs. 4.22 and 4.23. Following STSA in this modified form, and after fixing a 10% maximum error on ignition delay time for the identification of the core species, the mechanisms listed in Table 6.1 were obtained for soot formation from n-heptane combustion. In the case of the high-temperature mechanism, about 100 species could be cut with a negligible accuracy. It must be highlighted that, if the original mechanism contains 100 BIN species (50 molecules + 50 radicals), in its skeletal version 73 of them were retained (45 molecules + 28 radicals). Most of the removed ones are then gas-phase compounds. Moreover, in absolute terms skeletal reduction is less effective when performed to a discrete sectional model, if compared to the basic approach (Section 4.2). Indeed, considering that the sectional model is conceived in such a way that every BIN has a double mass, compared to the previous one, the removal of an intermediate section would break

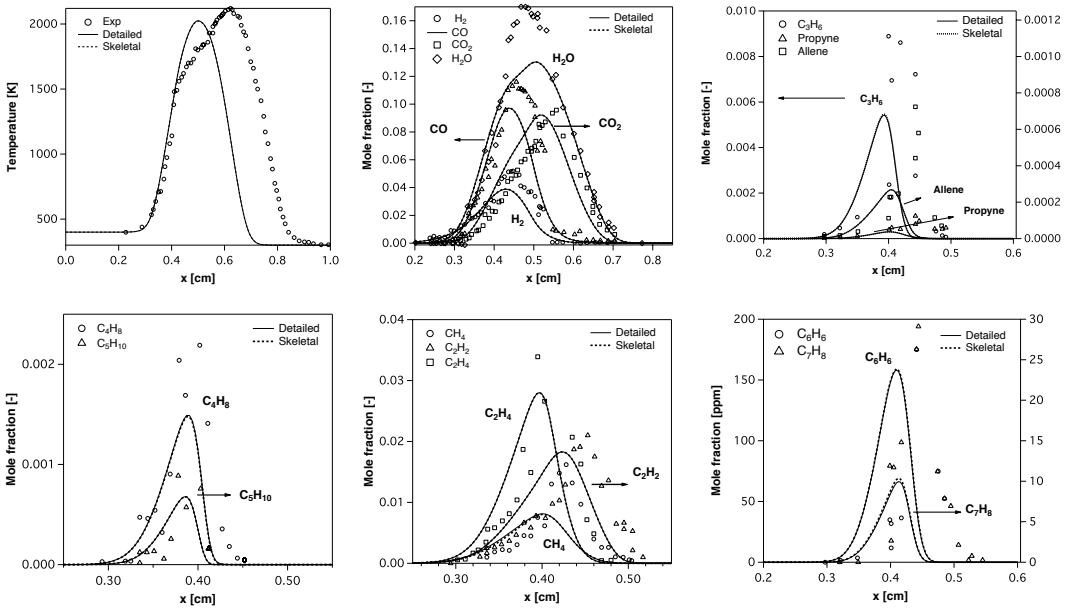

Figure 6.2: Experimental [193] and numerical profiles of n-heptane/air partially premixed flame. Strain rate = 150 s^{-1}; $\Phi = 4.1$; Nozzle separation = 1 cm.

the growth chain of particles through coalescence/aggregation, such that particles can only grow via coalescence with smaller ones, having a much lower mass.

6.1.2 Mechanism benchmark

A comprehensive verification of the POLIMI soot model can be found in the reference work by Saggese et al. [192]. Hereafter, the high-temperature skeletal mechanism is benchmarked against it and experimental data.

PAH formation in counterflow laminar flames. A preliminary test has involved the formation of soot precursors in 1-dimensional flames, necessary for the formation of the first BINs. n-heptane partially premixed counterflow flames were experimentally studied by Berta et al. [193], and detailed measurements of hydrocarbon species up to benzene and toluene were carried out in rich conditions, with variable strain rates and equivalence ratios. Figure 6.2 shows the comparison between detailed and skeletal mechanism. As expected, in all the cases the numerical profiles are overlapped. The agreement with experimental data is good for both major species and intermediate compounds. Most significant deviations are observed for toluene, whose peak is underestimated by a factor 2-3. The location of the temperature peak is also misestimated. This behavior had been observed by the authors themselves within their own numerical predictions in all their case studies, and had been attributed to the catalytic effect of the thermocouple.

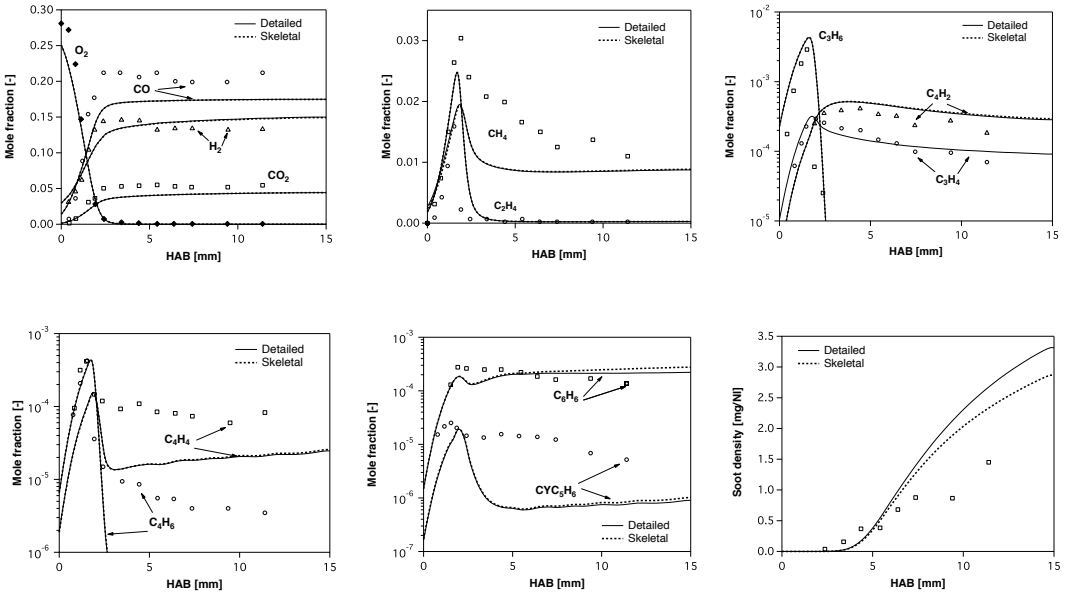

Figure 6.3: Experimental [194] and numerical profiles of n-heptane/air laminar premixed flame. $v_{in} = 4\,cm/s$. C/O = 0.70.

Soot formation in premixed laminar flames. To date, the formation of soot in counterflow flames from real fuels has not been characterized yet. Instead, few experimental works have measured PAH and soot in premixed laminar flames. D'Anna and coworkers [194] measured combustion products in slightly sooting (C/O = 0.70) and heavily sooting (C/O = 0.80) conditions, i.e. major species, smaller intermediate alkanes, condensed species (PAH) and soot. Both flames were simulated through original and skeletal model, and respective results are shown in Figure 6.3 for the slightly sooting flame, and Figure 6.4 for the heavily sooting one. The temperature profile was taken from experimental measurements and energy balance was not solved: this is a standard procedure, because burner heat losses are strongly dependant on the experimental devices, and the 1D flame cannot be assumed as adiabatic. A very good agreement can be observed for major species, where the original and skeletal mechanism are overlapped. A similar behavior is observed for benzene, too: in such case, kinetic mechanisms can reproduce experimental trends very well, and although the numerical profiles are not completely overlapped, their difference is reasonable at the outlet, being around 20% in both cases (note: y-axis is in logarithmic units).

The most important outcome from the two case studies is the soot density profile (bottom right of Figure 6.3 and 6.4). The deviations between detailed and skeletal mechanism are of the order of 15% at the burner outlet, which is an appreciable agreement, in line with the accuracy targets of the reduction procedure. Moreover, the very good agreement with experimental data must be pointed out.

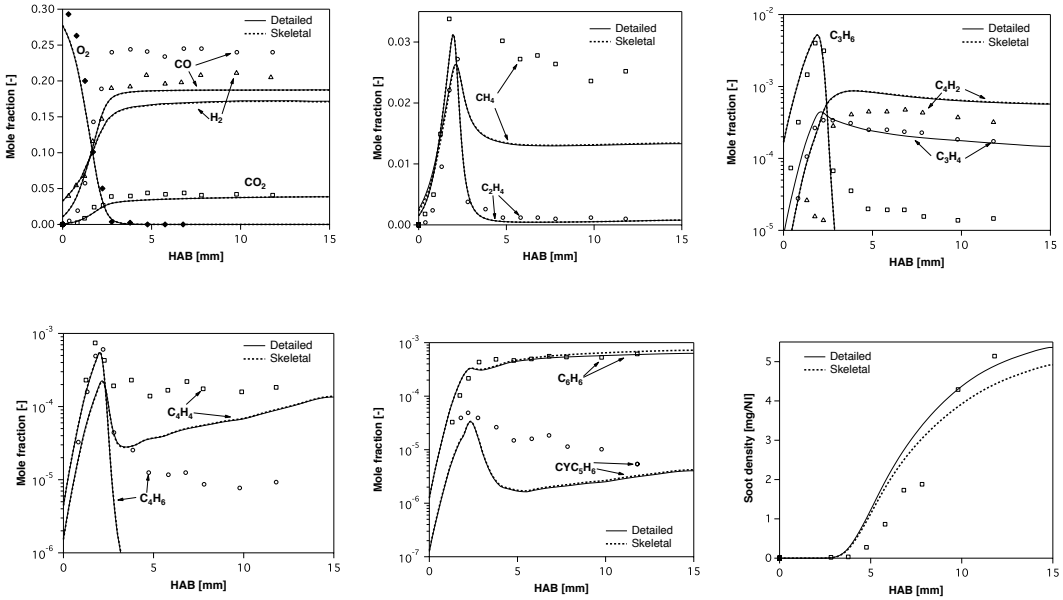

Figure 6.4: Experimental [194] and numerical profiles of n-heptane/air laminar premixed flame. $v_{in} = 4\,cm/s$. C/O = 0.80.

Also considering the experimental uncertainty behind soot measurements [184], in premixed conditions the quality of the results for n-heptane combustion is comparable to what had previously been obtained for ethylene [188, 192].

Soot formation in coflow diffusion flames. Because of particle transport outside the reaction zone, in diffusion flames all the reaction steps mentioned in Section 6.1 coexist, including oxidation. Moreover, in this kind of flames the amount of produced soot is generally higher, because the locally rich composition on the fuel side provides favorable kinetic conditions. The capability of predicting sooting tendency from real fuels in these applications is then of primary importance. From the experimental side, such tendency has been standardized under the Threshold Sooting Index methodology [195], which is also one of the target properties for surrogate formulation [160]. Recently, the sooting propensity in coflow diffusion flames has been investigated by Kashif et al. [196, 197] for gasoline surrogates and primary reference fuels. In the case of gasoline surrogates, the variation of the relative ratio between the constituting hydrocarbons (n-heptane, iso-octane and toluene) resulted in an approximately linear variation in the amount of produced soot, in terms of fields as well as integral values. In the context of mechanisms verification, the experimental data from the pure n-heptane case are here used as reference.

The axisymmetric coflow burner utilized by Kashif et al. to analyze the sooting propensity of gasoline surrogate was simulated. Here, fuel is injected via the

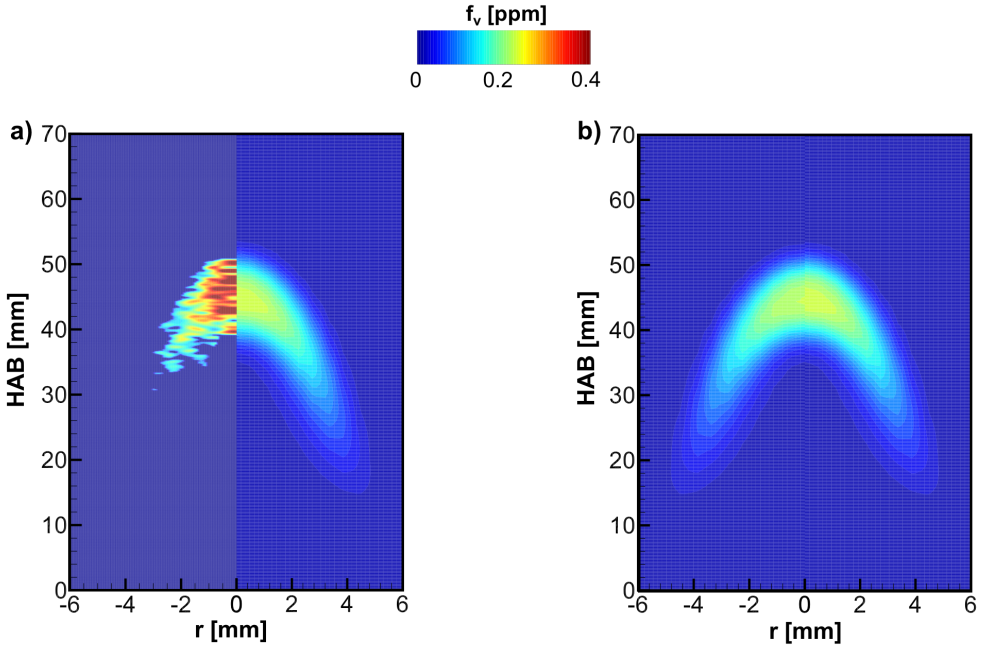

Figure 6.5: Comparison between soot volume fraction fields. a) Experimental [197] (left) vs numerical results, obtained with the original mechanism (right). b) Numerical results, as obtained with skeletal (left) and original (right) mechanisms.

inner vertical axial duct, having a 11 mm diameter of injection, and its exit velocity profile can be assumed as fully developed. Oxidizer is introduced into a concentric 102 mm inner diameter cylinder, and its flow is straightened with a ceramic honeycomb. Fuel mixture consists of a carrier gas (50% methane and 50% nitrogen), and experiments were carried out with two different n-heptane molar fraction (0.0186 and 0.0247). Results are shown here for the richer mixture. In Figure 6.5a, the available experimental field of soot volume fraction is compared to numerical predictions, as obtained via the original model. Such comparison highlights a very similar shape of the profiles. Yet, differently from the premixed case, the volume fraction is underestimated, and in proximity of the axis of symmetry there is a factor 2 of difference. This may be due either to the experimental uncertainty, considering the very low volume fractions involved, or most likely to the oxidation model. As highlighted by Saggese et al. [188], the kinetics of soot oxidation has not been fully investigated yet, and in the present kinetic model the kinetic rates were derived from similar gas-phase reactions.

6.2 Isolated droplet model

The numerical model describing the transient evolution of an isolated droplet was developed with the assumption of spherical simmetry because of microgravity

conditions. It was first implemented through a finite-difference approach by Cuoci and coworkers [122, 123], where both gas- and liquid-phase were discretized and flux equilibrium was supposed at the interface. Here, its main features are recalled, and aspects of higher relevance for this context are described in detail.

Liquid phase is discretized as in Eqs. 5.1, 5.2 and 5.3. In this case, no models for liquid internal diffusion are required, because of the homogeneous droplet composition in the cases considered. Interface flux continuity of heat and species are imposed. Considering the operating conditions of the case studies here investigated, i.e. low pressures and ideal fuels (n-alkanes), the use of the Raoult's law for system closure and thermodynamical equilibrium can be used without significant mistakes [122]. Unlike the approach adopted in Section 5.1, gas phase is here radially discretized:

$$\rho_G \left(\frac{\partial Y_{G,i}}{\partial t} + v_G \frac{\partial Y_{G,i}}{\partial r} \right) = - \frac{1}{r^2} \frac{\partial}{\partial r} \left(r^2 \left(j_G + j_{Th} + j_S \right) \right) + \dot{\omega}_{G,i}, \tag{6.1}$$

$$\begin{aligned} \rho_G C_G \left(\frac{\partial T_G}{\partial t} + v_G \frac{\partial T_G}{\partial r} \right) =& \frac{1}{r^2} \frac{\partial}{\partial r} \left(r^2 k_G \frac{\partial T_G}{\partial r} \right) \\ & - \sum_i j_{G,i} C_{G,i} \frac{\partial T_G}{\partial r} - \sum_{i=1}^{N_C} \omega_{G,i} H_{R,i} - \nabla q_R, \end{aligned} \tag{6.2}$$

$$\frac{\partial \rho_G}{\partial t} + \frac{1}{r^2} \frac{\partial}{\partial r} \left(r^2 \rho_G v_G \right) = 0, \tag{6.3}$$

where the subscript G denotes the gas-phase. j_G is the gas-phase diffusion flux, evaluated through the Fick's law; j_S is the flux related to the Soret effect, while j_{Th} is the flux due to thermophoretic effect [198], which involves solid phase particles and is evaluated, in spherical coordinates, as:

$$j_{Th} = - \frac{3}{4 \left(1 + \frac{\pi \alpha}{8} \right)} \frac{\mu}{T} \frac{dT}{dr} = - K_{Th} \frac{\mu}{T} \frac{dT}{dr} \tag{6.4}$$

where μ is the dynamic viscosity and α is the accommodation factor, which is commonly accepted as equal to 0.9 [199], thus leading to a value of K_{Th} equal to ~0.554. $\omega_{G,i}$ is the reaction source term of the i-th species, $\omega_{G,i} = \sum_{j=1}^{N_R} \nu_{ij} r_j$, with r_j the rate of the j-th reaction. $H_{R,i}$ is the enthalpy of formation of the i-th species, and finally ∇q_R is the radiative heat flux. P-1 radiation model [200] is used, and the Planck absorption coefficient for soot is evaluated following Smooke et al. [201]. Boundary conditions at the droplet center are defined like in Section 5.1. At the outer boundary, i.e. around 80-100 times the droplet size, Dirichlet conditions are imposed for species and temperature.

At initial conditions, the droplet is numerically ignited by simulating a "numerical spark": for a limited amount of time, a temperature profile peaking at ~2000 K is imposed near the droplet interface. Although in experimental devices the spark occurs at one side of the droplet and may in principle compromise the symmetrical characteristics, this effect is neglected in the present model, as already done in previous cases [154].

6.3 Droplet combustion of sooting fuels

Based on the experimental activity carried out in the latest two decades, the combustion of *n*-alkane droplets has been investigated in a wide range of conditions, in terms of diameters and starting fuel. Where not further specified, the skeletal mechanism has been employed, in order to perform simulations in affordable times, i.e. O(hours). An adaptive grid, made up of 410 points, has been used, with four different stretching factors: higher refinement has been set in the region where the soot and flame shells are expectably located (from the available experimental data), while a more coarse spacing has been set in the far field.

6.3.1 Flame structure and standoff ratio

From the experimental side, understanding the flame evolution over time in sooting droplets is a very challenging task. The formation of soot around them prevents any invasive measurement on the inner part, since the thermocouple would be coated with soot, thus compromising the accuracy of results. Insights can instead be provided on the outer flame profile, where the use of proper coating of thermocouples to avoid catalytic effect can produce reliable data. The transient flame structure was studied by Mikami et al. [202], who used hooked thermocouples, concentric with droplets shape, to measure the outer temperature profile at different time steps. For the case of interest here, i.e. *n*-heptane at ambient pressure, results were numerically reproduced through the isolated droplet model. Figure 6.6 compares model output with experimental data. Results show that the model is able to replicate the shape of the radial temperature profile. Nevertheless, an overestimation of the outer part of the temperature profile can be observed. This is also apparent from the evolution of flame temperature over time. Around 120 K of difference are present: such deviation is partly explained by the need of accounting for radiative heat loss from the thermocouple [203]. As recognized by Mikami and coworkers, in the peak region the actual temperature is at least 80 K higher than thermocouple output. A second possible reason to explain the residual deviation is related to soot itself. Radiative heat transfer effects due to the

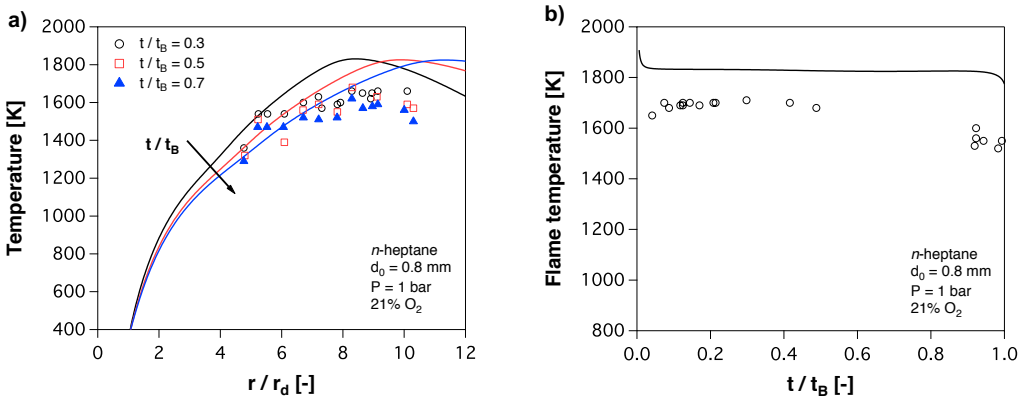

Figure 6.6: Flame evolution over time in a n-heptane droplet ($d_0 = 0.80\,mm$): experimental data vs numerical predictions. a) Temperature profile at different time steps. b) Flame temperature over time. t_B = total burning time of the droplet.

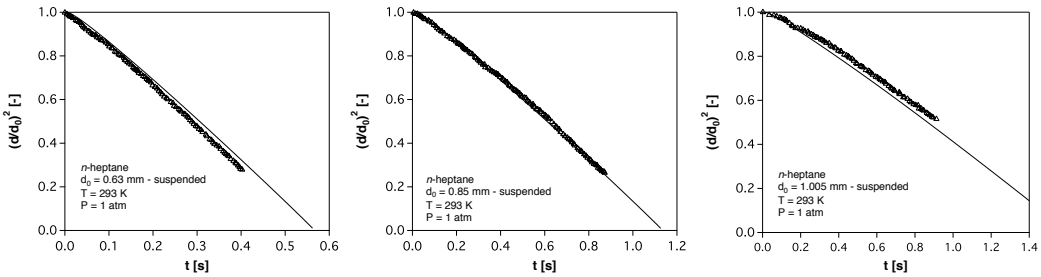

Figure 6.7: Diameter profiles over time during the combustion of three isolated droplets. Experimental data from [185].

presence of soot are indeed significant [204], and also explain the slow decrease of flame temperature over time starting from $t/t_B \approx 0.4$. The decrease in flame temperature predicted by the numerical model is instead smaller. Therefore, if soot formation is underestimated by the model, this affects negatively the steepness of the temperature profile, as well as the absolute deviation with experimental data. Unfortunately, no data on soot formation were collected my Mikami and coworkers, but this aspect is further deepened in Section 6.3.2.

Figure 6.6a also shows that the unsteady burning conditions result in the flame front progressively moving away from the droplet surface. In order to be observed, such behavior needs a detailed description, and simplified analyses considering quasi-steady state conditions, or constant thermal and physical properties might provide approximate predictions. Jackson et al. [185] studied the flame evolution with different starting diameters ($d_0 \leq 1\,mm$) and different fuels (n-heptane and 1-chloro-octane), in order to check the deviations from the quasi-steady state process. In the case of n-heptane, the numerical simulations confirm a constant burning rate over time, except for the initial heating transient. Figure 6.7 shows

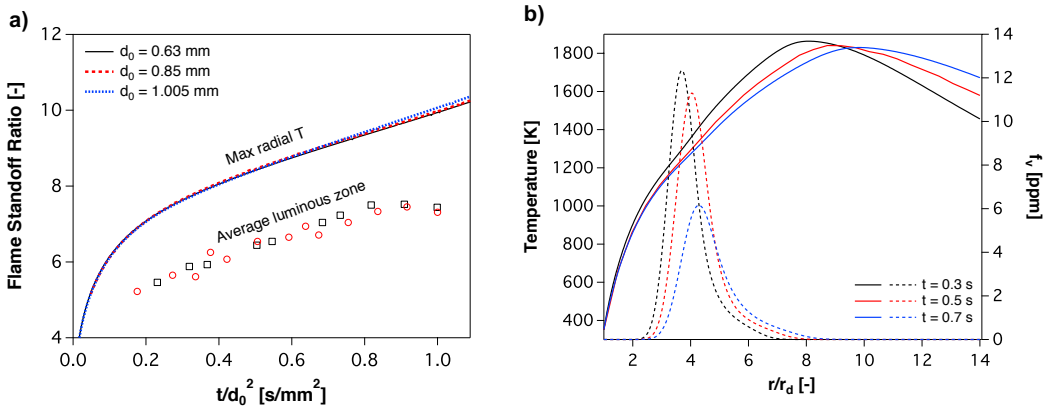

Figure 6.8: a) Experimental [185] vs predicted FSR over burning time. Experimental data not available for $d = 1.005\,mm$. b) Correspondence between predicted maximum temperature (continuous lines) and soot volume fraction profile (dashed lines). $d_0 = 0.855\,mm$.

the good agreement with the experiments. Conversely, the position of the flame front with respect to the droplet itself cannot be considered stationary. Figure 6.8a shows the evolution of the Flame Standoff Ratio (FSR), i.e. the relative position of the flame front with respect to the droplet, normalized by its instantaneous diameter. Numerical predictions show a linear increase of FSR over time, which apparently scale with d_0^2 since the three curves are almost overlapped.

A constant and significant offset can be observed between model and measurements. This is most likely due to the different procedure for measuring the flame front. The experimental methodology adopted by Jackson and Avedisian [185] consisted in calculating the average of the yellow luminous zone around the droplet; numerically, FSR is usually evaluated as the location where the maximum radial temperature is attained, or equivalently the peak in OH formation. Figure 6.8b shows the difference between the two metrics in a sample droplet. The yellow color is indeed mostly due to radiation from soot, occurring as long as it is in high temperature regions. There is negligible soot around the temperature peak because of the thermophoretic effect, thus the experimental procedure finds a lower FSR profile. As a point of comparison, in the more recent work by Liu et al. [205] FSR is evaluated as the outer boundary of the blue zone (i.e. soot-free) enclosing the yellow core, and in that case for a droplet of comparable size ($d_0 = 0.55 - 0.60\,mm$) FSR profile is shifted upwards, and more in line with the results obtained here with the numerical criterion.

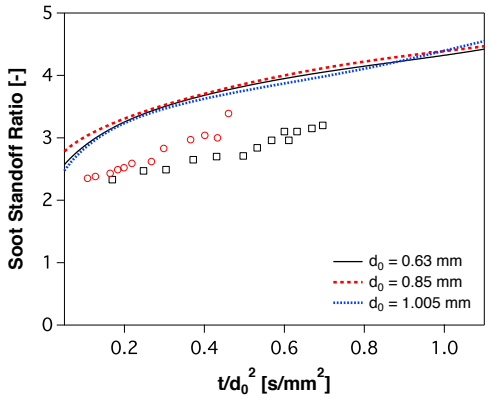

Figure 6.9: SSR evolution during the combustion of three isolated droplets. Experimental data from [185].

6.3.2 Soot characteristics

Unsteady effects are of critical importance when soot is concerned. It has been already mentioned that its presence in significant amounts might affect droplet combustion because of its radiative power, thus coupling gas and aerosol phase and decreasing burning efficiency. In microgravity conditions several experiments have analyzed in detail its dynamics of formation; one major peculiarity has emerged, i.e. significantly higher amounts of soot formation, of the order of tens of ppm, even by not heavily sooting fuels, like *n*-heptane, whose formation amounts are usually smaller than 1 ppm (cfr. Figures 6.3 and 6.4). In addition to the soot mass and distribution, the characterization of its soot evolution is done in terms of relative position of the soot layer, i.e. the Soot Standoff Ratio (SSR). Similarly to what done for FSR, Jackson and Avedisian [185] have measured SSR throughout direct photographs observations. In numerical terms, this is done by finding the radial coordinate where volume fraction f_v is maximum. Figure 6.9 compares experimental and predicted profiles: in this case, too, they follow parallel trends, less steep than FSR, with the model overestimating SSR of about one diameter.

The position of SSR is strongly depending on the balance between the three different velocity acting on the soot particles:

i. The convective velocity due to evaporation, known as Stefan flow. Because of the constant-pressure hypothesis and the radial simmetry, it is obtained by the continuity equation:

$$v_{\text{Stefan}} = \frac{1}{\rho_G} \frac{\frac{dm}{dt}}{4\pi r^2} \tag{6.5}$$

ii. The diffusiophoretic velocity due to composition gradients. For each i-*th*

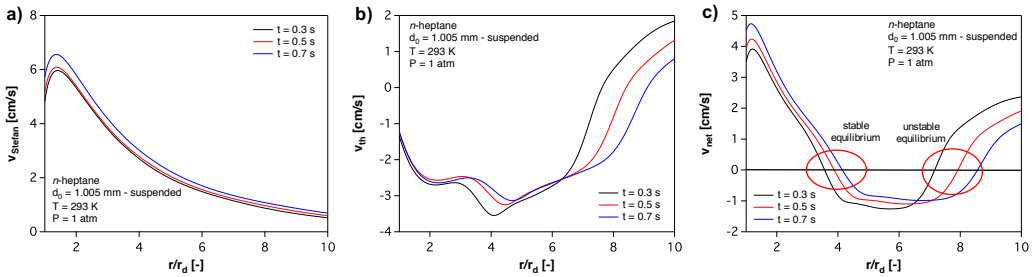

Figure 6.10: Predicted velocity profiles at three time steps for the droplet with $d_0 = 1.005\,mm$. a) Stefan velocity; b) Thermophoretic velocity; c) Net velocity

species, it is calculated according to Fick's first law:

$$v_{dp} = -D_{mix,i}\frac{dY_i}{dr} \tag{6.6}$$

where $D_{mix,i}$ is the diffusion coefficient of the i-th species into the gaseous mixture. Its value is evaluated as [206]:

$$D_{mix,i} = \frac{\sum_{j\neq i}^{N} X_j MW_j}{\overline{MW}\sum_{j\neq i}^{N} X_j D_{ij}} \tag{6.7}$$

where $\overline{MW}$ is the average molecular weight, N is the total number of species, D_{ij} is the binary diffusion coefficient of the i-th species into j, evaluated according the kinetic theory of gases [207]. For soot particles, such value is extrapolated according to their molecular weight, since the kinetic theory of gases is not applicable.

iii. Thermophoretic velocity, directly obtained from Eq. 6.4:

$$v_{\mathrm{Th}} = \frac{j_{Th}}{\rho_G} = -K_{Th}\frac{\mu}{\rho_G T}\frac{dT}{dr} \tag{6.8}$$

Considering that (ii) is usually negligible in this case if compared to the other two contributions [208], the balance between (i) and (iii), acting in opposite directions, determines the location of the equilibrium point inside the shell, as well as the residence times of soot in the fuel-rich region. Because of the temperature gradients characterizing radial profiles (Figure 6.6), a stronger thermophoretic effect would push the soot shell towards the droplet, and then bring to a lower SSR profile. Also, a stronger thermophoretic effect would allow a longer permanence to soot within the rich region, thus fostering its accumulation. Figure 6.10 shows the predicted velocity profiles at three different time steps. The competition between (i) and (iii) results in two equilibrium points (Figure 6.10c), where the residence times

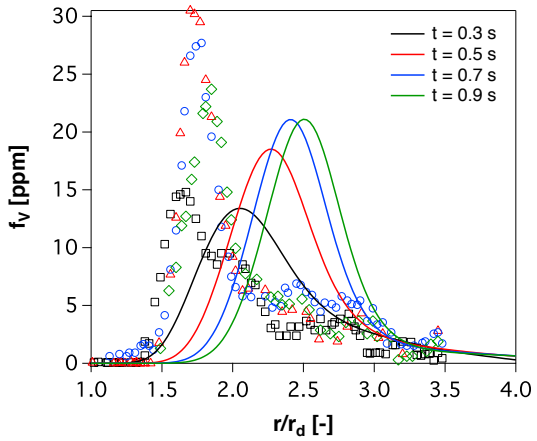

Figure 6.11: Predicted vs experimental [210] soot volume fraction profiles at different time steps. $d_0 = 2.90\,mm$.

are maximum. The outer one is unstable point because of its positive derivative. On the other hand, the inner one has a negative derivative and is then stable. As a result, SSR is located in correspondence of it, and coherently with its transient position, it gradually moves outwardly as combustion goes on.

To better understand this deviation, the evolution of the soot volume fraction has been evaluated. These data are not available in the work of Jackson and Avedisian. Such measurements were instead carried out in more recent works [209, 210], in the NASA drop tower at Cleveland, OH. Figure 6.11 shows a comparison with the experimental work by Manzello et al. [210]. Such trends are in line with what observed so far, i.e. the distribution being shifted outwardly. The predicted peaks are smaller than experimental values, and the simulated distribution is slightly wider than measurements in all the time steps. On the one hand, it must be acknowledged that the uncertainty in the measurement of the volume fraction is significant. Manzello et al. [210] report a value of 25% in their experimental measurements, compared to a ~5% error in FSR and SSR measurements. On the other, the deviations from experiments cannot be explained just with experimental uncertainty, especially considering that predicted SSR shows an offset of 1 diameter.

The reasons behind such mispredictions can be of different nature. First of all, both SSR overestimation and the volume fraction distribution may be connected to the equilibrium between Stefan flow and thermophoretic effect. Indeed, thermophoresis keeps soot particles away from the high temperature oxidative region (Figure 6.8), and increases their residence times in the region favorable to their growth. Intuitively, a stronger thermophoretic force would lower SSR profile, and increase the amount of produced soot. In the combustion community, the formu-

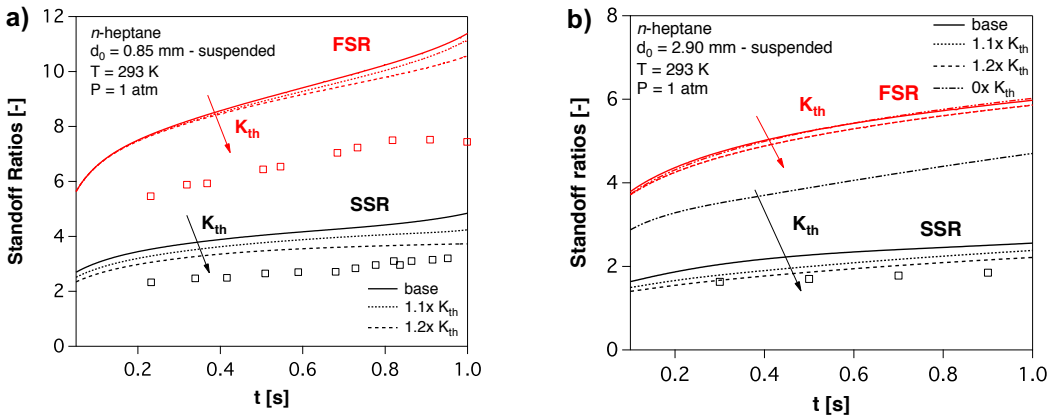

Figure 6.12: Sensitivity of standoff ratios to K_{th} value (Eq. 6.4). a) $d_0 = 0.855\,mm$ [185]. b) $d_0 = 2.90\,mm$ [210].

lation of thermophoretic velocity follows the law proposed by Waldmann [211], which has been implemented here (Eq. 6.4), too. Yet, not all available experimental data fit such equation, and measurements carried out in microgravity conditions [212] found out that the it may underestimate the actual impact of thermophoresis. The underestimation of SSR and f_v using such formulation was also experienced by Kumar et al. [213], who developed a semi-empirical model for predicting soot formation from *n*-heptane droplet combustion in microgravity conditions. In order to understand the sensitivity of the model to the Waldmann equation (6.4), a parametric analysis to the variation of K_{Th} has been carried out. Figure 6.12 shows the sensitivity of flame and soot standoff ratios to the thermophoretic force. FSR slightly decreases at the end of droplet combustion (Figure 6.12a), as a result of the radiative interaction with soot layer. The higher amount of soot increases radiation and lowers then the flame temperature. Therefore, the lower evaporation rate results in the flame getting closer to the droplet. On the other hand, the sensitivity of SSR is much more marked, and as expected, a higher thermophoretic velocity pushes the soot edge towards the droplet, and the numerical value gradually approaches the experimental. This increases, too, the amount of soot formed, and Figure 6.13 shows such dependency. Here, the key role of thermophoresis becomes apparent. Without considering it, the soot shell is far more detached from the droplet (Figure 6.12b), and the resulting soot concentrations are comparable with the diffusion and premixed cases shown in Section 6.1.2, i.e. O(ppm). Also, the maximum volume fraction is particularly sensitive to the value of K_{th}. Its multiplication by a factor 1.1, equivalent to an accommodation factor $\alpha = 0.6$ (instead of 0.9) returns peak values in line with the experimental observations. Nevertheless, the distribution is still shifted out-

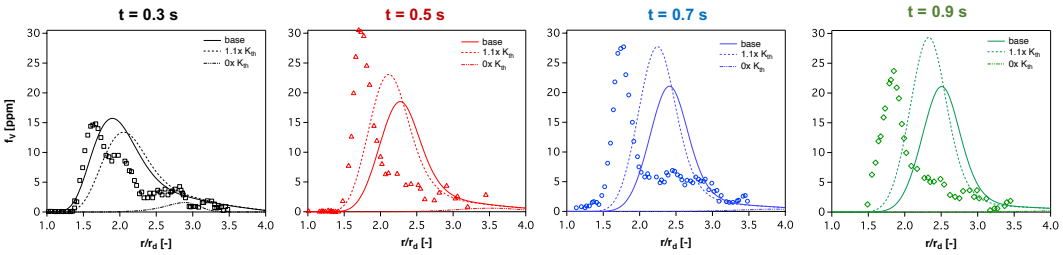

Figure 6.13: Sensitivity of f_v to K_{th} value at different times (Eq. 6.4). $d_0 = 2.90\,mm$ [210].

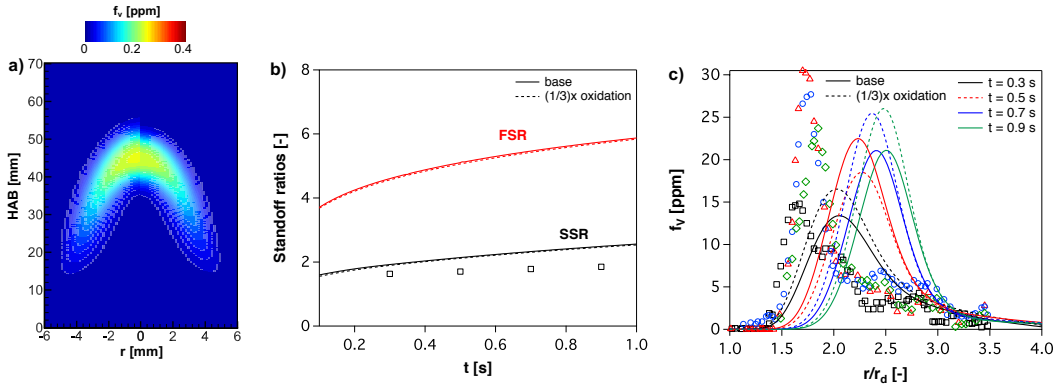

Figure 6.14: Sensitivity of soot dynamics to oxidation rates. a) Effects on coflow flame (Figure 6.5): mechanism with corrected oxidation reaction rates (left) vs base case (right). b) Soot standoff ratios and c) volume fraction sensitivity, compared with experimental data by Manzello et al. [210]. $d_0 = 2.90\,mm$.

wardly, thus meaning that thermophoresis alone is not able to explain the SSR deviation.

The second factor is related to the kinetic mechanism. Although it had been positively benchmarked against experimental data in Section 6.1.2, an underprediction of around a factor 2 in the soot maximum volume fraction had emerged when simulated the coflow flame investigated by Kashif et al. [197]. This is important in the context of isolated-droplet combustion for two reasons: (i) both problems are governed by transport, and (ii) in the coflow case, the thermophoretic effect is negligible, since convective velocities are higher, and there is no "trapping" effect for soot unlike in the droplet case. Therefore, at least in the coflow flame thermophoresis cannot be considered as the cause of underprediction. One of the conclusions drawn in Section [197] was that the factor 2 of difference could be related to the oxidation model, whose dynamics were not defined at an experimental level. To understand the possible weight of the oxidation in these cases, both the coflow flame and the droplet of Figure 6.11 have been simulated with a modified kinetic mechanism, where the oxidation rates have been divided by a factor 3. Figure 6.14 shows the sensitivity of the two systems. In the diffusion

flame, the soot thickness is stretched of ~2 mm, and becomes larger than the experimental value, while the peak volume fraction is 10% higher than in the base case. Anyway, it is still a factor ~2 lower than the experimental maximum, and cannot be then considered as the cause of this underestimation. In the isolated droplet, both standoff ratios (Figure 6.14b) are almost totally insensitive to oxidation rates: as a matter of fact, the soot profiles (Figure 6.14c) are not dramatically affected by the lower oxidation intensity, and the radial profiles are only dilatated in shape, such that the peak volume fraction is about 10% higher than the base case. No shift is observed, which was also expectable considering the substantial insensitivity to SSR.

6.3.3 Soot, radiation and radiative extinction

The investigation on the dynamics of soot formation in microgravity conditions is completed with a focus on the role of radiation in the combustion of larger sooting droplets. For sufficiently large initial diameters, i.e. O(mm), droplet evaporation cannot self-sustain the whole combustion process because of the radiative heat loss from the large flame, and extinction is reached at a certain point. Moreover, experiments on the International Space Station (ISS) [186] have also shown that after extinction, droplets keep burning in a cool flame regime, till the final extinction. In this second phase, the process is governed by Low Temperature Chemistry (LTC) with no visible flame emission. Therefore, a reliable description of chemistry is of primary importance to have a sufficient degree of predictability.

In such conditions, a proper modeling of radiative heat transfer assumes a primary importance: this includes gas radiation, as well as soot. To this purpose, the use of pseudo-spectral radiation models like Weighted-Sum-of-Gray-Gases (WSGG) are generally able to guarantee the highest accuracy [204]. Unfortunately, a generalized description of this kind is not available for soot but only for the major gas species, thus limiting its applicability in this situation, where the presence of soot might have a determining influence on the temperature field. An alternative approach, although of a semi-empirical type, consists in using the gray-gas approximation, and using a radiation correction coefficient, based on experimental evidence. In these cases, previous experience [214] has shown that the use of a correction coefficient equal to $0.5 - 0.6$ provides satisfactory results. This is a strong limitation of such approach restricting its predictability to the droplet-specific case, but at present it is the only viable way to keep soot radiation into account.

Recently, an experimental campaign has been carried out by Nayagam et

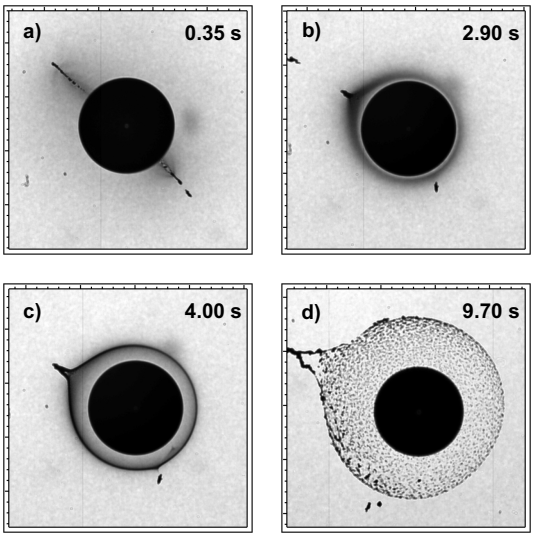

Figure 6.15: Direct photographs of the soot shell evolution. Fuel: *n*-decane. $d_0 = 4.369\,mm$; P = 1 atm; $T_0 = 293\,K$. Courtesy of D. Dietrich (NASA).

al. [215] on the ISS in order to study the cool-flame extinction of *n*-alkanes with different diameters. Figure 6.15 shows the time evolution of a *n*-decane, and direct photographs of the soot shell dynamics are reported. It is possible to observe that, soon after ignition, no soot is present around the droplet (a). Throughout its combustion (b,c), a progressively thicker (and symmetrical) soot layer is formed around the droplet, whose relative location (SSR) remains approximately constant. Just before radiative extinction (d), which is reached at 10.9 s, the soot layer is progressively dispersed in the surrounding air.

The evolution of the burning droplet (*n*-decane; $d_0 = 4.369\,mm$; P = 1 atm; $T_0 = 293\,K$) was simulated using the described conditions to represent the flame radiation; the complete soot mechanism, including high and low temperature reaction paths was used in order to observe the cool flame behavior after radiative extinction. A lower number of points (250) was used to make the computation affordable (which, anyway, required approximately one week). The evolution of the diameter is shown in Figure 6.16a. With the exception of the first 2-3 seconds, where experimental noise is likely present, a good agreement between measurements is observed. Also, Figure 6.16b highlights the model capability in predicting flame radiation. The shape of the radiated power is comparable with experimental data, although a slight underestimation is observed. This comparison should be analyzed very cautiously: the computed curve represents the overall heat emitted through gas and soot radiation, as evaluated through the related model; on the other hand, the experimental curve has measured the flame radiance in a delimited range of wavelengths. Thus, the two values do not directly correspond.

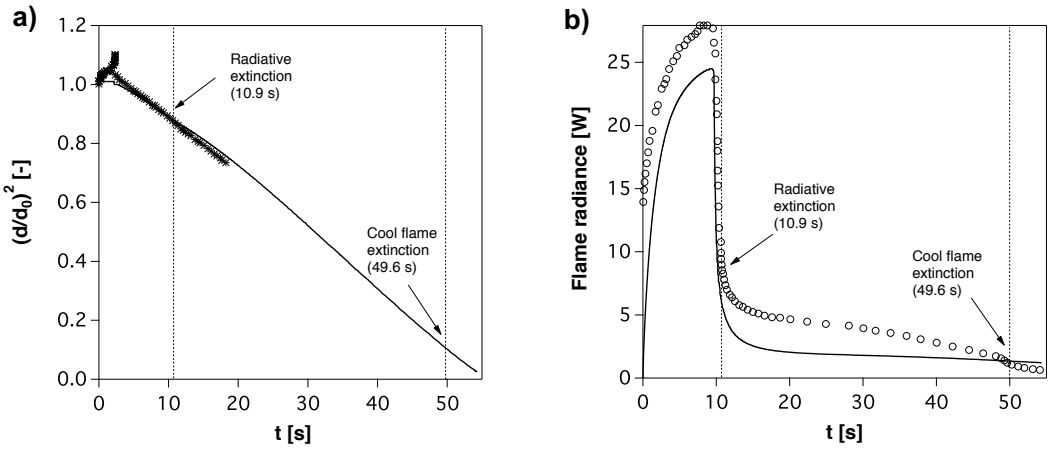

Figure 6.16: n-decane droplet evolution over time, before and after radiative extinction; a) diameter profile. b) flame radiance. Experimental data are courtesy of D. Dietrich (NASA)

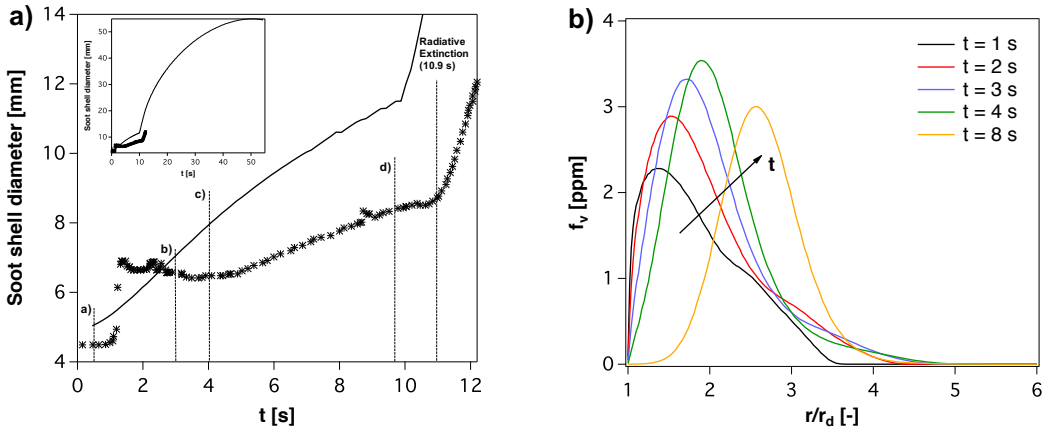

Figure 6.17: soot evolution in n-decane droplet over time: a) shell diameter (letters correspond to photographs in Figure 6.15). b) volume fraction. Experimental data are courtesy of D. Dietrich (NASA), not available for volume fraction

The evolution of soot is instead shown in Figure 6.17. Similarly to what observed in Section 6.3.2, the shell location is overestimated. On the other hand, the model well predicts the progressive departure of the shell from the surface close to radiative extinction. No experimental data are available with regard to soot volume fraction, nor to the total mass formed. The related profiles, shown in Figure 6.18, highlight that a slight consumption occurs over the cool flame burning, where its progressive dilution in the surrounding air causes the decrease in $f_{v,max}$.

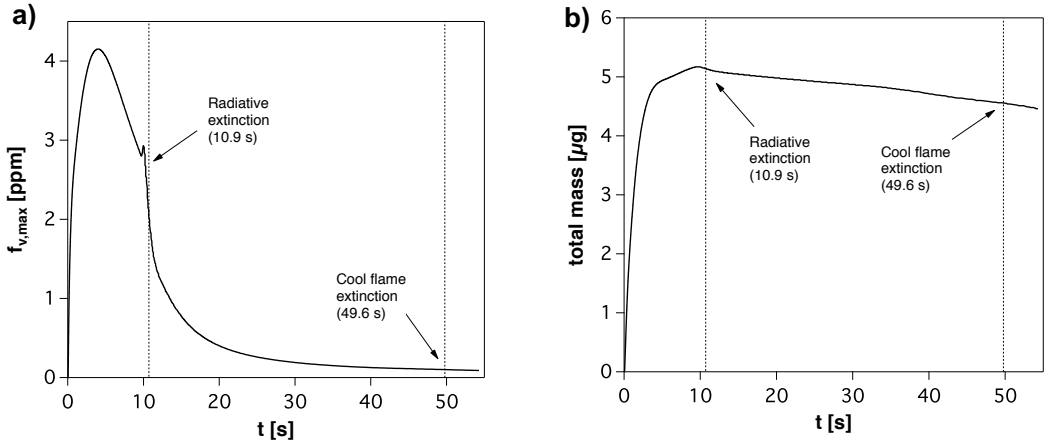

Figure 6.18: soot evolution in *n*-decane droplet over time: a) maximum soot volume fraction as a function of time). b) soot total mass over time.

6.4 Conclusions

The complexities behind the formation of soot in two-phase systems make fundamental studies a necessary instrument to gain insight into such dynamics by using proper simplifications. In this context, microgravity droplet experiments must be interpreted as a trade-off to study the soot evolution in presence of the basic phenomena governing also real devices. From a numerical point of view, they turn out as useful case studies to assess the validity of the kinetic and fluid dynamic hypotheses in idealized conditions. Yet, the numerical demand, mainly arising from the complexity of soot description, can still be the rate determining step of these analyses. For this reason, further simplification proved necessary, and the reduction framework introduced in this Thesis has found a proper application, although it required an adaptation to take into account the particular kinetic behavior of the aerosol phase.

After a preliminary verification of accuracy of the skeletal kinetic mechanism, the performed study has shed light on the phenomena playing a key importance in the involved dynamics. The main outcome has been the role of the thermophoretic effect in these conditions: without accounting for it, similar predictions to premixed and diffusion flames have been observed, i.e. volume fractions the order of ppm. More important, model performances have proven to be strongly sensitive to the thermophoretic law. The traditional formulation, which does not distinguish between particles size, is able to catch the progressive formation of the soot shell, with the predicted volume fraction in line with the experimental observations. Yet, considering the extreme sensitivity of the model and the experimental studies on aerosol particles [212] sometimes in disagreement with the Waldmann law,

further investigation is needed on this point, and a more complete particle-size dependent velocity can be a useful improvement in this direction [208].

The second point coming out from this study is the strong coupling and mutual interaction between soot layer and flame structure because of radiation. When soot concentrations are O(10) ppm, the heat lost because of it becomes significant. This has an influence on the flame transient location and temperature, which are both decreased because of it. Moreover, such interaction becomes determining for larger droplets, where the radiative losses are sufficiently high to bring the flame to extinction. Here the model is further complicated by the presence of cool flame burning following the radiative extinction. Anyway, apart from the heavier computing demand, the inclusion of low-temperature chemistry and its coupling to the base model is able to quantitatively reproduce the cool flame behavior and final extinction. The downside of this approach is the semi-empirical approach to radiation: the use of a correction coefficient due to the gray model adopted limits the predictability of the radiation model in different situations (fuel, pressure, ambient air). Generalizing the calculation of radiative heat transfer for any medium is still an open issue in combustion science [216], and is a primary need to be accomplished in the next future also for the isolated droplet model.

CHAPTER 7

Conclusions and outlooks

The use of modeling activity to support, design and sometimes replace experiments is today a common practice in combustion science. In this context, the key importance of adopting detailed kinetic chemistry has been progressively recognized, and the currently available computational resources allow its direct implementation for the smallest fuels (CH_4, H_2). On the other hand, the need for mechanism simplification is apparent when more complex fuels are involved, like those feeding gasoline, jet and diesel engines. Yet, finding the optimal trade-off between size and accuracy is not straightforward.

In this Thesis, it has been shown that a multistep approach is required to reach the final target. The coupling of lumping and skeletal reduction approaches proved effective to shrink the size of the original input without losing accuracy. The upstream use of lumping when generating the detailed kinetic schemes resulted in a simpler and more effective benchmark phase of the final scheme, directly accomplished on the lumped mechanism. Moreover, it was shown that the accuracy of a kinetic mechanism cannot always be quantified with the traditional target property of ignition delay time. For species characterized by longer time scales, matching ignition delay time is a necessary but not sufficient condition to preserve accuracy on their dynamics of formation. For this reason, a novel error metric has

been developed for error quantification, initially conceived for model/experiments comparison, and successfully applied in the reduction framework.

Relying on these cornerstones, a numerical tool, `DoctorSMOKE++`, was created to obtain skeletal mechanisms with the desired accuracy on the defined target properties. The numerical framework of `OpenSMOKE++` behind it, and the distributed-memory protocol make it a useful and flexible instrument for model reduction, which is expected to be freely released to the combustion community in the next future. Indeed, an instrument able to quickly "preprocess" a kinetic mechanism according to the specific purposes can be an important resource for everybody dealing with chemical kinetics implementation in CFD applications. The effectiveness of the procedure was shown through two applications involving fundamental studies on the two different types of property targets, which skeletal reduction can be targeted at. In both cases, the use of skeletal mechanisms has allowed to obtain model output in limited times - O(hours) - and a wider range of conditions could be then explored. The conclusions obtained from them can be of major importance when (i) implementing spray submodels and evaluating physical properties of fuel surrogates (cfr. Chapter 5) or (ii) refining kinetic models and thermophoretic flow description (cfr. Chapter 6).

Of course, several work can be still carried out to further refine the reduction methodology, as well as for what concerns their applications. This Thesis ends with a short mention to some of them.

7.1 Extending DoctorSMOKE++: QSSA approach

The main limitation of skeletal reduction approaches lies in the fact that they are based on a removal strategy, i.e. cutting the part of a mechanism (species and/or reactions), which is identified as marginal for the target accuracy. This means that, since reaction rates are not modified, there is a physical limit, in terms of mechanism size, after which a given accuracy cannot be guaranteed anymore, regardless of the skeletal reduction methodology. If further reduction is required, a different strategy must be devised.

A possibility is applying the Quasi Steady-State Approximation (QSSA) to radicals with the fastest time scales. For example, Lu and Law [139] proposed a criterion based on Computational Singular Perturbation (CSP) to identify species with "fast" time scales. In this way, transport equations for those species would not need to be added, since their local value would be the result of the resolution of an algebraic system obtained by imposing no accumulation for each of them. The drawback of this approach is the need to readapt the numerical codes where

the kinetic mechanism is to be used, in the form of a DAE problem, instead of ODE. But regardless of the required additional coding, QSSA can prove crucial in providing a further significant reduction to the mechanism size: to give an example, Luong et al. [15] further reduced the 171-species mechanism for PRF to 116 species through QSSA [217] for its use in DNS. Therefore, if lumping is further added upstream, considering that the mechanism obtained for TRF in Section 4.5.2 included 114 species without QSSA, the competitiveness of the resulting mechanism becomes apparent.

7.2 Analyzing soot formation in turbulent flames

The use of idealized systems to investigate the dynamics of combustion and pollutants formation is very useful to test the performance of the single submodels adopted in more complex systems. Indeed, important findings had arisen from the extensive analysis of the soot formation in the isolated droplet combustion (Section 6.3), which allowed to identify the determining role of thermophoresis and flame radiance, as well as to further benchmark the soot kinetic mechanism in non-premixed conditions. Nevertheless, when the focus is addressed towards more realistic applications, the problem becomes conceptually and numerically challenging. In turbulent flames, which constitute the vast majority of combustion applications, soot chemistry is only one of the factors determining its formation, which also depends on flow history and local turbulence properties. In this case, a fundamental insight can only be gained through DNS and LES simulations; here, using a 195-species mechanism for such simulations is unfeasible, especially for DNS. Recently, three-dimensional simulations of turbulent sooting flames, fed by n-heptane, were carried out by using a 47-species mechanism [181, 218], coupled to a solid phase description through a hybrid method of moments. Therefore, further simplification is needed for a successful implementation of detailed kinetics of soot.

In addition to the QSSA methodology described in Section 7.1, further reduction can only be achieved by acting on the soot description. Indeed, about 40% of the skeletal mechanism is constituted by the soot pseudo-species. For this reason, the multistep methodology can be coupled to a dynamic management of the number of discrete sections constituting the solid-phase model. In the current mechanism, discretization is carried out through 20 sections describing the size distribution, and 3 sections representing the variable composition. Considering that both radicals and molecules are represented, coarsening such description would prove particularly useful to decrease the total number of soot species. To

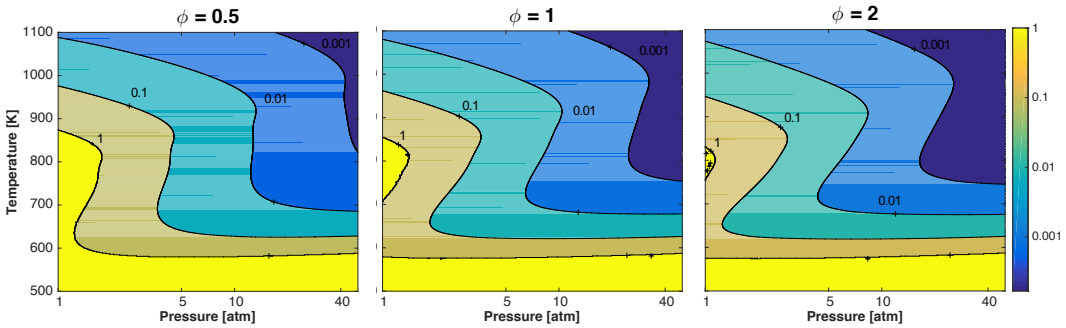

Figure 7.1: Map of constant-pressure ignition delay time (in seconds). Simulations were carried out via POLIMI_1412 mechanism [9].

this end, an adaptive procedure needs be implemented, able to return a soot submodel according to the level of accuracy required by the used, similarly to what already done by `DoctorSMOKE++` through the STSA methodology. This procedure would not fall outside skeletal reduction methods: since the reaction stoichiometries would need to be automatically adjusted according to the number, size and type of sections, an automatic approach must be properly devised to generate chemical reactions according to the desired input parameters, then returning the subset of solid-phase reactions to be attached to the gas-phase model. Although the development of such a parallel instrument is not straightforward, it is subject of ongoing and future research.

7.3 Investigating LTC in turbulent combustion

As widely shown in Chapter 2 and 4, one of the most delicate features of kinetic mechanisms for large hydrocarbon fuels is their capability in representing their low temperature behavior, and the consequent NTC region of transition to the traditional high temperature chemistry. As a matter of fact, in the latest years an increasing interest in this topic is being raised because of the continuous efforts towards efficiency improvements of burners and engines. To this purpose, the common trend of the newly conceived combustion technologies [219–221] consists in operating at elevated temperatures and pressures. In these conditions, the low temperature ignition delay time may be significantly shortened, to the point that its length may become competitive with the other involved time scales (i.e. flame and turbulence); as an illustrative example, Figure 7.1 shows its variability with pressure and temperature for *n*-decane, a representative *n*-alkane exhibiting LTC/NTC behavior.

From a CFD perspective, this issue has been rarely faced so far, presumably for two main reasons: (i) the operating conditions of "traditional" combustors,

which could reasonably allow to exclude *a priori* the importance of LTC; (ii) the need to accommodate detailed chemistry into the related simulations, in order to guarantee the right reliability. Nevertheless, the increasing capabilities in the High Performance Computing have allowed to perform some fundamental studies in this direction. For instance, Yoo et al. [222] carried out a DNS parametric study to assess the effects of thermal stratification and turbulent mixing timescales on the auto-ignition of a lean *n*-heptane/air mixture at elevated pressure, quantifying such dependences in the NTC regime, too. Other studies [223, 224] revealed the different, and so far unexplored, combustion regimes which can occur when the fuel exhibits an LTC chemistry.

From an experimental standpoint, the role of LTC in turbulent flame propagation has been recently studied by Won et al. [11]. They used a newly-conceived burner (Reactor Assisted Turbulent Slot - RATS) to analyze turbulent flame regimes and burning rates of *n*-heptane, as the smallest species representative of real fuels. Their major outcome was finding out that when ignition time scale becomes comparable to flow and flame time scales, a low-temperature ignition turbulent flame regime is established, due to the preliminary conversion of the fuel in low-temperature intermediates, which then enter the turbulent flame and alter its propagation rates.

To the end of finding new operating conditions with higher efficiency and lower emissions, these outcomes are particularly interesting. Following these first experimental findings, the actual potentials of low temperature regime need to be delineated. In numerical terms, an LES investigation could elucidate the flame behavior in the different operating conditions. Yet, to make it predictable, an accurate kinetic description of the low temperature behavior is required; at the same time, the high intrinsic demand of LES calculation prevents from adopting a detailed mechanism as it is. In this background, the application of the multistep methodology developed here finds a direct application, and its coupling with fluid dynamic solvers may prove a winning combination to shed light on the nonconventional flame regime developed in these conditions.

Bibliography

[1] International Energy Agency, World energy outlook, OECD, 2015.

[2] EIA, US, Annual energy outlook 2013, US Energy Information Administration, Washington, DC (2013) 60–62.

[3] S. Shafiee, E. Topal, When will fossil fuel reserves be diminished?, Energy policy 37 (1) (2009) 181–189.

[4] C. Guerreiro, F. de Leeuw, V. Foltescu, et al., Air Quality in Europe: 2013 Report, Publications Office, 2013.

[5] The European Parliament and the Council of the European Union, Regulation (EC) no 715/2007 of the European Parliament and of the council of 20 June 2007, Official Journal of the European Union 171.

[6] A. Bandivadekar, K. Bodek, L. Cheah, C. Evans, T. Groode, J. Heywood, E. Kasseris, K. Kromer, M. Weiss, On the road in 2035: Reducing transportation's petroleum consumption and GHG emissions, Tech. Rep. Report No. LFEE 2008-05 RP, Massachusetts Institute of Technology, Laboratory for Energy and the Environment (July 2008).

[7] B. Johnson, C. Edwards, Exploring the pathway to high efficiency IC engines through exergy analysis of heat transfer reduction, SAE International Journal of Engines 6 (1) (2013) 150–166.

[8] C. K. Westbrook, Y. Mizobuchi, T. J. Poinsot, P. J. Smith, J. Warnatz, Computational combustion, Proceedings of the Combustion Institute 30 (1) (2005) 125–157.

[9] E. Ranzi, A. Frassoldati, R. Grana, A. Cuoci, T. Faravelli, A. Kelley, C. Law, Hierarchical and comparative kinetic modeling of laminar flame speeds of hydrocarbon and oxygenated fuels, Progress in Energy and Combustion Science 38 (4) (2012) 468–501.

[10] T. Lu, C. K. Law, Toward accommodating realistic fuel chemistry in large-scale computations, Progress in Energy and Combustion Science 35 (2) (2009) 192–215.

[11] S. H. Won, B. Windom, B. Jiang, Y. Ju, The role of low temperature fuel chemistry on turbulent flame propagation, Combustion and Flame 161 (2) (2014) 475–483.

[12] A. Cavaliere, M. de Joannon, Mild combustion, Progress in Energy and Combustion science 30 (4) (2004) 329–366.

[13] G. H. Golub, C. F. Van Loan, Matrix computations, Vol. 3, JHU Press, 2012.

[14] T. Poinsot, D. Veynante, Theoretical and numerical combustion, Cerfacs, 2015.

[15] M. B. Luong, Z. Luo, T. Lu, S. H. Chung, C. S. Yoo, Direct numerical simulations of the ignition of lean primary reference fuel/air mixtures with temperature inhomogeneities, Combustion and Flame 160 (10) (2013) 2038–2047.

[16] A. Cuoci, A. Frassoldati, T. Faravelli, E. Ranzi, OpenSMOKE++: An object-oriented framework for the numerical modeling of reactive systems with detailed kinetic mechanisms, Computer Physics Communications 192 (2015) 237–264.

[17] G. Li, H. Rabitz, A general analysis of exact lumping in chemical kinetics, Chemical engineering science 44 (6) (1989) 1413–1430.

[18] H. Wang, M. Frenklach, Detailed reduction of reaction mechanisms for flame modeling, Combustion and Flame 87 (3) (1991) 365–370.

[19] K. E. Niemeyer, C.-J. Sung, M. P. Raju, Skeletal mechanism generation for surrogate fuels using directed relation graph with error propagation and sensitivity analysis, Combustion and Flame 157 (9) (2010) 1760–1770.

[20] C. K. Law, Combustion physics, Cambridge university press, 2006.

[21] K. H. Altgelt, Composition and analysis of heavy petroleum fractions, CRC Press, 1993.

[22] C. Chevalier, W. Pitz, J. Warnatz, C. Westbrook, H. Melenk, Hydrocarbon ignition: automatic generation of reaction mechanisms and applications to modeling of engine knock, in: Symposium (International) on Combustion, Vol. 24, Elsevier, 1992, pp. 93–101.

[23] G. L. Steele Jr, R. P. Gabriel, The evolution of Lisp, in: acm sigplan Notices, Vol. 28, ACM, 1993, pp. 231–270.

[24] R. R. Baldwin, M. W. Hisham, R. W. Walker, Arrhenius parameters of elementary reactions involved in the oxidation of neopentane, Journal of the Chemical Society, Faraday Transactions 1: Physical Chemistry in Condensed Phases 78 (5) (1982) 1615–1627.

[25] J. Warnatz, Rate coefficients in the C/H/O system, in: Combustion chemistry, Springer, 1984, pp. 197–360.

[26] R. Walker, Temperature coefficients for reactions of OH radicals with alkanes between 300 and 1000 K, International journal of chemical kinetics 17 (6) (1985) 573–582.

[27] R. Walker, Reactions of HO_2 radicals in combustion chemistry, in: Symposium (International) on Combustion, Vol. 22, Elsevier, 1989, pp. 883–892.

[28] E. S. Blurock, Reaction: system for modeling chemical reactions, Journal of chemical information and computer sciences 35 (3) (1995) 607–616.

[29] E. Ranzi, T. Faravelli, P. Gaffuri, A. Sogaro, Low-temperature combustion: automatic generation of primary oxidation reactions and lumping procedures, Combustion and Flame 102 (1) (1995) 179–192.

[30] G. Côme, V. Warth, P. Glaude, R. Fournet, F. Battin-Leclerc, G. Scacchi, Computer-aided design of gas-phase oxidation mechanisms—application to the modeling of n-heptane and iso-octane oxidation, in: Symposium (International) on Combustion, Vol. 26, Elsevier, 1996, pp. 755–762.

[31] L. Broadbelt, S. Stark, M. Klein, Computer generated reaction modelling: decomposition and encoding algorithms for determining species uniqueness, Computers & chemical engineering 20 (2) (1996) 113–129.

[32] R. G. Susnow, A. M. Dean, W. H. Green, P. Peczak, L. J. Broadbelt, Rate-based construction of kinetic models for complex systems, The Journal of Physical Chemistry A 101 (20) (1997) 3731–3740.

[33] V. Warth, F. Battin-Leclerc, R. Fournet, P.-A. Glaude, G.-M. Côme, G. Scacchi, Computer based generation of reaction mechanisms for gas-phase oxidation, Computers & chemistry 24 (5) (2000) 541–560.

[34] D. M. Matheu, A. M. Dean, J. M. Grenda, W. H. Green, Mechanism generation with integrated pressure dependence: A new model for methane pyrolysis, The Journal of Physical Chemistry A 107 (41) (2003) 8552–8565.

[35] F. Battin-Leclerc, J. M. Simmie, E. Blurock, Cleaner Combustion, Springer, 2013.

[36] H. Curran, P. Gaffuri, W. J. Pitz, C. K. Westbrook, A comprehensive modeling study of *n*-heptane oxidation, Combustion and Flame 114 (1) (1998) 149–177.

[37] H. J. Curran, P. Gaffuri, W. Pitz, C. Westbrook, A comprehensive modeling study of iso-octane oxidation, Combustion and Flame 129 (3) (2002) 253–280.

[38] P.-A. Glaude, F. Battin-Leclerc, R. Fournet, V. Warth, G.-M. Côme, G. Scacchi, Construction and simplification of a model for the oxidation of alkanes, Combustion and Flame 122 (4) (2000) 451–462.

[39] G. Bikas, N. Peters, Kinetic modelling of *n*-decane combustion and autoignition, Combustion and Flame 126 (1) (2001) 1456–1475.

[40] W. Green, P. Barton, B. Bhattacharjee, D. Matheu, D. Schwer, J. Song, R. Sumathi, H.-H. Carstensen, A. Dean, J. Grenda, Computer construction of detailed chemical kinetic models for gas-phase reactors, Industrial & engineering chemistry research 40 (23) (2001) 5362–5370.

[41] E. Ranzi, A. Frassoldati, S. Granata, T. Faravelli, Wide-range kinetic modeling study of the pyrolysis, partial oxidation, and combustion of heavy n-alkanes, Industrial & engineering chemistry research 44 (14) (2005) 5170–5183.

[42] E. Ranzi, C. Cavallotti, A. Cuoci, A. Frassoldati, M. Pelucchi, T. Faravelli, New reaction classes in the kinetic modeling of low temperature oxidation of n-alkanes, Combustion and flame 162 (5) (2015) 1679–1691.

[43] E. Ranzi, T. Faravelli, P. Gaffuri, E. Garavaglia, A. Goldaniga, Primary pyrolysis and oxidation reactions of linear and branched alkanes, Industrial & engineering chemistry research 36 (8) (1997) 3336–3344.

[44] C. K. Westbrook, C. V. Naik, O. Herbinet, W. J. Pitz, M. Mehl, S. M. Sarathy, H. J. Curran, Detailed chemical kinetic reaction mechanisms for soy and rapeseed biodiesel fuels, Combustion and Flame 158 (4) (2011) 742–755.

[45] C. K. Westbrook, W. J. Pitz, O. Herbinet, H. J. Curran, E. J. Silke, A comprehensive detailed chemical kinetic reaction mechanism for combustion of n-alkane hydrocarbons from n-octane to n-hexadecane, Combustion and Flame 156 (1) (2009) 181–199.

[46] H. Huang, M. Fairweather, J. Griffiths, A. Tomlin, R. Brad, A systematic lumping approach for the reduction of comprehensive kinetic models, Proceedings of the Combustion Institute 30 (1) (2005) 1309–1316.

[47] S. M. Jacob, B. Gross, S. E. Voltz, V. W. Weekman, A lumping and reaction scheme for catalytic cracking, AIChE Journal 22 (4) (1976) 701–713.

[48] R. Djouad, B. Sportisse, N. Audiffren, Reduction of multiphase atmospheric chemistry, Journal of Atmospheric Chemistry 46 (2) (2003) 131–157.

[49] M. Dente, E. Ranzi, A. Goossens, Detailed prediction of olefin yields from hydrocarbon pyrolysis through a fundamental simulation model (SPYRO), Computers & Chemical Engineering 3 (1) (1979) 61–75.

[50] M. Dente, E. Ranzi, S. Barendregt, A. Goossens, Radical reaction mechanisms in the pyrolysis of light hydrocarbons, AIChE-meeting–presentation, 1979.

[51] T. Turanyi, T. Berces, S. Vajda, Reaction rate analysis of complex kinetic systems, International Journal of Chemical Kinetics 21 (2) (1989) 83–99.

[52] J. Wei, J. C. W. Kuo, Lumping analysis in monomolecular reaction systems. analysis of the exactly lumpable system, Industrial & Engineering Chemistry Fundamentals 8 (1) (1969) 114–123.

[53] M. Pelucchi, M. Bissoli, C. Cavallotti, A. Cuoci, T. Faravelli, A. Frassoldati, E. Ranzi, A. Stagni, Improved kinetic model of the low-temperature oxidation of n-heptane, Energy & Fuels 28 (11) (2014) 7178–7193.

[54] M. Mehl, W. J. Pitz, C. K. Westbrook, H. J. Curran, Kinetic modeling of gasoline surrogate components and mixtures under engine conditions, Proceedings of the Combustion Institute 33 (1) (2011) 193–200.

[55] A. Stagni, A. Cuoci, A. Frassoldati, T. Faravelli, E. Ranzi, Lumping and reduction of detailed kinetic schemes: an effective coupling, Industrial & Engineering Chemistry Research 53 (22) (2014) 9004–9016.

[56] H. Ciezki, G. Adomeit, Shock-tube investigation of self-ignition of n-heptane-air mixtures under engine relevant conditions, Combustion and Flame 93 (4) (1993) 421–433.

[57] S. S. Vasu, D. F. Davidson, Z. Hong, V. Vasudevan, R. K. Hanson, n-dodecane oxidation at high-pressures: Measurements of ignition delay times and OH concentration time-histories, Proceedings of the Combustion Institute 32 (1) (2009) 173–180.

[58] D. Davidson, Z. Hong, G. Pilla, A. Farooq, R. Cook, R. Hanson, Multi-species time-history measurements during n-dodecane oxidation behind reflected shock waves, Proceedings of the Combustion Institute 33 (1) (2011) 151–157.

[59] P. Dagaut, M. Reuillon, M. Cathonnet, Experimental study of the oxidation of n-heptane in a jet stirred reactor from low to high temperature and pressures up to 40 atm, Combustion and Flame 101 (1) (1995) 132–140.

[60] A. Mzé-Ahmed, K. Hadj-Ali, P. Dagaut, G. Dayma, Experimental and modeling study of the oxidation kinetics of n-undecane and n-dodecane in a jet-stirred reactor, Energy & Fuels 26 (7) (2012) 4253–4268.

[61] B. Li, N. Liu, R. Zhao, F. N. Egolfopoulos, H. Zhang, Extinction studies of flames of heavy neat hydrocarbons and practical fuels, Journal of Propulsion and Power 29 (2) (2013) 352–361.

[62] K. Kumar, C.-J. Sung, Laminar flame speeds and extinction limits of preheated n-decane/O_2/N_2 and n-dodecane/O_2/N_2 mixtures, Combustion and Flame 151 (1) (2007) 209–224.

[63] S. Davis, C. Law, Determination of and fuel structure effects on laminar flame speeds of C_1 to C_8 hydrocarbons, Combustion Science and Technology 140 (1-6) (1998) 427–449.

[64] C. Ji, E. Dames, Y. L. Wang, H. Wang, F. N. Egolfopoulos, Propagation and extinction of premixed C_5–C_{12} n-alkane flames, Combustion and Flame 157 (2) (2010) 277–287.

[65] H. Rabitz, M. Kramer, D. Dacol, Sensitivity analysis in chemical kinetics, Annual review of physical chemistry 34 (1) (1983) 419–461.

[66] A. S. Tomlin, M. J. Pilling, J. H. Merkin, J. Brindley, N. Burgess, A. Gough, Reduced mechanisms for propane pyrolysis, Industrial & engineering chemistry research 34 (11) (1995) 3749–3760.

[67] S. Vajda, P. Valko, T. Turanyi, Principal component analysis of kinetic models, International Journal of Chemical Kinetics 17 (1) (1985) 55–81.

[68] N. J. Brown, G. Li, M. L. Koszykowski, Mechanism reduction via principal component analysis, International journal of chemical kinetics 29 (6) (1997) 393–414.

[69] T. Lu, Y. Ju, C. K. Law, Complex CSP for chemistry reduction and analysis, Combustion and Flame 126 (1) (2001) 1445–1455.

[70] L. Elliott, D. B. Ingham, A. G. Kyne, N. S. Mera, M. Pourkashanian, C. W. Wilson, Reaction mechanism reduction and optimization using genetic algorithms, Industrial & engineering chemistry research 44 (4) (2005) 658–667.

[71] A. S. Tomlin, M. J. Pilling, T. Turányi, J. H. Merkin, J. Brindley, Mechanism reduction for the oscillatory oxidation of hydrogen: sensitivity and quasi-steady-state analyses, Combustion and Flame 91 (2) (1992) 107–130.

[72] L. Whitehouse, A. Tomlin, M. Pilling, Systematic reduction of complex tropospheric chemical mechanisms, part I: sensitivity and time-scale analyses, Atmospheric Chemistry and Physics 4 (7) (2004) 2025–2056.

[73] T. Nagy, T. Turányi, Reduction of very large reaction mechanisms using methods based on simulation error minimization, Combustion and Flame 156 (2) (2009) 417–428.

[74] T. Turanyi, Reduction of large reaction mechanisms, New journal of chemistry 14 (11) (1990) 795–803.

[75] T. Lu, C. K. Law, A directed relation graph method for mechanism reduction, Proceedings of the Combustion Institute 30 (1) (2005) 1333–1341.

[76] P. Pepiot-Desjardins, H. Pitsch, An efficient error-propagation-based reduction method for large chemical kinetic mechanisms, Combustion and Flame 154 (1) (2008) 67–81.

[77] W. Sun, Z. Chen, X. Gou, Y. Ju, A path flux analysis method for the reduction of detailed chemical kinetic mechanisms, Combustion and Flame 157 (7) (2010) 1298–1307.

[78] E. Ranzi, A. Frassoldati, A. Stagni, M. Pelucchi, A. Cuoci, T. Faravelli, Reduced kinetic schemes of complex reaction systems: Fossil and biomass-derived transportation fuels, International Journal of Chemical Kinetics 46 (9) (2014) 512–542.

[79] L. Tosatto, B. A. V. Bennett, M. D. Smooke, Comparison of different drg-based methods for the skeletal reduction of jp-8 surrogate mechanisms, Combustion and Flame 160 (9) (2013) 1572–1582.

[80] R. K. Mohammed, M. A. Tanoff, M. D. Smooke, A. M. Schaffer, M. B. Long, Computational and experimental study of a forced, timevarying, axisymmetric, laminar diffusion flame, in: Symposium (International) on Combustion, Vol. 27, Elsevier, 1998, pp. 693–702.

[81] A. Cuoci, A. Frassoldati, T. Faravelli, E. Ranzi, A computational tool for the detailed kinetic modeling of laminar flames: Application to c 2 h 4/ch 4 coflow flames, Combustion and Flame 160 (5) (2013) 870–886.

[82] K. Narayanaswamy, P. Pepiot, H. Pitsch, A chemical mechanism for low to high temperature oxidation of n-dodecane as a component of transportation fuel surrogates, Combustion and Flame 161 (4) (2014) 866–884.

[83] P. Pepiot-Desjardins, H. Pitsch, An automatic chemical lumping method for the reduction of large chemical kinetic mechanisms, Combustion Theory and Modelling 12 (6) (2008) 1089–1108.

[84] X. Zheng, T. Lu, C. Law, Experimental counterflow ignition temperatures and reaction mechanisms of 1, 3-butadiene, Proceedings of the Combustion Institute 31 (1) (2007) 367–375.

[85] J. Bugler, K. P. Somers, E. J. Silke, H. J. Curran, Revisiting the kinetics and thermodynamics of the low-temperature oxidation pathways of alkanes: A case study of the three pentane isomers, The Journal of Physical Chemistry A 119 (28) (2015) 7510–7527.

[86] C. Olm, I. G. Zsély, R. Pálvölgyi, T. Varga, T. Nagy, H. J. Curran, T. Turányi, Comparison of the performance of several recent hydrogen combustion mechanisms, Combustion and Flame 161 (9) (2014) 2219–2234.

[87] C. Olm, I. G. Zsély, T. Varga, H. J. Curran, T. Turányi, Comparison of the performance of several recent syngas combustion mechanisms, Combustion and Flame 162 (5) (2015) 1793–1812.

[88] G. Mittal, C.-J. Sung, R. A. Yetter, Autoignition of H_2/CO at elevated pressures in a rapid compression machine, International Journal of Chemical Kinetics 38 (8) (2006) 516–529.

[89] M. S. Bernardi, M. Pelucchi, A. Stagni, L. M. Sangalli, A. Cuoci, P. Secchi, T. Faravelli, Curve matching: a generalized framework for combustion model comparison and validation, Combustion and Flame 168 (2016) 186–203.

[90] J. O. Ramsay, Functional data analysis, Wiley Online Library, 2006.

[91] T. Held, A. Marchese, F. Dryer, A semi-empirical reaction mechanism for n-heptane oxidation and pyrolysis, Combustion Science and Technology 123 (1-6) (1997) 107–146.

[92] H. Hakka, R. Cracknell, A. Pekalski, P.-A. Glaude, F. Battin-Leclerc, Experimental and modeling study of ultra-rich oxidation of n-heptane, Fuel 144 (2015) 358–368.

[93] D. Mishra, Experimental Combustion: An Introduction, Crc Press, 2014.

[94] L. Vernier, Kinetic modeling of NOx formation and reduction, Master's thesis, Politecnico di Milano (2015).

[95] Creck modeling web page [cited September 2015].
URL `http://creckmodeling.chem.polimi.it`

[96] A. Stagni, A. Frassoldati, A. Cuoci, T. Faravelli, E. Ranzi, Skeletal mechanism reduction through species-targeted sensitivity analysis, Combustion and Flame 163 (2016) 382–393.

[97] M. Mehl, W. Pitz, M. Sjöberg, J. E. Dec, Detailed kinetic modeling of low-temperature heat release for PRF fuels in an HCCI engine, Tech. rep., SAE Technical Paper (2009).

[98] R. Seiser, H. Pitsch, K. Seshadri, W. Pitz, H. Gurran, Extinction and autoignition of n-heptane in counterflow configuration, Proceedings of the Combustion Institute 28 (2) (2000) 2029–2037.

[99] L. Cai, H. Pitsch, Optimized chemical mechanism for combustion of gasoline surrogate fuels, Combustion and Flame 162 (5) (2015) 1623–1637.

[100] J. C. Prince, F. A. Williams, G. E. Ovando, A short mechanism for the low-temperature ignition of n-heptane at high pressures, Fuel 149 (2015) 138–142.

[101] L. Seidel, K. Moshammer, X. Wang, T. Zeuch, K. Kohse-Höinghaus, F. Mauss, Comprehensive kinetic modeling and experimental study of a fuel-rich, premixed n-heptane flame, Combustion and Flame 162 (5) (2015) 2045–2058.

[102] H.-P. S. Shen, J. Steinberg, J. Vanderover, M. A. Oehlschlaeger, A shock tube study of the ignition of n-heptane, n-decane, n-dodecane, and n-tetradecane at elevated pressures, Energy & Fuels 23 (5) (2009) 2482–2489.

[103] Y. Huang, C. Sung, J. Eng, Laminar flame speeds of primary reference fuels and reformer gas mixtures, Combustion and Flame 139 (3) (2004) 239–251.

[104] S. Jerzembeck, N. Peters, P. Pepiot-Desjardins, H. Pitsch, Laminar burning velocities at high pressure for primary reference fuels and gasoline: Experimental and numerical investigation, Combustion and Flame 156 (2) (2009) 292–301.

[105] Y. Xin, D. A. Sheen, H. Wang, C. K. Law, Skeletal reaction model generation, uncertainty quantification and minimization: Combustion of butane, Combustion and Flame 161 (12) (2014) 3031–3039.

[106] K. E. Niemeyer, C.-J. Sung, On the importance of graph search algorithms for DRGEP-based mechanism reduction methods, Combustion and Flame 158 (8) (2011) 1439–1443.

[107] E. W. Dijkstra, A note on two problems in connexion with graphs, Numerische mathematik 1 (1) (1959) 269–271.

[108] K. E. Niemeyer, C.-J. Sung, Reduced chemistry for a gasoline surrogate valid at engine-relevant conditions, Energy & Fuels 29 (2) (2015) 1172–1185.

[109] J. A. Miller, M. C. Branch, W. J. McLean, D. W. Chandler, M. D. Smooke, R. J. Kee, The conversion of HCN to NO and N_2 in H_2-O_2-HCN-Ar flames at low pressure, in: Symposium (International) on Combustion, Vol. 20, Elsevier, 1985, pp. 673–684.

[110] T. P. Coffee, J. M. Heimerl, Sensitivity analysis for premixed, laminar, steady state flames, Combustion and Flame 50 (1983) 323–340.

[111] Y. Reuven, M. D. Smooke, H. Rabitz, Sensitivity analysis of boundary value problems: Application to nonlinear reaction-diffusion systems, Journal of computational physics 64 (1) (1986) 27–55.

[112] R. Rota, F. Bonini, A. Servida, M. Morbidelli, S. Carra, Analysis of detailed kinetic schemes for combustion processes: Application to a methane-ethane mixture, Chemical engineering science 49 (24) (1994) 4211–4221.

[113] C. J. Montgomery, S. Cannon, M. Mawid, B. Sekar, Reduced chemical kinetic mechanisms for JP-8 combustion, Tech. rep., DTIC Document (2002).

[114] S. Honnet, K. Seshadri, U. Niemann, N. Peters, A surrogate fuel for kerosene, Proceedings of the Combustion Institute 32 (1) (2009) 485–492.

[115] S. Dooley, S. H. Won, M. Chaos, J. Heyne, Y. Ju, F. L. Dryer, K. Kumar, C.-J. Sung, H. Wang, M. A. Oehlschlaeger, et al., A jet fuel surrogate formulated by real fuel properties, Combustion and Flame 157 (12) (2010) 2333–2339.

[116] Y. Ra, R. D. Reitz, A combustion model for IC engine combustion simulations with multi-component fuels, Combustion and Flame 158 (1) (2011) 69–90.

[117] M. H. Hakka, P.-A. Glaude, O. Herbinet, F. Battin-Leclerc, Experimental study of the oxidation of large surrogates for diesel and biodiesel fuels, Combustion and Flame 156 (11) (2009) 2129–2144.

[118] R. Lemaire, A. Faccinetto, E. Therssen, M. Ziskind, C. Focsa, P. Desgroux, Experimental comparison of soot formation in turbulent flames of diesel and surrogate diesel fuels, Proceedings of the Combustion Institute 32 (1) (2009) 737–744.

[119] Y. Chang, M. Jia, Y. Liu, Y. Li, M. Xie, Development of a new skeletal mechanism for n-decane oxidation under engine-relevant conditions based on a decoupling methodology, Combustion and Flame 160 (8) (2013) 1315–1332.

[120] J. Biet, M. H. Hakka, V. Warth, P.-A. Glaude, F. Battin-Leclerc, Experimental and modeling study of the low-temperature oxidation of large alkanes, Energy & Fuels 22 (4) (2008) 2258–2269.

[121] N. Peters, Turbulent combustion, Cambridge university press, 2000.

[122] A. Cuoci, M. Mehl, G. Buzzi-Ferraris, T. Faravelli, D. Manca, E. Ranzi, Autoignition and burning rates of fuel droplets under microgravity, Combustion and Flame 143 (3) (2005) 211–226.

[123] A. Cuoci, A. Frassoldati, T. Faravelli, E. Ranzi, Numerical modeling of auto-ignition of isolated fuel droplets in microgravity, Proceedings of the Combustion Institute 35 (2) (2015) 1621–1627.

[124] M. Tanabe, T. Bolik, C. Eigenbrod, H. Rath, J. Sato, M. Kono, Spontaneous ignition of liquid droplets from a view of non-homogeneous mixture formation and transient chemical reactions, in: Symposium (International) on Combustion, Vol. 26, Elsevier, 1996, pp. 1637–1643.

[125] O. Moriue, C. Eigenbrod, H. Rath, J. Sato, K. Okai, M. Tsue, M. Kono, Effects of dilution by aromatic hydrocarbons on staged ignition behavior of n-decane droplets, Proceedings of the Combustion Institute 28 (1) (2000) 969–975.

[126] W. J. Pitz, C. J. Mueller, Recent progress in the development of diesel surrogate fuels, Progress in Energy and Combustion Science 37 (3) (2011) 330–350.

[127] B. Gauthier, D. Davidson, R. Hanson, Shock tube determination of ignition delay times in full-blend and surrogate fuel mixtures, Combustion and Flame 139 (4) (2004) 300–311.

[128] K. Fieweger, R. Blumenthal, G. Adomeit, Self-ignition of SI engine model fuels: A shock tube investigation at high pressure, Combustion and Flame 109 (4) (1997) 599–619.

[129] L. Sileghem, V. Alekseev, J. Vancoillie, K. Van Geem, E. Nilsson, S. Verhelst, A. Konnov, Laminar burning velocity of gasoline and the gasoline surrogate components iso-octane, n-heptane and toluene, Fuel 112 (2013) 355–365.

[130] S. Davis, C. Law, Laminar flame speeds and oxidation kinetics of iso-octane-air and n-heptane-air flames, in: Symposium (international) on combustion, Vol. 27, Elsevier, 1998, pp. 521–527.

[131] P. Dirrenberger, P.-A. Glaude, R. Bounaceur, H. Le Gall, A. P. da Cruz, A. Konnov, F. Battin-Leclerc, Laminar burning velocity of gasolines with addition of ethanol, Fuel 115 (2014) 162–169.

[132] A. Kelley, A. Smallbone, D. Zhu, C. Law, Laminar flame speeds of C_5 to C_8 n-alkanes at elevated pressures: Experimental determination, fuel similarity, and stretch sensitivity, Proceedings of the Combustion Institute 33 (1) (2011) 963–970.

[133] T. Hirasawa, C. Sung, A. Joshi, Z. Yang, H. Wang, C. Law, Determination of laminar flame speeds using digital particle image velocimetry: binary fuel blends of ethylene, n-butane, and toluene, Proceedings of the Combustion Institute 29 (2) (2002) 1427–1434.

[134] C. Marchal, J.-L. Delfau, C. Vovelle, G. Moréac, C. Mounaı, F. Mauss, et al., Modelling of aromatics and soot formation from large fuel molecules, Proceedings of the Combustion Institute 32 (1) (2009) 753–759.

[135] A. E. Bakali, J.-L. Delfau, C. Vovelle, Experimental study of 1 atmosphere, rich, premixed n-heptane and iso-octane flames, Combustion science and technology 140 (1-6) (1998) 69–91.

[136] T. Lu, C. K. Law, C. S. Yoo, J. H. Chen, Dynamic stiffness removal for direct numerical simulations, Combustion and Flame 156 (8) (2009) 1542–1551.

[137] C. E. Baukal Jr, Industrial burners handbook, CRC press, 2003.

[138] A. Frassoldati, T. Faravelli, E. Ranzi, Kinetic modeling of the interactions between NO and hydrocarbons at high temperature, Combustion and Flame 135 (1) (2003) 97–112.

[139] T. Lu, C. K. Law, A criterion based on computational singular perturbation for the identification of quasi steady state species: A reduced mechanism for methane oxidation with NO chemistry, Combustion and Flame 154 (4) (2008) 761–774.

[140] A. Konnov, I. Dyakov, J. De Ruyck, Probe sampling measurements and modeling of nitric oxide formation in methane-air flames, Combustion science and technology 169 (1) (2001) 127–153.

[141] F. Coppens, J. De Ruyck, A. Konnov, Effects of hydrogen enrichment on adiabatic burning velocity and NO formation in methane+air flames, Experimental Thermal and Fluid Science 31 (5) (2007) 437–444.

[142] H. Pitsch, M. Chen, N. Peters, Unsteady flamelet modeling of turbulent hydrogen-air diffusion flames, in: Symposium (international) on combustion, Vol. 27, Elsevier, 1998, pp. 1057–1064.

[143] M. Ihme, H. Pitsch, Modeling of radiation and nitric oxide formation in turbulent nonpremixed flames using a flamelet/progress variable formulation, Physics of Fluids (1994-present) 20 (5) (2008) 055110.

[144] M. Ravikanti, M. Hossain, W. Malalasekera, Laminar flamelet model prediction of NO_x formation in a turbulent bluff-body combustor, Proceedings of the Institution of Mechanical Engineers, Part A: Journal of Power and Energy 223 (1) (2009) 41–54.

[145] T. Shimizu, F. A. Williams, A. Frassoldati, Concentrations of nitric oxide in laminar counterflow methane/air diffusion flames, Journal of propulsion and power 21 (6) (2005) 1019–1028.

[146] R. Ravikrishna, N. M. Laurendeau, Laser-induced fluorescence measurements and modeling of nitric oxide in methane–air and ethane–air counterflow diffusion flames, Combustion and flame 120 (3) (2000) 372–382.

[147] G. Rørtveit, J. Hustad, No_x formations in diluted ch_4/h_2 counterflow diffusion flames, International Journal of Energy for a Clean Environment 4 (4).

[148] A. Stagni, C. Saggese, M. Bissoli, A. Cuoci, A. Frassoldati, T. Faravelli, E. Ranzi, Reduced kinetic model of biodiesel fuel combustion, Chemical Engineering Transactions 37 (2014) 877–882.

[149] P. Dagaut, M. Cathonnet, The ignition, oxidation, and combustion of kerosene: A review of experimental and kinetic modeling, Progress in energy and combustion science 32 (1) (2006) 48–92.

[150] T. Edwards, L. Q. Maurice, Surrogate mixtures to represent complex aviation and rocket fuels, Journal of Propulsion and Power 17 (2) (2001) 461–466.

[151] A. Violi, A. F. Sarofim, G. A. Voth, Kinetic monte carlo–molecular dynamics approach to model soot inception, Combustion science and technology 176 (5-6) (2004) 991–1005.

[152] A. Agosta, N. Cernansky, D. Miller, T. Faravelli, E. Ranzi, Reference components of jet fuels: kinetic modeling and experimental results, Experimental Thermal and Fluid Science 28 (7) (2004) 701–708.

[153] ASTM International, Astm standard d6890-15a, Standard Test Method for Determination of Ignition Delay and Derived Cetane Number (DCN) of Diesel Fuel Oils by Combustion in a Constant Volume Chamberdoi:10.1520/D6890-15A.

[154] A. J. Marchese, T. L. Vaughn, K. Kroenlein, F. L. Dryer, Ignition delay of fatty acid methyl ester fuel droplets: Microgravity experiments and detailed numerical modeling, Proceedings of the Combustion Institute 33 (2) (2011) 2021–2030.

[155] O. Moriue, M. Mikami, N. Kojima, C. Eigenbrod, Numerical simulations of the ignition of n-heptane droplets in the transition diameter range from heterogeneous to homogeneous ignition, Proceedings of the Combustion Institute 30 (2) (2005) 1973–1980.

[156] T. I. Farouk, F. L. Dryer, Isolated n-heptane droplet combustion in microgravity:"cool flames"–two-stage combustion, Combustion and Flame 161 (2) (2014) 565–581.

[157] A. M. Lippert, R. D. Reitz, Modeling of multicomponent fuels using continuous distributions with application to droplet evaporation and sprays, Tech. rep., SAE Technical Paper (1997).

[158] Y. Ra, R. D. Reitz, A vaporization model for discrete multi-component fuel sprays, International Journal of Multiphase Flow 35 (2) (2009) 101–117.

[159] S. Sazhin, M. Al Qubeissi, R. Kolodnytska, A. Elwardany, R. Nasiri, M. Heikal, Modelling of biodiesel fuel droplet heating and evaporation, Fuel 115 (2014) 559–572.

[160] S. Dooley, S. H. Won, J. Heyne, T. I. Farouk, Y. Ju, F. L. Dryer, K. Kumar, X. Hui, C.-J. Sung, H. Wang, et al., The experimental evaluation of a methodology for surrogate fuel formulation to emulate gas phase combustion kinetic phenomena, Combustion and Flame 159 (4) (2012) 1444–1466.

[161] S. Liu, J. C. Hewson, J. H. Chen, H. Pitsch, Effects of strain rate on high-pressure nonpremixed n-heptane autoignition in counterflow, Combustion and flame 137 (3) (2004) 320–339.

[162] R. Taylor, R. Krishna, Multicomponent mass transfer, Vol. 2, John Wiley & Sons, 1993.

[163] J. Wesselingh, R. Krishna, Mass transfer, Ellis Horwood Chichester, West Sussex (England), 1990.

[164] M. Siddiqi, K. Lucas, Correlations for prediction of diffusion in liquids, The Canadian Journal of Chemical Engineering 64 (5) (1986) 839–843.

[165] J. M. Prausnitz, R. N. Lichtenthaler, E. G. de Azevedo, Molecular thermodynamics of fluid-phase equilibria, Pearson Education, 1998.

[166] D.-Y. Peng, D. B. Robinson, A new two-constant equation of state, Industrial & Engineering Chemistry Fundamentals 15 (1) (1976) 59–64.

[167] K. K. Kuo, Principles of combustion, Wiley New York et al., 1986.

[168] L. Constantinou, R. Gani, New group contribution method for estimating properties of pure compounds, AIChE Journal 40 (10) (1994) 1697–1710.

[169] R. C. Reid, J. M. Prausnitz, B. E. Poling, The properties of gases and liquids.

[170] M. Burger, R. Schmehl, K. Prommersberger, O. Schäfer, R. Koch, S. Wittig, Droplet evaporation modeling by the distillation curve model: accounting for kerosene fuel and elevated pressures, International journal of heat and mass transfer 46 (23) (2003) 4403–4412.

[171] T. J. Bruno, L. S. Ott, B. L. Smith, T. M. Lovestead, Complex fluid analysis with the advanced distillation curve approach, Analytical chemistry 82 (3) (2009) 777–783.

[172] W. A. Sirignano, Fluid dynamics and transport of droplets and sprays, Cambridge University Press, 2010.

[173] D. Manca, G. Buzzi-Ferraris, The solution of DAE systems by a numerically robust and efficient solver, Computer Aided Chemical Engineering 24 (2007) 93–98.

[174] P. Govindaraju, M. Ihme, Multicomponent evaporation using group contribution method and application to transportation fuels, International Journal of Heat and Mass Transfer (in preparation).

[175] R. Lecourt, G. Linassier, G. Lavergne, Detailed characterisation of a swirled air/kerosene spray in reactive and non-reactive conditions downstream from an actual turbojet injection system, in: ASME 2011 Turbo Expo: Turbine Technical Conference and Exposition, American Society of Mechanical Engineers, 2011, pp. 185–194.

[176] A. H. Lefebvre, Gas turbine combustion, CRC press, 1998.

[177] E. Mobil, The outlook for energy: A view to 2040, Tech. rep., Texas, United States (2013).

[178] ICAO Environmental Protection, Annex 16 amendment 5, Aircraft Noise.

[179] T. Edwards, Liquid fuels and propellants for aerospace propulsion: 1903-2003, Journal of Propulsion and Power 19 (6) (2003) 1089–1107.

[180] M. Mueller, G. Blanquart, H. Pitsch, Hybrid method of moments for modeling soot formation and growth, Combustion and Flame 156 (6) (2009) 1143–1155.

[181] F. Bisetti, G. Blanquart, M. E. Mueller, H. Pitsch, On the formation and early evolution of soot in turbulent nonpremixed flames, Combustion and Flame 159 (1) (2012) 317–335.

[182] N. A. Janssen, M. E. Gerlofs-Nijland, T. Lanki, R. O. Salonen, F. Cassee, G. Hoek, P. Fischer, B. Brunekreef, M. Krzyzanowski, Health effects of black carbon, WHO Regional Office for Europe Copenhagen, Denmark, 2012.

[183] T. C. Bond, S. J. Doherty, D. Fahey, P. Forster, T. Berntsen, B. DeAngelo, M. Flanner, S. Ghan, B. Kärcher, D. Koch, et al., Bounding the role of black carbon in the climate system: A scientific assessment, Journal of Geophysical Research: Atmospheres 118 (11) (2013) 5380–5552.

[184] H. Wang, Formation of nascent soot and other condensed-phase materials in flames, Proceedings of the Combustion Institute 33 (1) (2011) 41 – 67.

[185] G. Jackson, C. Avedisian, The effect of initial diameter in spherically symmetric droplet combustion of sooting fuels, in: Proceedings of the Royal Society of London A: Mathematical, Physical and Engineering Sciences, Vol. 446, The Royal Society, 1994, pp. 255–276.

[186] D. L. Dietrich, V. Nayagam, M. C. Hicks, P. V. Ferkul, F. L. Dryer, T. Farouk, B. D. Shaw, H. K. Suh, M. Y. Choi, Y. C. Liu, et al., Droplet combustion experiments aboard the international space station, Microgravity Science and Technology 26 (2) (2014) 65–76.

[187] A. Krestinin, Detailed modeling of soot formation in hydrocarbon pyrolysis, Combustion and Flame 121 (3) (2000) 513–524.

[188] C. Saggese, S. Ferrario, J. Camacho, A. Cuoci, A. Frassoldati, E. Ranzi, H. Wang, T. Faravelli, Kinetic modeling of particle size distribution of soot in a premixed burner-stabilized stagnation ethylene flame, Combustion and Flame 162 (9) (2015) 3356–3369.

[189] A. Burcat, B. Ruscic, Third millenium ideal gas and condensed phase thermochemical database for combustion with updates from active thermochemical tables, Argonne National Laboratory Argonne, IL, 2005.

[190] S. W. Benson, Thermochemical kinetics, Wiley, 1976.

[191] M. Schenk, S. Lieb, H. Vieker, A. Beyer, A. Gölzhäuser, H. Wang, K. Kohse-Höinghaus, Morphology of nascent soot in ethylene flames, Proceedings of the Combustion Institute 35 (2) (2015) 1879–1886.

[192] C. Saggese, Detailed kinetic modeling of soot formation in combustion processes, Ph.D. thesis, Politecnico di Milano (2015).

[193] P. Berta, S. K. Aggarwal, I. K. Puri, An experimental and numerical investigation of n-heptane/air counterflow partially premixed flames and emission of no x and pah species, Combustion and flame 145 (4) (2006) 740–764.

[194] A. D'Anna, M. Alfe, B. Apicella, A. Tregrossi, A. Ciajolo, Effect of fuel/air ratio and aromaticity on sooting behavior of premixed heptane flames, Energy & Fuels 21 (5) (2007) 2655–2662.

[195] H. Calcote, D. Manos, Effect of molecular structure on incipient soot formation, Combustion and Flame 49 (1) (1983) 289–304.

[196] M. Kashif, P. Guibert, J. Bonnety, G. Legros, Sooting tendencies of primary reference fuels in atmospheric laminar diffusion flames burning into vitiated air, Combustion and Flame 161 (6) (2014) 1575–1586.

[197] M. Kashif, J. Bonnety, A. Matynia, P. Da Costa, G. Legros, Sooting propensities of some gasoline surrogate fuels: Combined effects of fuel blending and air vitiation, Combustion and Flame 162 (5) (2015) 1840–1847.

[198] P. S. Epstein, Zur theorie des radiometers, Zeitschrift für Physik 54 (7-8) (1929) 537–563.

[199] S. K. Friedlander, Smoke, dust and haze: Fundamentals of aerosol behavior, 1977.

[200] J. R. Howell, M. P. Menguc, R. Siegel, Thermal radiation heat transfer, CRC press, 2010.

[201] M. Smooke, C. McEnally, L. Pfefferle, R. Hall, M. Colket, Computational and experimental study of soot formation in a coflow, laminar diffusion flame, Combustion and Flame 117 (1) (1999) 117–139.

[202] M. Mikami, M. Niwa, H. Kato, J. Sato, M. Kono, Clarification of the flame structure of droplet burning based on temperature measurement in microgravity, in: Symposium (International) on Combustion, Vol. 25, Elsevier, 1994, pp. 439–446.

[203] W. Kaskan, The dependence of flame temperature on mass burning velocity, in: Symposium (International) on Combustion, Vol. 6, Elsevier, 1957, pp. 134–143.

[204] M. F. Modest, Radiative heat transfer, Academic press, 2013.

[205] Y. C. Liu, A. J. Savas, C. T. Avedisian, The spherically symmetric droplet burning characteristics of jet-a and biofuels derived from camelina and tallow, Fuel 108 (2013) 824–832.

[206] R. Bird, W. Stewart, E. Lightfoot, Transport Phenomena, John Wiley & Sons, 2007.

[207] S. Chapman, T. G. Cowling, The mathematical theory of non-uniform gases: an account of the kinetic theory of viscosity, thermal conduction and diffusion in gases, Cambridge university press, 1970.

[208] G. Ben-Dor, T. Elperin, B. Krasovit, Effect of thermo–and diffusiophoretic forces on the motion of flame-generated particles in the neighbourhood of burning droplets in microgravity conditions, in: Proceedings of the Royal Society of London A: Mathematical, Physical and Engineering Sciences, Vol. 459, The Royal Society, 2003, pp. 677–703.

[209] K.-O. Lee, S. L. Manzello, M. Y. Choi, The effects of initial diameter on sooting and burning behavior of isolated droplets under microgravity conditions, Combustion science and technology 132 (1-6) (1998) 139–156.

[210] S. L. Manzello, M. Y. Choi, A. Kazakov, F. L. Dryer, R. Dobashi, T. Hirano, The burning of large n-heptane droplets in microgravity, Proceedings of the Combustion Institute 28 (1) (2000) 1079–1086.

[211] L. Waldmann, On the motion of spherical particles in nonhomogeneous gases, in: Rarefied gas dynamics, 1961, p. 323.

[212] A. Toda, H. Ohnishi, R. Dobashi, T. Hirano, T. Sakuraya, Experimental study on the relation between thermophoresis and size of aerosol particles, International journal of heat and mass transfer 41 (17) (1998) 2710–2713.

[213] S. Kumar, A. Ray, S. Kale, A soot model for transient, spherically symmetric n-heptane droplet combustion, Combustion Science and Technology 174 (9) (2002) 67–102.

[214] A. Cuoci, A. E. Saufi, A. Frassoldati, D. L. Dietrich, F. A. Williams, T. Faravelli, Flame extinction and low-temperature combustion of isolated fuel droplets of n-alkanes, Proceedings of the Combustion Institute *under review.*

[215] V. Nayagam, D. L. Dietrich, M. C. Hicks, F. A. Williams, Cool-flame extinction during n-alkane droplet combustion in microgravity, Combustion and Flame 162 (5) (2015) 2140–2147.

[216] F. Cassol, R. Brittes, F. H. França, O. A. Ezekoye, Application of the weighted-sum-of-gray-gases model for media composed of arbitrary concentrations of H_2O, CO_2 and soot, International Journal of Heat and Mass Transfer 79 (2014) 796–806.

[217] T. Lu, C. K. Law, Systematic approach to obtain analytic solutions of quasi steady state species in reduced mechanisms, The Journal of Physical Chemistry A 110 (49) (2006) 13202–13208.

[218] A. Attili, F. Bisetti, M. E. Mueller, H. Pitsch, Damköhler number effects on soot formation and growth in turbulent nonpremixed flames, Proceedings of the Combustion Institute 35 (2) (2015) 1215–1223.

[219] H. C. Mongia, Ge aviation low emissions combustion technology evolution, Tech. rep., SAE Technical Paper (2007).

[220] K.-Y. Hsu, L. Goss, W. Roquemore, Characteristics of a trapped-vortex combustor, Journal of Propulsion and Power 14 (1) (1998) 57–65.

[221] D. Splitter, R. D. Reitz, R. Hanson, High efficiency, low emissions rcci combustion by use of a fuel additive, Tech. rep., SAE Technical Paper (2010).

[222] C. S. Yoo, T. Lu, J. H. Chen, C. K. Law, Direct numerical simulations of ignition of a lean n-heptane/air mixture with temperature inhomogeneities at constant volume: Parametric study, Combustion and Flame 158 (9) (2011) 1727–1741.

[223] C. S. Yoo, E. S. Richardson, R. Sankaran, J. H. Chen, A dns study on the stabilization mechanism of a turbulent lifted ethylene jet flame in highly-heated coflow, Proceedings of the Combustion Institute 33 (1) (2011) 1619–1627.

[224] Y. Ju, W. Sun, M. P. Burke, X. Gou, Z. Chen, Multi-timescale modeling of ignition and flame regimes of n-heptane-air mixtures near spark assisted homogeneous charge compression ignition conditions, Proceedings of the Combustion Institute 33 (1) (2011) 1245–1251.